Title
Measurement of CP asymmetries in the three-body charmless decay B' --> K's K's K's

Author
Hadavand, Haleh K.

Publication Date
2005

UNIVERSITY OF CALIFORNIA, SAN DIEGO

The Measurement of CP Asymmetries in the Three-Body Charmless Decay $B^0 \rightarrow K^0_S\, K^0_S\, K^0_S$

A dissertation submitted in partial satisfaction of the
requirements for the degree Doctor of Philosophy in
Physics

by

Haleh K. Hadavand

Committee in charge:

Professor David MacFarlane, Chair
Professor Ben Grinstein
Professor Doug Magde
Professor David Meyer
Professor Hans Paar

2005

The dissertation of Haleh Hadavand is approved, and it is acceptable in quality and form for publication on microfilm:

David Meyer

Douglas Magde

D Macfarlane

Chair

University of California, San Diego
2005

DEDICATION

This dissertation is dedicated to my parents who came to this country to give me and my brother the opportunity to pursue our education and live free lives. They sacrificed greatly for us. Without their strength, commitment, and love I could not achieve this.

TABLE OF CONTENTS

LIST OF FIGURES

LIST OF TABLES

VITA

1999	Bachelor of Science in Phyiscs, University of Maryland, College Park
1999–2000	Teaching Assistant, Department of Physics, University of California, San Diego
2000	Masters of Science, University of California, San Diego
2000–2005	Research Assistant, University of California, San Diego
2005	Ph.D., University of California, San Diego

ABSTRACT OF THE DISSERTATION

The Measurement of CP Asymmetries in the Three-Body Charmless Decay $B^0 \to K^0_S\, K^0_S\, K^0_S$

by

Haleh K. Hadavand

Doctor of Philosophy in Physics

University of California, San Diego, 2005

Professor David MacFarlane, Chair

In this dissertation, a measurement of CP-violating effects in decays of neutral B mesons is presented. The data sample for this measurement consists of about 272 million $\Upsilon(4S) \to B\bar{B}$ decays collected between 1999 and 2004 with the BABAR detector at the PEP-II asymmetric-energy e^+e^- collider, located at the Stanford Linear Accelerator Center. One neutral B meson is fully reconstructed in the CP eigenstate $B^0 \to K^0_S\, K^0_S\, K^0_S$. The other B meson is determined to be either a B^0 or a $\overline{B}{}^0$, at the time of its decay, from the properties of its decay products. The proper time Δt elapsed between the decay of the two mesons is determined by reconstructing their decay vertices, and by measuring the distance between them. A novel technique for determining the B vertex of the decay to the CP eigenstate $B^0 \to K^0_S\, K^0_S\, K^0_S$ has been applied since the tracks in the final state do not originate from the B decay vertex. The time-dependent CP asymmetry amplitudes are determined by the distributions of Δt in events with a reconstructed B meson in the CP eigenstate. The detector resolution and the b flavor tagging parameters are constrained by the Δt distributions of events with a fully reconstructed flavor eigenstate. Because of the special topology of this decay, the detector resolution on Δt must be checked for consistency with decays with tracks which originate from the B decay. From a maximum likelihood fit to the Δt distributions of all selected events, the value of the CP violating asymmetries are measured to be $S_{3K^0_S} = -0.71^{+0.38}_{-0.32} \pm 0.04$ and $C_{3K^0_S} = -0.34^{+0.28}_{-0.25} \pm 0.05$. Fixing $C = 0$ we measure the time-dependent CP asymmetry amplitude $\sin 2\beta = -S_{3K^0_S} = 0.79^{+0.39}_{-0.36} \pm 0.04$. The value of $\sin 2\beta$ is in agreement with Standard Model predictions.

Chapter 1

Introduction

One of the unresolved mysteries of science is the existence of more matter than anti-matter in the universe. A key ingredient for producing this asymmetry, *CP* violation, was first observed in 1964 [1] in K_L^0 decays. Since its discovery, *CP* violation has been of great interest to particle physicists. In 1967 Sakharov first showed that without *CP* violation, a universe which was matter-antimatter symmetric could not have evolved into the asymmetric one we see today.

Sakharov showed that in order to accommodate such a large asymmetry we must have three ingredients in theories describing the evolution of the universe. These three ingredients are know as the Sakharov conditions and include 1) baryon number changing processes 2) *CP* violation and 3) thermal in-equilibrium [2].

The topic of *CP* violation is therefore of interest to theoretical cosmologists as well. Although they believe that after the Big Bang the universe consisted of equal parts of matter and anti-matter, we observe today that $N >> \overline{N}$ where N is the number of baryons and $\overline{N}$ is the number of anti-baryons in the universe. We also observe that the number of photons N_γ in our universe is 10^{-10} times that of the number of baryons, N. The low number of photons is proof that there are no pockets of anti-matter elsewhere in the universe which would annihilate the matter to produce photons [3].

Our current scientific model, describing the interactions of particles, the Standard Model, has an elegant explanation of the *CP*-violating effects observed in the K_L^0 decays. This effect is provided by the *CP*-violating phase of the three-generation Cabibbo-Kobayashi-Maskawa (CKM) quark-mixing matrix [4]. However, experimental constraints from these measurements do not provide an stringent test of whether the CKM phase describes *CP* violation [5].

An excellent testing ground for *CP* violation is provided by B meson decays through the interference of particle-anti-particle mixing and decay. The *CP* violating phase can be measured from time-dependent rate asymmetries. For example a B^0 ($\overline{B}^0$) can decay to a *CP* eigenstate f_{CP} or mix into a $\overline{B}^0$ (B^0) then decay to the final state f_{CP}.

In order to perform time-dependent *CP* measurements of B decays the B factories with the detectors named *BABAR* at the Stanford Linear Accelerator(SLAC), and Belle, at KEK in Japan, were built. The PEP-II asymmetric e^+e^- collider at SLAC is designed to produce a large number of $\Upsilon(4S)$ decays to B^0 $\overline{B}^0$ pairs which evolve in a coherent state along the beam axis (z direction) with an average Lorenz boost of $\beta\gamma = 0.55$. Therefore the proper decay-time difference between the two B mesons can be calculated from the distance between the two B decay vertices in the z direction.

The B factories have been successfully taking data since 1999 and performed the first measurements of *CP* violation in theoretically clean charmonium channels in 2001. By 2002 both experiments concurred the existence of *CP* violation in the B meson decays through the measurement of the parameter $\sin 2\beta$. The current world average of $\sin 2\beta$ from charmonium decays is 0.685 ± 0.032 and hence clearly not zero which would indicate no *CP* violation [6]. More than 30 years after the first observation we discover another particle with *CP*-violating behavior and show that the CKM phase describes *CP* violation.

However the Standard Model does not, through the CKM phase, incorporate enough *CP* violation to explain the current matter-anti-matter asymmetry [7]. It is therefore worth pursuing searches for physics beyond the SM that would accommodate a large enough *CP*-violating phase to explain the asymmetry seen now.

One area of fairly recent interest in the search for new physics has been in decay modes called “penguin” decays. These decays can have large non-SM contributions which can clearly signal the existence of new physics. The decay of $B^0 \to K^0_S\, K^0_S\, K^0_S$ is of particular interest since its interpretation is also theoretically clean. A deviation of $\sin 2\beta$ measured from this decay from the one measured from charmonium modes, shown above, would be an indication of new physics. *CP* violation in several other “penguin modes” have already been measured but vary in the degree of theoretical uncertainties. This dissertation will detail the measurement of the $B^0 \to K^0_S\, K^0_S\, K^0_S$ penguin decay mode and therefore add to our understanding of these type of decays.

1.1 Overview of Analysis

In the coming chapters we will discuss the theory of *CP* violation in the SM, the *BABAR* detector, and the analysis technique in great detail. Before starting on this detailed discussion, we provide a concise overview of the analysis in order to facilitate the understanding of the chapters to follow.

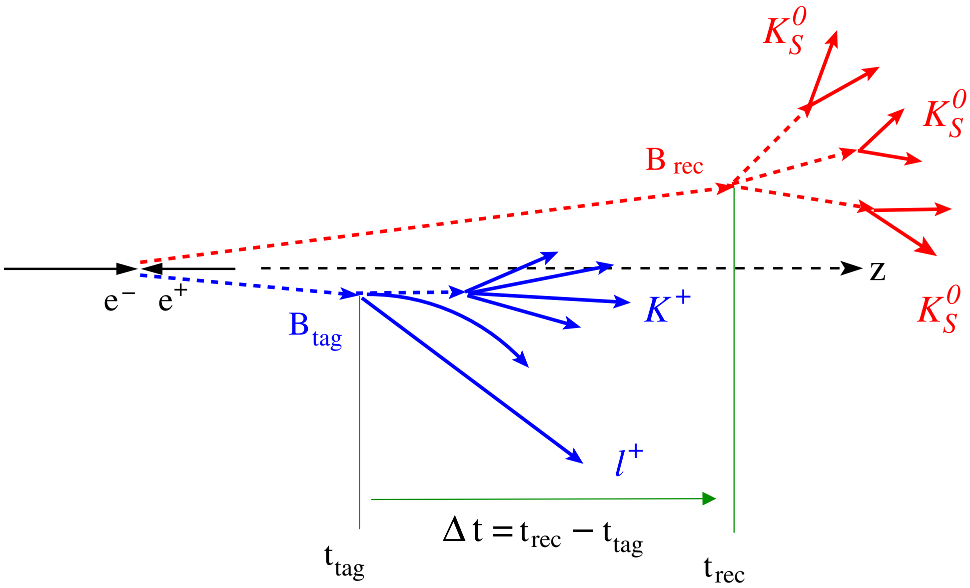

Figure 1.1: Topology of $B^0 \to K_S^0\, K_S^0\, K_S^0$ decay and Δt definition.

In the coming theory chapter we see how the three generations of quarks and leptons result in an irreducible phase which is responsible for CP violation in the SM. From the decay of B mesons one can measure the CP violating amplitude through the time-dependent CP asymmetry observable,

$$A_{CP}(\Delta t) = \mathcal{S} \sin(\Delta m_d \Delta t) - \mathcal{C} \cos(\Delta m_d \Delta t).$$

The measurement of the amplitudes of the sine and cosine term is what is measured experimentally.

The equation above is written as a function of time difference, Δt. The schematic depiction of this time difference is shown in fig 1.1 and is determined from the spatial separation along the z axis, or the direction of the boost, between the two B decays. Since the two B mesons from the $\Upsilon(4S)$ decay are in an *coherent* state, we do not need to know the absolute time of decay. This is described in more detail in sec. 2.4.

The boost of the $\Upsilon(4S)$ system is essential for measuring the spatial separation of the two B mesons. In the rest frame of the $\Upsilon(4S)$ system the separation between the two B decays is about

$30\mu m$ which is technologically challenging to measure with good precision. By boosting the system by $\beta\gamma$=0.55 the separation becomes about $260\mu m$ which is easily measured by the Silicon Vertex Tracker of the *BABAR* detector.

From fig 1.1 we see that one B is fully reconstructed in the *CP* eigenstate $B^0 \to K^0_S\, K^0_S\, K^0_S$, referred to as $B_{\rm rec}$. The other B, $B_{\rm tag}$, is inclusively reconstructed to determine the decay vertex and the *flavor* at the time of decay.

The $B^0 \to K^0_S\, K^0_S\, K^0_S$ decay has a special topology since the decay products seen by the detector, the pions, do not originate from the B vertex. This is due to the long lifetime of the K^0_S meson. In the decay of $B^0 \to J/\psi\ K^0_S$ for example, the J/ψ has prompt tracks which can help determine the B decay vertex with a resolution of about $50\mu m$ longitudinally. For the case of the $B^0 \to K^0_S\, K^0_S\, K^0_S$ decay we must impose an additional constraint to the transverse area of the luminous area beam, the beamspot, to determine the B decay vertex. The longitudinal vertex resolution is increased to about $75\mu m$ by using this technique for determining the vertex. The details of this are discussed in sec. 5.2.2.

The remaining particles in the event are used to inclusively reconstruct the $B_{\rm tag}$ vertex. It is necessary to inclusively reconstruct the tag side since exclusive B reconstruction efficiency is $O(10^{-3})$. The precision of $B_{\rm tag}$ decay vertex is about $100\mu m$ longitudinally. The distance between the two decay vertices has a resolution of about $180\mu m$ and is still dominated by the vertex resolution of $B_{\rm tag}$.

After determining the decay vertex of the two B mesons, we must determine the *flavor* of $B_{\rm tag}$ at the time of decay. This means that we must determine whether it was a B^0 or $\overline{B}^0$ at the time of decay. The coherence of the $\Upsilon(4S)$ system will then tell us the flavor of $B_{\rm rec}$ at the time of decay. This information cannot be determined directly from $B_{\rm rec}$ since it is a *CP* eigenstate.

The flavor of $B_{\rm tag}$ is correlated with the charge of the leptons and kaons produced in the decay. An algorithm which utilizes the kinematic and particle identification information of the decay products determines the flavor of the $B_{\rm tag}$ meson. This algorithm is referred to as *flavor tagging*. From this information we can determine whether a B^0 or a $\overline{B}^0$ decayed to the *CP* eigenstate.

The flavor tagging algorithm is a neural-network trained from Monte Carlo (MC) simulations. Since it is an inclusive algorithm there is a probability that a fraction of events, w, are assigned the wrong flavor. This fraction can be determined from MC simulations again, but because of differences in tracking and particles identification efficiencies between data and MC, we use a large sample of data events reconstructed in flavor eigenstates to determine a more accurate value of w. This sample is usually referred to as the *flavor sample*. The flavor sample is also used to determine the detector resolution on Δt.

As we mentioned earlier, $B^0 \to K^0_S\, K^0_S\, K^0_S$ decay vertex is determined by additional beamspot constraints. This implies that the detector resolution on Δt, which is derived from the difference in the longitudinal vertex positions of the B mesons, could be different from B decays with prompt tracks. We therefore test that the Δt resolution function is the same. This is discussed further in sections 5.3.2 and 6.1.

The time-dependent CP asymmetries are measured with a multi-dimensional maximum likelihood fit. The parametrization of the Δt resolution is determined from the flavor sample and is fixed in the fit to data. The probability distribution functions are parametrized using signal MC events and events from data that have a large probability of being background events. The fit is tested to insure it is unbiased using a large sample of events generated with a known value for the time-dependent CP asymmetries and with the same parametrization used for fitting the data sample.

The contents of the chapters to follow are summarized below:

- Chapter 2 describes the theory of CP violation in the SM and shows how the CP violation phase can be determined from B decays. It also describes the theoretical predictions for the $B^0 \to K^0_S\, K^0_S\, K^0_S$ decay.

- Chapter 3 describes the detector and how it is used to measure track kinematic and particle identification properties. We will also describe how the data is harvested from the detector and stored on disk for analysis.

- Chapter 4 describes the reconstruction of the $B^0 \to K^0_S\, K^0_S\, K^0_S$ decay and the selection of events which will be used in the maximum likelihood fit. We will then introduce the concept of maximum likelihood fits which will be describes again in more detail in 6.3.

- Chapter 5 describes the ingredients needed for performing a time-dependent CP measurement. These ingredients are 1) determining the B decay vertices, 2) determining the time difference between the two B decays, Δt, and 3) determining the flavor of B_{tag} and therefore that of B_{rec}. We will also describe the detector resolution for Δt.

- In chapter 6 we test that the Δt resolution function for the $B^0 \to K^0_S\, K^0_S\, K^0_S$ decay is similar to decays with prompt particles. After showing that the same resolution function can be used, we move on to parameterizing and validating the maximum likelihood fit. We then can perform a *blind* fit where the values of the asymmetries are hidden until no other checks and systematics uncertainties need to be added. Finally we *unblind* the fit to the data to obtain our final results.

- Finally, chapter 7 gives a summary of the results, the future prospective of the analysis, and compares the result with the theoretical predictions.

Chapter 2

Theory

In this chapter we describe *CP* violation in the Standard Model which describes interactions of particles. In 2.2 we describe the SM in terms of symmetries and introduce the elementary particles which it describes. We introduce the Cabibbo-Kobayashi-Maskawa (CKM) matrix, the quark-mixing matrix, and its properties which allow for *CP* violation in the SM in sections 2.2.2 and 2.2.3.

In section 2.3 we describe the phenomenology of *CP* violation. Here we describe how to actually measure *CP* violation and therefore describe the experimental observables. We then investigate our specific case of *CP* violation in $B^0 \to K^0_S\, K^0_S\, K^0_S$ decays in 2.4.

Finally in section 2.5 we show how the $B^0 \to K^0_S\, K^0_S\, K^0_S$ decay is a theoretically clean way to measure penguin dominated decays and therefore is a good mode for discovering physics beyond the SM.

2.1 Symmetries

Symmetries have played a fundamental role in understanding physical laws. They are of particular importance in particles physics and have been studied for over fifty years. Three discrete symmetries are of particular interest in particle physics:1) Time reversal, T, 2) Parity, P, and 3) Charge conjugation C. Time reversal changes the sign of the time coordinate $t \to -t$. Time reversal of classical theory shows no change in physical laws with a change of time direction. Similarly parity changes the sign of the spacial coordinate $\vec{x} \to -\vec{x}$. This symmetry exists since a mirror reflection about a coordinate plane does not change classical laws of motion. Charge parity symmetry was discovered much later during the time of the development of relativistic quantum physics theories and it has no counterpart in the classical theories of gravity and electromagnetism. Charge conjugation changes the sign of all quantum numbers of a particle except the spin and turns it into its anti-particle counterpart with equal mass.

Although it was thought that the forces of nature were invariant under the application of C, P, and T, in the late 50's scientists began to question these fundamental laws and proved that they can be violated in some cases. Parity violation was first observed in 1957 in nuclear β decay of ^{60}CO nuclei by C. Wu et al [8]. A year later, neutrino helicity experiments performed through weak interactions showed both C and P violation [9]. Neutrino helicity experiments are studies of the spin and momentum direction of the neutrinos as depicted in fig. 2.1. Charge conjugation transforms a left-handed neutrino (*i.e* opposite spin and momentum directions) to a left-handed anti-neutrino which is not observed in nature, hence C is violated in the weak interaction. Parity transforms a left-handed neutrino to a right-handed neutrino which is also not observed in nature therefore P is also violated in this weak interaction. The combination of C and P transformations however is not violated in decays of pions to a neutrino and muon as also shown in the fig. 2.1. Hence CP was thought to be a symmetry of weak interactions.

However in 1964 the combination of *CP* was also observed to be violated in the decay of $K_L^0 \rightarrow \pi\pi$ by Christensen et al [1]. In the coming decades scientist would try to incorporate *CP* violation into theories as a fundamental component of nature. Within the framework of the (SM) Kobayashi-Maskawa showed a mechanism by which *CP* violation could occur [4].

2.2 The Standard Model

The SM explains the fundamental theory of particles through three generations of quarks and leptons and their interactions through the weak, electromagnetic, and strong interactions. The material to follow is aimed to review the SM to the extent of showing what parameters are responsible for *CP* violation. The level of the material is suitable for a graduate student in high energy physics. The main results are summarized to aid people who are not familiar with field theory. A few good references for introduction to field theory can be found in references [10] and [11]. For a thorough discussion of *CP* violation see reference [12].

2.2.1 The Building Blocks/Particles, Forces and Field Theories

Particles are generally divided into two groups depending on their spin. Fermions are particles with half integer spin and bosons are particles with integer spin, see fig. 2.2. The SM is made

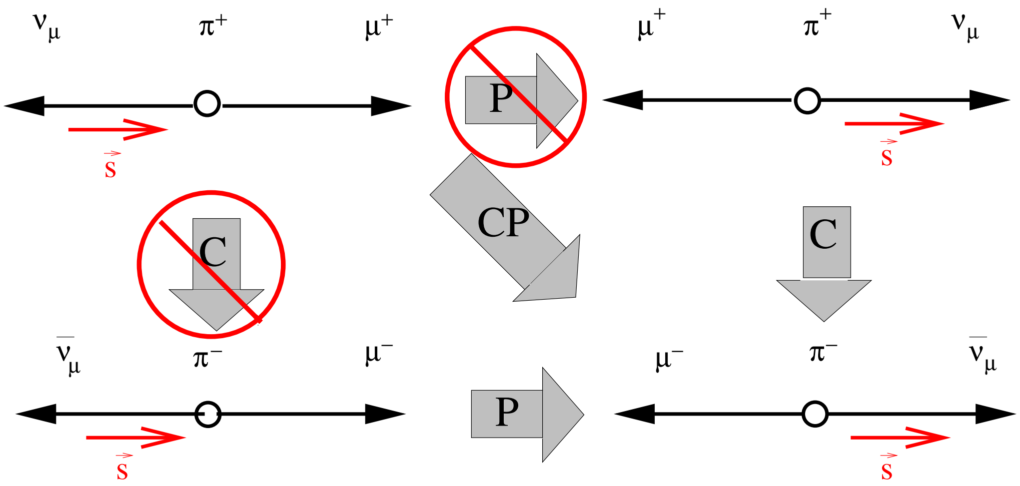

Figure 2.1: Schematic drawing of neutrino helicity experiments using the decays $\pi^{+/-} \rightarrow \mu^{+/-}\nu_\mu$ to show violation of C and P but conservation of CP.

of three generations of matter constituents known as quarks and leptons which are fermions. The qualities which identify these particles are electric charge, color, spin, flavor, or the generation, and mass which is unique for each particle. Each generation constitutes an up-type quark, charge $+2/3$, a down-type quark, charge $-1/3$, a lepton, and a neutrino of the corresponding type. Each particle has an antimatter partner that has equal mass but opposite charge and flavor. Quarks can be combined into two types of particles: mesons, which have two quark constituents and baryons which have three quark constituents.

The SM is made of forces which mediate interactions between the particles. These forces are, in order of relative strength: gravity, electromagnetism, weak force, and strong force. The force carriers are bosons listed in fig. 2.2 and are depicted in greater detail in fig. 2.4. The unification of the last three forces is possible at very high energy scales but at low energies each force is described by a different symmetry group. Combining gravity with these other forces to create a theory of quantum gravity is an important and challenging topic for physicists. However, gravitational interactions

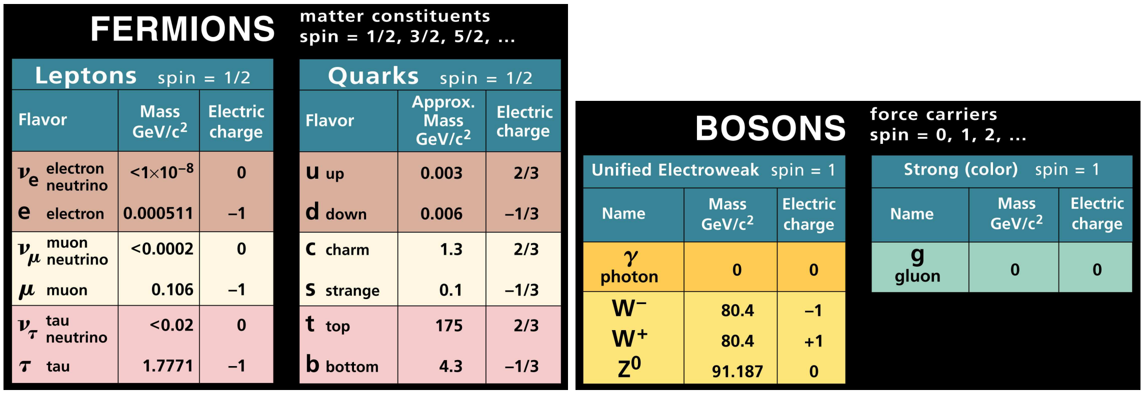

FERMIONS matter constituents
spin = 1/2, 3/2, 5/2, ...

Leptons spin = 1/2

Flavor	Mass GeV/c^2	Electric charge
ν_e electron neutrino	$<1\times10^{-8}$	0
e electron	0.000511	–1
ν_μ muon neutrino	<0.0002	0
μ muon	0.106	–1
ν_τ tau neutrino	<0.02	0
τ tau	1.7771	–1

Quarks spin = 1/2

Flavor	Approx. Mass GeV/c^2	Electric charge
u up	0.003	2/3
d down	0.006	–1/3
c charm	1.3	2/3
s strange	0.1	–1/3
t top	175	2/3
b bottom	4.3	–1/3

BOSONS force carriers
spin = 0, 1, 2, ...

Unified Electroweak spin = 1

Name	Mass GeV/c^2	Electric charge
γ photon	0	0
W$^-$	80.4	–1
W$^+$	80.4	+1
Z^0	91.187	0

Strong (color) spin = 1

Name	Mass GeV/c^2	Electric charge
g gluon	0	0

Figure 2.2: The list of fundamental particles divided into fermions and bosons.

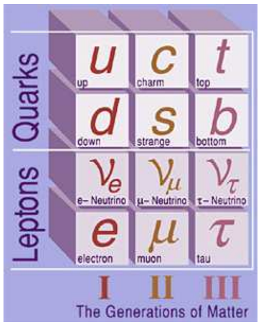

Figure 2.3: The three generations of matter in the universe.

have yet to be incorporated in a consistent manner into the SM and the force mediator for gravity, the graviton, has yet to be discovered.

A Lagrangian is a function which describes the equations of motion of a system. We are generally interested in the electroweak portion of the Lagrangian which is responsible for B mixing and decays.

A field theory Lagrangian depends on a bilinear fermion field which transforms as a Lorentz scalar. The properties of the bilinear fields and boson fields under C, P, and CP must be understood before we apply it to the SM Lagrangian. Table 2.1 shows the transformations of the these fields under the symmetries mentioned. By sandwiching the Dirac γ-matrices between the bilinear fields we can represent various Lorentz covariant currents. In general for a Lagrangian $\mathcal{L}$ to be invariant under CP it must satisfy the condition:

$$CP\mathcal{L}(t,\vec{x})(CP)^\dagger = \mathcal{L}(t,-\vec{x}) \tag{2.1}$$

While CP can be violated in relativistic field theories, CPT symmetry is preserved by construction. Its conservation is based on the fact that the field theory is Lorentz invariant and localized.

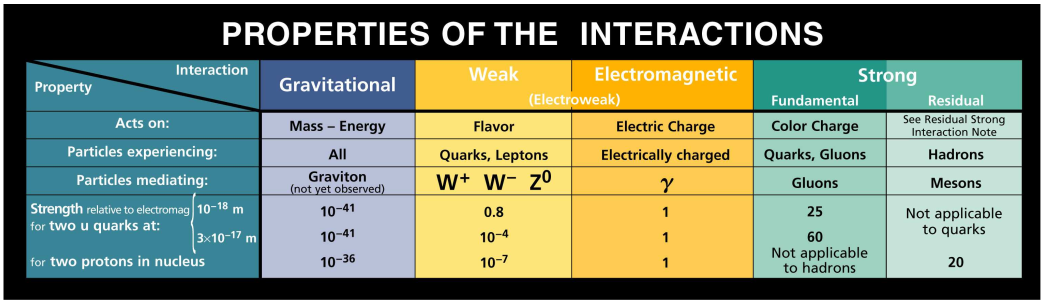

PROPERTIES OF THE INTERACTIONS

Property \ Interaction	Gravitational	Weak	Electromagnetic	Strong	
		(Electroweak)		Fundamental	Residual
Acts on:	Mass – Energy	Flavor	Electric Charge	Color Charge	See Residual Strong Interaction Note
Particles experiencing:	All	Quarks, Leptons	Electrically charged	Quarks, Gluons	Hadrons
Particles mediating:	Graviton (not yet observed)	W^+ W^- Z^0	γ	Gluons	Mesons
Strength relative to electromag for two u quarks at: 10^{-18} m	10^{-41}	0.8	1	25	Not applicable to quarks
3×10^{-17} m	10^{-41}	10^{-4}	1	60	
for two protons in nucleus	10^{-36}	10^{-7}	1	Not applicable to hadrons	20

Figure 2.4: The properties of the interactions in the Standard Model.

Table 2.1: Properties of charged boson fields and corresponding fermion bilinear terms under **P**, **C**, and **CP**. γ^5 and γ^μ are the Dirac matrices.

Fermion bilinear	Boson field F	$\mathbf{P}\,F\,\mathbf{P}^\dagger$	$\mathbf{C}\,F\,\mathbf{C}^\dagger$	$\mathbf{CP}\,F\,\mathbf{CP}^\dagger$
$\overline{\psi}\psi$	Scalar $S^+(t,\vec{x})$	$S^+(t,-\vec{x})$	$S^-(t,\vec{x})$	$S^-(t,-\vec{x})$
$\overline{\psi}\gamma^5\psi$	Pseudoscalar $P^+(t,\vec{x})$	$-P^+(t,-\vec{x})$	$P^-(t,\vec{x})$	$-P^-(t,-\vec{x})$
$\overline{\psi}\gamma_\mu\psi$	Vector $V_\mu^+(t,\vec{x})$	$V_\mu^+(t,-\vec{x})$	$-V_\mu^-(t,\vec{x})$	$-V_\mu^-(t,-\vec{x})$
$\overline{\psi}\gamma_\mu\gamma^5\psi$	Axial $A_\mu^+(t,\vec{x})$	$-A_\mu^+(t,-\vec{x})$	$A_\mu^-(t,\vec{x})$	$-A_\mu^-(t,-\vec{x})$

2.2.2 CKM Matrix

The SM of particle physics is a field theory with local gauge symmetry $SU(3)\times SU(2)\times U(1)$ and describes the strong and electroweak interactions between the particles. In the Lagrangian the fermions are governed by terms like $\overline{\psi}\delta_\mu\psi$ and $\overline{\psi}\gamma^\mu\delta_\mu\psi$. The gauge symmetry requirement forces the derivative to become a covariant derivative

$$\delta^\mu \longrightarrow \mathcal{D}^\mu = \delta^\mu - ig_1\frac{Y}{2}B^\mu - ig_2\frac{\sigma_i}{2}W_i^\mu - ig_3\frac{\lambda_a}{2}G_a^\mu, \tag{2.2}$$

where G_a^μ, W^μ, and B^μ are the mediators of the $SU(3)$, $SU(2)$, and $U(1)$ gauge symmetries respectively. Y, σ_i, and λ_a are the generators of the groups with coupling constants g_i. We will focus on CP violation in electroweak interactions since there is no experimental evidence of CP violation in strong interactions.

The SM includes a single Higgs scalar doublet field which interacts with the quarks to generate the fermion masses through the spontaneous symmetry breaking mechanism [11]. The Lagrangian for a scalar Higgs field H can be written as

$$\mathcal{L}_{\text{Higgs}} = (D_\mu H)^\dagger(D_\mu H) - \frac{\lambda}{4}(H^\dagger H - v^2/2)^2 \tag{2.3}$$

where the last term is the Higgs potential. The four bosons ($W^{\pm}$,W^0,B^0) are massless until the $SU(2) \times U(1)$ symmetry is broken resulting in three massive bosons ($W^{\pm}$,Z^0) and one massless boson, γ. The symmetry is broken at the minimum of the Higgs potential. Expanding the Lagrangian around the minimum Higgs field given by [10]

$$H_0 = \begin{pmatrix} 0 \\ v/\sqrt{2} \end{pmatrix}, \tag{2.4}$$

the electroweak Lagrangian becomes:

$$\begin{aligned}
\mathcal{L}_{\text{electroweak}}|_{H_0} &= \left| \left(-i\frac{g_1}{2}B^\mu - ig_2\frac{\sigma_i}{2}W_i^\mu \right) H_0 \right|^2 \\
&= \frac{1}{8} \left| \begin{pmatrix} g_2 W_\mu^3 + g_1 B_\mu & g_2\left(W_\mu^1 - iW_\mu^2\right) \\ g_2\left(W_\mu^1 - iW_\mu^2\right) & -g_2 W_\mu^3 + g_1 B_\mu \end{pmatrix} \begin{pmatrix} 0 \\ v \end{pmatrix} \right|^2 \\
&= \frac{1}{8}v^2 g_2^2 \left[\left(W_\mu^1\right) + \left(W_\mu^2\right)^2 \right] + \frac{1}{8}v^2 \left(g_1 B_\mu - g_2 W_\mu^3\right)\left(g_1 B^\mu - g_2 W^{3\mu}\right) \\
&= \left(\frac{1}{2}vg_2\right)^2 W_\mu^+ W^{-\mu} + \frac{1}{8}v^2 \begin{pmatrix} W_\mu^3 & B_\mu \end{pmatrix} \begin{pmatrix} g_2^2 & -g_1 g_2 \\ -g_1 g_2 & g_1^2 \end{pmatrix} \begin{pmatrix} W^{3\mu} \\ B^\mu \end{pmatrix}.
\end{aligned} \tag{2.5}$$

Here defining $W^{\pm} = (W^1 \mp iW^2)/\sqrt{2}$ we find $M_W = \frac{1}{2}vg_2$. The eigenvalues of the second term in eq. 2.5 are 0 and $\frac{v^2}{8}(g_1^2 + g_2^2)$ with eigenvectors which correspond to the A_μ and Z_μ physical states respectively. So the normalized fields and corresponding eigenvalues can be written as

$$A_\mu = \frac{g_1 W_\mu^3 + g_2 B_\mu}{\sqrt{g_1^2 + g_2^2}} \qquad \text{with } M_A = 0 \tag{2.6}$$

$$Z_\mu = \frac{g_2 W_\mu^3 - g_1 B_\mu}{\sqrt{g_1^2 + g_2^2}} \qquad \text{with } M_Z = \frac{v}{2}\sqrt{g_1^2 + g_2^2} \tag{2.7}$$

Using $\tan\theta_W = g_1/g_2$ to rewrite the equations above we get

$$A_\mu = \cos\theta_W B_\mu + \sin\theta_W W_\mu^3 \,,\; Z_\mu = -\sin\theta_W B_\mu + \cos\theta_W W_\mu^3, \tag{2.8}$$

and we see that $M_W = \cos\theta_W M_Z$ [10].

We now introduce the Yukawa coupling of the Higgs to the fermions:

$$\mathcal{L}_{\text{Yukawa}} = g_u^{ij}\bar{u}_R^i H^T(-\sigma_1\sigma_2)Q_L^j - g_d^{ij}\bar{d}_R^i H^\dagger Q_L^j - g_e^{ij}\bar{e}_R^i H^\dagger L_L^j + \text{h.c.}, \tag{2.9}$$

where σ_i are the Pauli matrices. By expanding the Higgs field around the minimum of this Lagrangian, as we did for the Higgs Lagrangian, the fermions become massive. Equation 2.9 then becomes (ignoring the lepton terms):

$$\mathcal{L}_M = -\frac{1}{\sqrt{2}}vg_d^{ij}\overline{d_{Li}}d_{Rj} - \frac{1}{\sqrt{2}}vg_u^{ij}\overline{u_{Li}}u_{Rj} + \text{h.c.}, \tag{2.10}$$

with the mass matrices

$$M_d = \mathbf{g}_d v/\sqrt{2}, M_u = \mathbf{g}_u v/\sqrt{2}. \tag{2.11}$$

These mass matrices are not necessarily diagonal which implies there's mixing between the generations. To get the definite mass of the particles as found in nature we must diagonalize the mass matrices. This can be done by using four unitary matrices such that:

$$\mathbf{V}_{dL} M_d V^\dagger_{dR} = M^{\text{diag}}_d \, , \mathbf{V}_{uL} M_u V^\dagger_{uR} = M^{\text{diag}}_u \tag{2.12}$$

where $\mathbf{M}^{\text{diag}}_q$ are diagonal and real while $\mathbf{V}_{qR}$ and $\mathbf{V}_{qL}$ are complex. In the mass basis the charged current interactions can be written as

$$\mathcal{L}_W = -\frac{1}{\sqrt{2}} g_2 \overline{u}_{Li} \gamma^\mu \mathbf{V}_{CKMij} d_{Lj} W^+_\mu + \text{h.c.}. \tag{2.13}$$

where $\mathbf{V}_{CKM} = \mathbf{V}_{uL}\mathbf{V}^\dagger_{dL}$ is the unitary mixing matrix for three quark generations. More precisely

$$V_{\text{CKM}} = \begin{pmatrix} V_{ud} & V_{us} & V_{ub} \\ V_{cd} & V_{cs} & V_{cb} \\ V_{td} & V_{ts} & V_{tb} \end{pmatrix} \tag{2.14}$$

where each term correspond to the mixing amplitude between left handed quarks through W boson exchange. This is known as the Cabibbo-Kobayashi-Maskawa matrix [4].

In summary, by expanding the Higgs potential around the vacuum expectation value the fermions become massive. The CKM matrix arises by just changing our basis from the electroweak to the mass basis, i.e. by just diagonalizing the matrices M_d and M_u. Each term of the CKM matrix governs the rate at which one quark can mix into another quark. We see in sec. 2.2.4 that transitions between the first and third generations are less likely than first to second or vice versa. In section 2.2.3 we see how the number of generations is significant for the existence of *CP* violation in the SM.

2.2.3 *CP* Violation in the Standard Model

Examining the relevant terms in the SM Lagrangian, we note that

$$(CP)\frac{g_2}{\sqrt{2}}\bar{u}'^i_L\gamma^\mu(V_{\text{CKM}})^{ij}d'^j_L W^+_\mu (CP)^\dagger = e^{i\phi}\frac{g_2}{\sqrt{2}}\bar{d}'^i_L\gamma^\mu(V_{\text{CKM}})^{ij}u'^j_L W^-_\mu \tag{2.15}$$

which when compared to the hermitian conjugate term $\frac{g_2}{\sqrt{2}}\bar{d}^i_L\gamma^\mu(V^*_{\text{CKM}})^{ij}u^j_L W^-_\mu$ implies that *CP* conservation requires

$$V^*_{ij} = e^{i\phi} V_{ij}. \tag{2.16}$$

Here ϕ is an arbitrary single phase, which may be chosen to satisfy the condition (2.16) for one CKM element. However, the condition is not necessarily satisfied for all elements, and if more than one element of the CKM matrix is complex, *CP* conservation is violated in the SM.

The phases in the CKM matrix can be reduced by a simple transformation such that

$$V_{CKM} \to \overline{V_{CKM}} = P_u V_{CKM} P_d^*. \tag{2.17}$$

where P_u and P_d are diagonal phase matrices. Such a transformation is allowed since it redefines the phases of the quark mass eigenstate fields but leaves the diagonal mass matrix M_q^{diag} unchanged. In general for a given number of generation n one has $(n-2)(n-1)/2$ irreducible phases by this transformation.

For three quark generations the complex CKM matrix has $2n^2$ parameters. Imposing unitarity removes half of these leaving n^2. Then we see that we have

- $\frac{1}{2}n(n-1)$ real angles, and
- $n^2 - \frac{1}{2}n(n-1) = \frac{1}{2}n(n+1)$ complex phases.

However, as noted above the $2n$ quark fields can be redefined to remove $2n-1$ phases. Then we arrive at our expression above for the number of irreducible phases:

- $\frac{1}{2}n(n+1) - 2n - 1 = \frac{1}{2}(n-1)(n-2)$.

Thus, for three generations of quarks there is one irreducible phase which is the source of *CP* violation. Note that if there were two generations of quarks as was the model about thirty years ago, the theory could not support *CP* violation since there would be no phase.

2.2.4 CKM Matrix and Unitarity Triangle

A survey of experimental results from weak decays of hadrons and deep inelastic neutrino-nucleon scattering gives us values of the CKM matrix parameters. There are theoretical errors associated with hadronic quantities and there are of course experimental uncertainties in each measurement. Our present knowledge of the parameters is [13]:

$$|\mathbf{V_{CKM}}| \equiv \begin{pmatrix} 0.9741-0.9756_{ud} & 0.219-0.226_{us} & 0.0025-0.0048_{ub} \\ 0.219-0.226_{cd} & 0.9732-0.9748_{cs} & 0.038-0.044_{cb} \\ 0.004-0.014_{td} & 0.037-0.044_{ts} & 0.9990-0.9993_{tb} \end{pmatrix}, \tag{2.18}$$

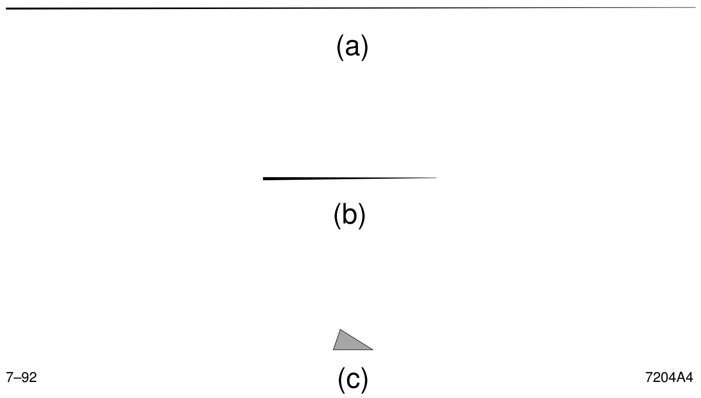

Figure 2.5: The unitarity triangles defined by (2.20) in a), (2.21) in b), and (2.22) in c). The same scale has been used for all triangles.

Examining the values of the term in the matrix, we notice that mixing within the same generation, denoted by the diagonal terms, is most probable and gets smaller between the first and second generations and even smaller between the first and third generations. The values with the most uncertainty are between the first and third generations i.e. V_{td} and V_{ub}.

A useful and elegant parametrization of the CKM matrix is the Wolfenstein parametrization [14]. This is the parametrization most often used by experimentalists:

$$V_{\mathrm{CKM}} = \begin{pmatrix} 1-\frac{\lambda^2}{2}{}_{ud} & \lambda_{us} & A\lambda^3(\rho-i\eta)_{ub} \\ -\lambda_{cd} & 1-\frac{\lambda^2}{2}{}_{cs} & A\lambda^2_{cb} \\ A\lambda^3(1-\rho-i\eta)_{td} & -A\lambda^2_{ts} & 1_{tb} \end{pmatrix} + O(\lambda^4), \tag{2.19}$$

where $\lambda = V_{us} = 0.2205 \pm 0.0018$ and $V_{cb} = A\lambda^2$ so that $A = 0.84$ [5]. The parameters ρ and η are the ones which have the largest uncertainty associated to them and they occur in the transition from first to third generation.

Unitarity of V_{CKM} imposes nine constraints on the elements of the matrix. There are six constraints which require the sum of the terms to equal zero. Three of these constraints

$$V_{ud}V^*_{us} + V_{cd}V^*_{cs} + V_{td}V^*_{ts} = 0, \tag{2.20}$$

$$V_{us}V^*_{ub} + V_{cs}V^*_{cb} + V_{ts}V^*_{tb} = 0, \tag{2.21}$$

$$V_{ud}V^*_{ub} + V_{cd}V^*_{cb} + V_{td}V^*_{tb} = 0. \tag{2.22}$$

are useful for illustrating the level of *CP* violation in the decays. The pictorial depiction of the triangles is shown in fig 2.5 and although they may look very different they should have the same area. The triangle with the largest angles 2.22 requires the least experimental precision to measure and is related to the B_d meson decays. The remainder of the discussion will focus on measuring the angles of this triangle, β, γ, and α (see fig 2.6). The triangle can also be shown on the ρ, η plane by dividing on one side by $V_{cd}V_{cb}^*$ (see fig 2.7); then the apex of the triangle would give the value of ρ and η. This method of displaying the triangle is specially useful in visualizing experimental results.

The angles can be measured from the length of the sides of the triangles, but observation of CP violation in B decays will directly measure the angles as we will see in 2.4.2. The angles are defined as:

$$\alpha \equiv \arg\left[\frac{-V_{td}V_{tb}^*}{V_{ud}V_{ub}^*}\right], \ \beta \equiv \arg\left[\frac{-V_{cd}V_{cb}^*}{V_{td}V_{tb}^*}\right], \ \gamma \equiv \arg\left[\frac{-V_{ud}V_{ub}^*}{V_{cd}V_{cb}^*}\right] \equiv \pi - \alpha - \beta \, . \tag{2.23}$$

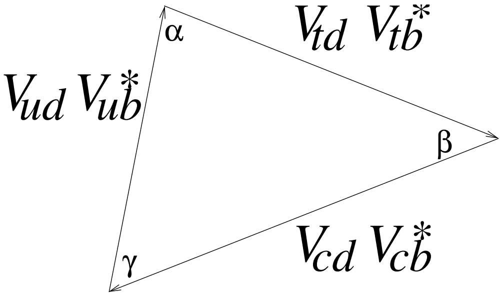

Figure 2.6: The Unitarity Triangle.

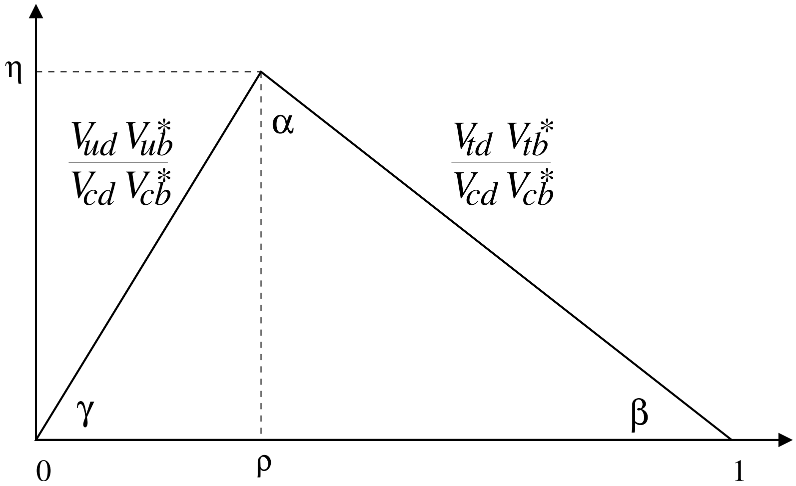

Figure 2.7: The Unitarity Triangle in the $\rho - \eta$ plane.

2.3 CP Violation Phenomenology

Now that we've seen the source of *CP* violation in the SM we can turn to how to measure it in experiments. In the next three sections we will discuss the different types of *CP* violation which can be measured. In section 2.3.2 we will discuss the observables which are measured in this analysis specifically.

2.3.1 Mixing of Neutral Mesons

Mixing occurs because the flavor eigenstates are not equivalent to the mass eigenstates i.e. one cannot measure both the mass and flavor of the particle simultaneously. Time evolution will rotate the flavor eigenstates while preserving the mass eigenstates. We saw an example of mixing in section 2.2.2 in the electroweak sector of the SM, where mixing between the quark generations occur by changing from the flavor to mass basis.

We can express the mass eigenstates as a function of flavor eigenstates :

$$|\psi\rangle = \psi_1|P^0\rangle + \psi_2|\overline{P}^0\rangle \tag{2.24}$$

and write the time-dependent Schrodinger equation as:

$$i\frac{d}{dt}\begin{pmatrix}\psi_1\\ \psi_2\end{pmatrix} = \mathcal{H}\begin{pmatrix}\psi_1\\ \psi_2\end{pmatrix} = (\mathbf{M}-\frac{i}{2}\mathbf{\Gamma})\begin{pmatrix}\psi_1\\ \psi_2\end{pmatrix}. \tag{2.25}$$

The Hamiltonian is not Hermitian, but the matrices $\mathbf{M}$ and $\mathbf{\Gamma}$ are. Under the assumption of CPT invariance $H_{11} = H_{22}$.

The matrices $\mathbf{M}$ and $\mathbf{\Gamma}$ may be computed from the weak Hamiltonian $\mathcal{H}_{\mathrm{EW}}$ in second order perturbation theory as [5]

$$\begin{aligned} M_{ij} &= m_0\delta_{ij} + \langle i|\mathcal{H}_{\mathrm{EW}}|j\rangle + \sum_n P\frac{\langle i|\mathcal{H}_{\mathrm{EW}}|n\rangle\langle n|\mathcal{H}_{\mathrm{EW}}|j\rangle}{(m_0-E_n)}, && (2.26)\\ \Gamma_{ij} &= 2\pi\sum_n \delta(m_0-E_n)\langle i|\mathcal{H}_{\mathrm{EW}}|n\rangle\langle n|\mathcal{H}_{\mathrm{EW}}|j\rangle. && (2.27)\end{aligned}$$

The eigenvalues of equation 2.25 are

$$\mu_\pm = M\frac{i}{2}\Gamma \mp \sqrt{(M_{12}-\frac{i}{2}\Gamma_{12})(M_{12}^*-\frac{i}{2}\Gamma_{12}^*)}, \tag{2.28}$$

with $\Gamma \equiv \Gamma_{11} \equiv \Gamma_{22}$ and $M \equiv M_{11} \equiv M_{22}$. The eigenvalues can also be expressed in terms of Δm_d and $\Delta\Gamma$

$$\Delta\mu = \Delta m_d - \frac{i}{2}\Delta\Gamma = m_H - m_L - \frac{i}{2}(\Gamma_H - \Gamma_L) = 2\sqrt{\mathcal{H}_{12}\mathcal{H}_{21}}, \tag{2.29}$$

where (m_H, m_L) and $(1/\Gamma_H, 1/\Gamma_L)$ are the masses and lifetimes of the heavy and light mass states $|P_H\rangle$ and $|P_L\rangle$.

Then the eigenstates corresponding to eigenvalues 2.28 can be expressed as

$$|P_L\rangle = p|P^0\rangle + q|\overline{P^0}\rangle \;,\; |P_H\rangle = p|P^0\rangle - q|\overline{P^0}\rangle, \tag{2.30}$$

where the coefficients p and q are

$$p = \sqrt{(M_{12} - \frac{i}{2}\Gamma_{12})(M_{12}^* - \frac{i}{2}\Gamma_{12}^*)}\;,\; q = M_{12}^* - \frac{i}{2}\Gamma_{12}. \tag{2.31}$$

which obey the normalization condition

$$|q|^2 + |p|^2 = 1. \tag{2.32}$$

A useful quantity in the study of *CP* violation is the ratio

$$\frac{p}{q} = \frac{\sqrt{M_{12}^* - \frac{i}{2}\Gamma_{12}^*}}{\sqrt{M_{12} - \frac{i}{2}\Gamma_{12}}} = \frac{\Delta m_d - \frac{i}{2}\Delta\Gamma}{2(M_{12} - \frac{i}{2}\Gamma_{12})} = -\frac{2(M_{12}^* - \frac{i}{2}\Gamma_{12}^*)}{\Delta m_d - \frac{i}{2}\Delta\Gamma}, \tag{2.33}$$

whose magnitude and phase translate into parameters of *CP* asymmetry. This will be discussed further in section 2.4.1.

If $|q/p| \neq 1$ then *CP* is violated and the mass eigenstates are not the same as *CP* eigenstates. This is called *CP violation in mixing or indirect CP violation*. Indirect *CP* violation in the SM is expected to be small, $O(10^{-2})$ [12].

2.3.2 CP violating observable

The *CP* operator relates the conjugate states by inducing arbitrary phases

$$\begin{aligned} CP|i\rangle &= e^{i\eta_i}|\bar{i}\rangle \quad , \quad CP|\bar{i}\rangle = e^{-i\eta_i}|i\rangle, \\ CP|f\rangle &= e^{i\eta_f}|\bar{f}\rangle \quad , \quad CP|\bar{f}\rangle = e^{-i\eta_f}|f\rangle. \end{aligned} \tag{2.34}$$

Applying these condition to equation 2.26 implies that *CP* is conserved when

$$\begin{aligned} M_{12}^* &= e^{2i\eta}M_{12}\;, \\ \Gamma_{12}^* &= e^{2i\eta}\Gamma_{12}. \end{aligned} \tag{2.35}$$

Considering the decay of $P^0/\overline{P}^0$ meson to the final states $f/\overline{f}$ gives the amplitudes

$$\begin{aligned} A_f &\equiv \langle f|T|P^0\rangle \quad , \quad \bar{A}_f \equiv \langle f|T|\bar{P}^0\rangle, \\ A_{\bar{f}} &\equiv \langle \bar{f}|T|P^0\rangle \quad , \quad \bar{A}_{\bar{f}} \equiv \langle \bar{f}|T|\bar{P}^0\rangle. \end{aligned} \tag{2.36}$$

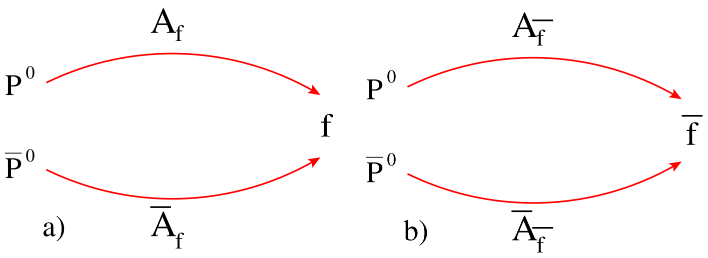

Figure 2.8: Schematic drawing of CP violation in decay. a) P^0 or $\overline{P^0}$ decaying into f b) P^0 or $\overline{P^0}$ decaying into $\overline{f}$; CP violation occurs when $|A_f| \neq |\overline{A}_f|$ or $|A_{\overline{f}}| \neq |\overline{A}_{\overline{f}}|$.

Using 2.34 and 2.35 the amplitudes can be written as

$$\begin{aligned} \bar{A}_{\bar{f}} &= e^{i(\eta_f-\eta)} A_f \quad \Rightarrow \quad |A_f| = |\bar{A}_{\bar{f}}|, \\ A_{\bar{f}} &= e^{i(\eta_f+\eta)} \bar{A}_f \quad \Rightarrow \quad |A_{\bar{f}}| = |\bar{A}_f|. \end{aligned} \tag{2.37}$$

as the CP invariant conditions. If these conditions do not hold we have *CP violation in decay*. This is shown pictorially in fig 2.8.

So far we've discussed both CP violation in mixing and decays. The next natural observable to follow from the latter would be the *CP violation through the interference between mixing and decay*. Taking the ratio of amplitudes shown in eq. 2.37 we find

$$\frac{A_f A_{\bar{f}}}{\bar{A}_f \bar{A}_{\bar{f}}} = e^{2i\eta} = \frac{q^2}{p^2}, \tag{2.38}$$

and define useful parameters

$$\Lambda_f \equiv \frac{q}{p}\frac{\bar{A}_f}{A_f}\, , \Lambda_{\bar{f}} \equiv \frac{q}{p}\frac{\bar{A}_{\bar{f}}}{A_{\bar{f}}}.$$

If the final state is a CP eigenstate (i.e. $CP|f\rangle = \eta_{f_{CP}}|f\rangle$, $\eta_{f_{CP}} = \pm 1$) we can write

$$A_f = Ae^{i(\delta+\phi_W)}\, , \overline{A}_f = \eta_{f_{CP}} Ae^{i(\delta-\phi_W)} \tag{2.39}$$

$$q/p = e^{2i\phi_M} \tag{2.40}$$

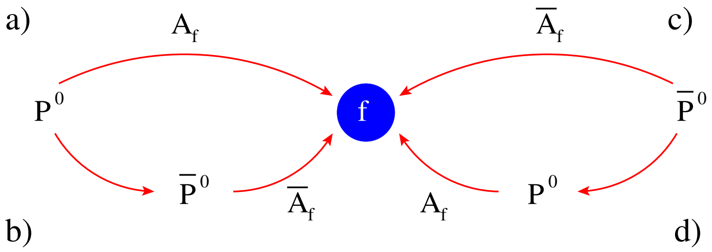

Figure 2.9: Schematic drawing of CP violation in the interference of mixing and decay. a) P^0 can decay directly to f; b) P^0 can mix into $\overline{P^0}$ then decay to f; c) $\overline{P^0}$ can decay directly to f; d) $\overline{P^0}$ can mix into P^0 then decay to f.

where δ is the CP even strong phase and ϕ_W is the CP odd weak phase and therefore changes sign. Then $\Lambda_f = \Lambda_{\overline{f}}$ is

$$\Lambda_f = \eta_{f_{CP}} e^{2i(\phi_M - \phi_D)}. \tag{2.41}$$

In order to have CP violation $\Lambda \neq \pm 1$ must hold in general. In order to have CP violation in mixing the condition $|q/p| \neq 1$ must hold while for CP violation in decay the condition $|\overline{A}_f/A_f| \neq 1$ must hold. And for CP violation in the interference of mixing and decay the phase difference $\phi_m - \phi_W$ must not vanish.

In section 2.4 we will see how Λ_f appears in the time evolution of the B^0 meson. We will also see how it is related to the CKM parameters for B decays.

2.4 Neutral B Mesons from $\Upsilon(4S)$ Decays

We now turn to the discussion of CP violation in B meson decays. The B mesons at ***BABAR*** are produced as the decay products of the $\Upsilon(4S)$ meson which is a vector meson with J=1. The $\Upsilon(4S)$ meson decays into a pair of B mesons which are *coherent* until one of them decays. Coherence of the B mesons means that before decaying one will always be a B^0 and the other a $\overline{B}^0$. We will see in section 5.2 how this helps us identify the B meson flavor at the time of decay. The coherence of

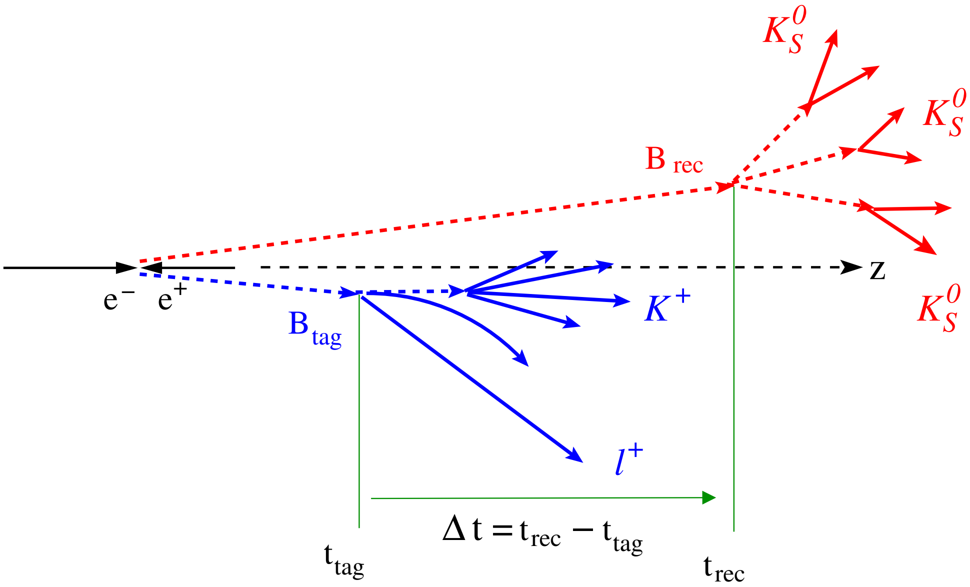

Figure 2.10: Topology of $B^0 \to K_S^0\ K_S^0\ K_S^0$ decay and Δt definition.

the B meson system can be explained by Bose statistics. Since the $\Upsilon(4S)$ is in an antisymmetric p-wave state, the two boson final states f must also be in an antisymmetric state. Bose statistics, however, requires them to be in a symmetric state so the probability of the final states f to be in an antisymmetric state would be zero. This imposes constraints on the coefficients a and b as seen below:

$$\begin{aligned} |B\overline{B}\rangle &= a|B_L B_H\rangle + b|B_H B_L\rangle \\ \langle ff|B\overline{B}\rangle &= 0 \\ a\langle ff|B_H B_L\rangle + b\langle ff|B_L B_H\rangle &= 0 \\ \text{but } \langle ff|B_H B_L\rangle &= \langle ff|B_L B_H\rangle \\ \therefore a &= -b. \end{aligned} \tag{2.42}$$

This means that the two-meson state is antisymmetric in both the mass and flavor eigenstate basis. Therefore states with two B^0 or two $\overline{B}^0$ are vanishing and we have states of the type $|B\overline{B}\rangle$ only.

The fact that the B mesons from the $\Upsilon(4S)$ system are in an entangled state makes the absolute decay time of the B mesons irrelevant. Only the time difference between the two B decays is needed to perform the time-dependent CP measurement. We reconstruct one B in a flavor eigenstate, $B_{\rm tag}$ and with decay time t_{tag} and reconstruct the other in a CP eigenstate called $B_{\rm rec}$ which decays at time $t_{\rm rec}$. The time difference between the decay of the two B mesons $\Delta t \equiv t_{\rm rec} - t_{\rm tag}$ is then used for determining the time-dependent CP asymmetries. We will discuss this further in section 5.2.

In the next two sections we will discuss the time evolution of B mesons in an coherent state and relate the CP asymmetries from B decays to the measurement of the CKM matrix angles.

2.4.1 Time Evolution of B Mesons

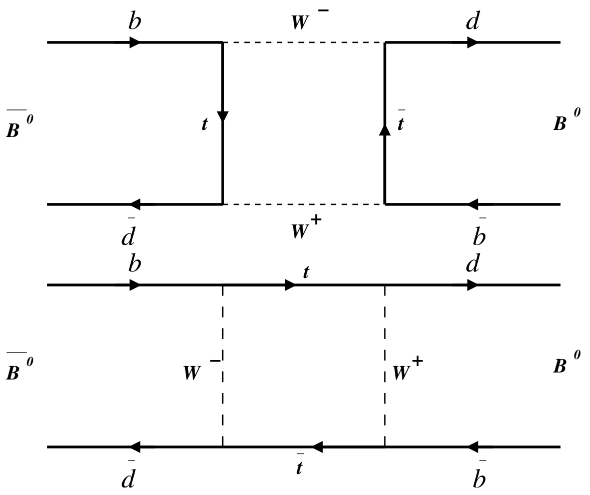

Figure 2.11: Leading diagram contributing to B^0-$\overline{B}^0$ mixing.

Similar to our discussion of neutral mesons we can write the time evolution of B mesons in the mass eigenstates as

$$\begin{aligned} |B_L(t)\rangle &= e^{-im_L t} e^{-\Gamma_L t/2} |B_L\rangle, \\ |B_H(t)\rangle &= e^{-im_H t} e^{-\Gamma_H t/2} |B_H\rangle, \end{aligned} \tag{2.43}$$

and written in terms of the flavor eigenstates as

$$\begin{aligned} |B_L(t)\rangle =& (e^{-(im_H - \Gamma_H/2)t} + e^{-(im_L - \Gamma_L/2)t}) |B^0\rangle + \\ & \frac{q}{p} (e^{-(im_H - \Gamma_H/2)t} - e^{-(im_L - \Gamma_L/2)t}) |\overline{B}^0\rangle \end{aligned} \tag{2.44}$$

$$\begin{aligned} |B_H(t)\rangle =& \frac{q}{p} (e^{-(im_H - \Gamma_H/2)t} - e^{-(im_L - \Gamma_L/2)t}) |B^0\rangle + \\ & (e^{-(im_H - \Gamma_H/2)t} + e^{-(im_L - \Gamma_L/2)t}) |\overline{B}^0\rangle. \end{aligned} \tag{2.45}$$

We can express some physical states in which at $\Delta t = 0$ the flavor is either a B^0 or $\overline{B}^0$ since we will know the flavor of the B at this point. So at $\Delta t = 0$ $|B^0{}_{\rm rec}(0)\rangle = |B^0\rangle$ and $|\overline{B^0}{}_{\rm rec}(0)\rangle = |\overline{B}^0\rangle$ and the time evolution of the states is expressed as

$$|B^0{}_{\rm rec}(\Delta t)\rangle = g_+(\Delta t)|B^0\rangle + (q/p)g_-(\Delta t)|\overline{B^0}\rangle \tag{2.46}$$

$$|\overline{B^0}{}_{\rm rec}(\Delta t)\rangle = (p/q)g_-(\Delta t)|B^0\rangle + g_+(\Delta t)|\overline{B^0}\rangle \tag{2.47}$$

$$g_-(\Delta t) = e^{-iM\Delta t}e^{-i\Gamma\Delta t/2} i\sin(\Delta m_d \Delta t/2) \tag{2.48}$$

$$g_+(\Delta t) = e^{-iM\Delta t}e^{-i\Gamma\Delta t/2} \cos(\Delta m_d \Delta t/2) \tag{2.49}$$

where $\Gamma = 1/\tau_B^0$ and $M = \frac{1}{2}(M_H + M_L)$, and $\Delta m_d = M_H - M_L$.

Since the two B mesons are in a coherent state only the flavor of $B_{\rm tag}$ is needed for describing the probability of the B mesons. The flavor of $B_{\rm rec}$ can be inferred from the flavor of $B_{\rm tag}$. The time-dependent probability functions for the $\Upsilon(4S)$ decay can be written in terms of the flavor of the $B_{\rm tag}$ meson i.e. Γ_{B^0} when $B_{\rm tag}$ is B^0 and $\Gamma_{\overline{B}^0}$ when $B_{\rm tag}$ is $\overline{B}^0$ at $\Delta t = 0$

$$\begin{aligned}
\Gamma_{B^0}(\Delta t) &= \frac{1}{2}|\langle f|T|B^0(t=t_{\rm rec})\rangle\langle B^0(t=t_{\rm tag})|\bar{B}^0(t=t_{\rm tag})\rangle - \\
&\qquad \langle f|T|\bar{B}^0(t=t_{\rm rec})\rangle\langle B^0(t=t_{\rm tag})|B^0(t=t_{\rm tag})\rangle|^2 \\
&= \frac{e^{-\frac{|\Delta t|}{\tau}}}{4\tau}(1 + S_f\sin(\Delta m_d\Delta t) - C_f\cos(\Delta m_d \Delta t)), \qquad (2.50)\\
\Gamma_{\bar{B}^0}(\Delta t) &= \frac{1}{2}|\langle f|T|B^0(t=t_{\rm rec})\rangle\langle \bar{B}^0(t=t_{\rm tag})|\bar{B}^0(t=t_{\rm tag})\rangle - \\
&\qquad \langle f|T|\bar{B}^0(t=t_{\rm rec})\rangle\langle \bar{B}^0(t=t_{\rm tag})|B^0(t=t_{\rm tag})\rangle|^2 \\
&= \frac{e^{-\frac{|\Delta t|}{\tau}}}{4\tau}(1 - S_f\sin(\Delta m_d\Delta t) + C_f\cos(\Delta m_d \Delta t)), \qquad (2.51)
\end{aligned}$$

where

$$S_f = \frac{2{\rm Im}\Lambda_f}{1+|\Lambda_f^2|} \text{ and } C_f = \frac{1-|\Lambda_f^2|}{1+|\Lambda_f^2|}. \tag{2.52}$$

As before,

$$\Lambda_f = \eta_{f_{CP}}\frac{p}{q}\frac{\bar{A}_f}{A_f},$$

where $A = |\langle f|T|B^0\rangle|$, $\bar{A} = |\langle f|T|\bar{B}^0\rangle|$, and $\eta_{f_{CP}}$ is the *CP* eigenvalue of the final state.

The equations above are dependent on Λ_f, which is a useful parameter in the measurement of *CP* violation. An observable sensitive to time-dependent *CP* asymmetry can be written as

$$\begin{aligned}
A_{CP}(\Delta t) &= \frac{\Gamma_{B^0}(\Delta t) - \Gamma_{\overline{B}^0}(\Delta t)}{\Gamma_{B^0}(\Delta t) + \Gamma_{\overline{B}^0}(\Delta t)} \\
&= S\sin(\Delta m_d\Delta t) - C\cos(\Delta m_d\Delta t), \qquad (2.53)
\end{aligned}$$

so that the amplitude of the $\sin$ and $\cos$ term give us the value of Λ_f. Integrating over $A_{CP}(\Delta t)$ from $-\infty$,$+\infty$ we see that the sine term vanishes since it's an odd function of Δt. We therefore have to measure the S_f term by performing a time-dependent measurement. We will discuss how this is done experimentally in the coming chapters.

2.4.2 Measurement of Unitarity Triangle Parameters in B decays

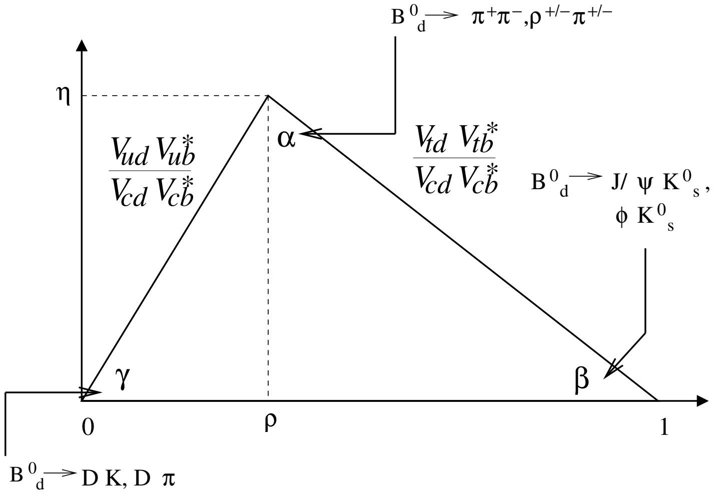

Figure 2.12: The CKM matrix triangle and some of the decay modes which allow measurement of the angles β, α, and γ.

Each angle of the CKM triangle can be measured through a *CP* violating amplitudes in decays which include the particular modes shown in fig. 2.12. Of particular interest for the analysis reported in this dissertation is the angle β. For a discussion of techniques for measurement of the other two angles, α and γ, the reader is referred to the *BABAR* Physics Book [5].

The "golden mode" for measuring β is the decay $B^0 \rightarrow J/\psi\ K^0_S$ since it has a clear theoretical interpretation and can be experimentally measured with great precision. *CP* violation in this channel will be shown to be entirely due to interference of mixing with the direct decay, with an time-dependent amplitude that is proportional to $\sin 2\beta$. Fig 2.13 shows the two Feynman diagrams contribution for the decay of $B^0 \rightarrow J/\psi\ K^0_S$. The leading contribution comes from the tree diagram with the penguin diagram being highly suppressed. This means that only one phase is dominant in the decay making this mode theoretically easy to interpret. The level of *CP* violation in this mode serves as a benchmark against which to compare the rare decays, like the $B^0 \to K^0_S\, K^0_S\, K^0_S$ decay, where the CP violating amplitude should also be $\sin 2\beta$ in the SM up to some hadronic corrections.

For this decay mode Λ_f is given by

$$\Lambda_f = \frac{q}{p}\frac{\overline{A}}{A}\left(\frac{q}{p}\right)_K , \tag{2.54}$$

where

$$\left(\frac{q}{p}\right)_K = \frac{V_{cs}V^*_{cd}}{V^*_{cs}V_{cd}}e^{2i\eta_K}, \tag{2.55}$$

is due to mixing between $K^0 - \overline{K}^0$, the process is similar to the box diagram shown for B mixing in fig. 2.11. The K^0 meson is made of $\overline{s}d$ and a $\overline{K}^0$ meson is made of $s\overline{d}$ quarks. The box digram is dominated by the exchange of virtual charm quarks. The ratio q/p due to mixing in the B system (fig. 2.11) is dominated by the exchange of virtual top quark

$$\frac{q}{p} = \frac{V^*_{tb}V_{td}}{V_{tb}V^*_{td}}e^{2i\eta_B} \tag{2.56}$$

As seen in fig. 2.13 the weak transitions of interest in the tree diagram are V_{cb} and V_{cs}. So the ratio $\overline{A}/A$ becomes

$$\frac{\overline{A}}{A} = \eta_f\left(\frac{V_{cb}V^*_{cs}}{V^*_{cb}V_{cs}}\right)e^{-2i\eta_B}, \tag{2.57}$$

then

$$\begin{aligned}\Lambda_f = \eta_f\frac{V_{cs}V^*_{cd}}{V^*_{cs}V_{cd}}\frac{V^*_{tb}V_{td}}{V_{tb}V^*_{td}}\frac{V_{cb}V^*_{cs}}{V^*_{cb}V_{cs}} &= \eta_f e^{2i\beta} \\ \Rightarrow \eta_f \mathrm{Im}\Lambda_f &= \eta_f \sin 2\beta \end{aligned} \tag{2.58}$$

where the phases $e^{2i\eta_B}$ and $e^{2i\eta_K}$ are absorbed by rephasing. The time-dependent asymmetry is given by

$$A_{CP} = -\eta_f \sin 2\beta \sin \Delta m_d \Delta t \tag{2.59}$$

Thus, the experimentally measurable amplitude for time-dependent CP violation directly gives us the CKM angle β.

2.5 The $B^0 \to K^0_S\, K^0_S\, K^0_S$ decay

This section explains penguin decay amplitudes and how it measures $\sin 2\beta$ in the SM up to some theoretical deviation, $\Delta \sin 2\beta_{K^0_S K^0_S K^0_S}$. There are two theoretical models used for determining this deviation. One is QCD factorization and the other is $SU(3)$ flavor symmetry. These models are explained in the sections to follow showing the theoretical predictions of the time-dependent asymmetries from the $B^0 \to K^0_S\, K^0_S\, K^0_S$ decay.

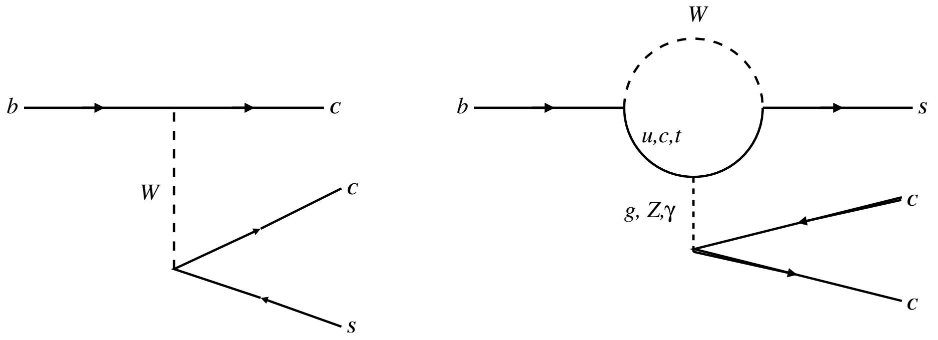

Figure 2.13: Feynman diagram of the $B^0 \to J/\psi\ K^0_S$ decay via a tree (left) and penguin decay (right).

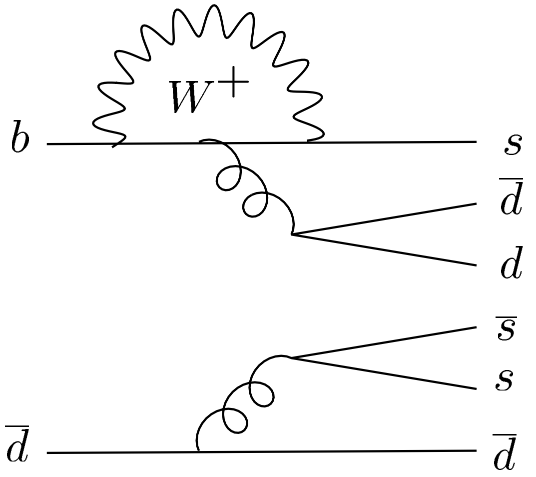

Figure 2.14: Feynman diagram of the $B^0 \to K^0_S\ K^0_S\ K^0_S$ decay via the dominant $b \to sd\overline{d}$ penguin mechanism.

2.5.1 Penguin Decays

The decay of $B^0 \to K^0_S\ K^0_S\ K^0_S$ occurs through a penguin diagram involving a transition $b \to sd\overline{d}$ shown in fig. 2.14 The amplitude of $b \to s$ penguin decays can be written as [5]

$$A(q\overline{q}s) = V_{tb}V^*_{ts}P^t_s + V_{cb}V^*_{cs}(T_{c\overline{c}s}\delta_{qc} + P^c_s) + V_{ub}V^*_{us}(T_{u\overline{u}s}\delta_{qu} + P^u_s) \tag{2.60}$$

where P and T denote contributions from tree and penguin diagrams respectively. Written as above the P terms are divergent and not well defined. Only differences of penguin diagrams are finite and well defined [5]. In the case of $b \to s$ penguin decays we can use the unitarity condition equation 2.23 to replace the $V_{tb}V^*_{ts}$ term to obtain

$$A(q\overline{q}s) = V_{cb}V^*_{cs}(T_{c\overline{c}s}\delta_{qc} + P^c_s - P^t_s) + V_{ub}V^*_{us}(T_{u\overline{u}s}\delta_{qu} + P^u_s - P^t_s). \tag{2.61}$$

Once again we see the familiar term $V_{cb}V_{cs}$ which occurred in the $B^0 \to J/\psi\ K^0_S$ decay. The $V_{ub}V_{us}$ term is suppressed with respect to the first term by $\mathcal{O}(\lambda^2)$. A theoretically clean interpretation of the amplitude for CP violation in terms of CKM angles requires that only one phase dominates the decay amplitude. For the case of the $B^0 \to J/\psi\ K^0_S$ decay only the tree amplitude is dominant therefore making the result easy to interpret. The $B^0 \to K^0_S\ K^0_S\ K^0_S$ decay is considered theoretically clean since the $V_{tb}V_{ts}$ term is dominant and the $V_{cb}V_{cs}$ is suppressed with no tree contributions which could interfere. The $b \to u\overline{u}s$ tree diagram followed by rescattering into $s\overline{s}s$ or $s\overline{d}d$ is OZI suppressed [15]. The OZI rule states that strong interaction processes where the final states can only be reached through quark/anti-quark annihilation are suppressed. The quark-level amplitudes however are just a way of classifying the B decays. The actual calculation of B decay amplitudes are complicated by hadronic interaction between quarks which can cause final state interactions and rescattering.

There has been great experimental activity in the measurement of penguin decay modes in search of new physics. The $b \to sq\overline{q}$ penguin modes are dominated by one-loop transitions where new physics at high mass scales can also contribute through the exchange of new virtual particles. Contributions from physics beyond the SM, like the SUSY diagram shown in fig. 2.15, could lead to different levels of CP violation than predicted by the SM, making these decays specially sensitive to new physics.

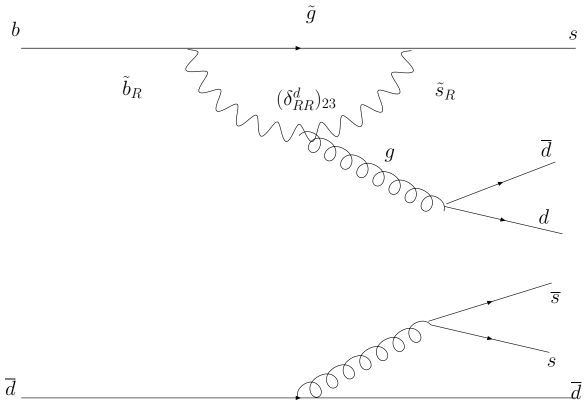

Figure 2.15: Feynman diagram of the $B^0 \to K^0_S\ K^0_S\ K^0_S$ decay via an intermediate SUSY particle in the loop.

BABAR has performed time-dependent CP measurements of the penguin modes $B^0 \to \phi K^0_S$, $f_0 K^0_S$, $K^+K^-K^0_S$, ωK^0_S, $\eta' K^0_S$, ηK^0_S, $\pi^0 K^0_S$, and $\rho^0 K^0_S$. The "golden mode" for discovering potential new physics is the $B^0 \to \phi K^0_S$ mode [16] [17]. The $B^0 \to K^0_S\ K^0_S\ K^0_S$ mode has also recently been deemed a "golden mode" as well since, within the SM, the amplitude for CP violation is expected to deviate very little from $\sin 2\beta$ measured from charmonium modes and the fact that it's a purely *CP* even final state [18]. Other states, in particular the $B^0 \to K^+K^-K^0_S$ decay, have both a *CP* even and odd component, with no a priori prediction for the breakdown, making it difficult to interpret the results.

2.5.2 CP Content of $B^0 \to K^0_S\, K^0_S\, K^0_S$

The $B^0 \to K^0_S\, K^0_S\, K^0_S$ decay is *CP* even. We can demonstrate this by splitting the system into $(K^0_S\, K^0_S)_{\mathrm{L}}$ and $K^0_S\,{}_{\mathrm{L}'}$, where L is the angular momentum of the $(K^0_S\, K^0_S)$ system and L′ is the angular momentum of K^0_S with respect to the $(K^0_S\, K^0_S)$ system. Because of Bose statistics the $(K^0_S\, K^0_S)$ system must be in a symmetric state making L even. So the *CP* of the $(K^0_S\, K^0_S)$ system can be written as [18]

$$\begin{aligned} CP(K^0_SK^0_S) &= C(K^0_SK^0_S) \times P(K^0_SK^0_S) = C(K^0_S)^2 \times P(K^0_S)^2 \times (-1)^L \\ &= CP(K^0_S)^2 \qquad (2.62) \\ &= +1 \qquad (2.63) \end{aligned}$$

where we assume K^0_S is a *CP* eigenstate. Imposing conservation of angular momentum we get

$$\begin{aligned} \mathbf{J}^0_B &= \mathbf{L} + \mathbf{L}' + 3\mathbf{S}_{K^0_S} \\ 0 &= \mathbf{L} + \mathbf{L}' \qquad (2.64) \end{aligned}$$

so L′ must equal L. Then we can write the *CP* of $K^0_S\, K^0_S\, K^0_S$ as

$$\begin{aligned} CP(K^0_SK^0_SK^0_S) &= CP(K^0_SK^0_S) \times CP(K^0_S) \times (-1)^{L'} \\ &= CP(K^0_S) \qquad = 1. \qquad (2.65) \end{aligned}$$

Thus the decay $B^0 \to K^0_S\, K^0_S\, K^0_S$ is a *CP* eigenstate with the same *CP* as K^0_S which is $+1$.

2.5.3 Theoretical Models

Several very recent phenomenology references attempt to predict via $SU(3)$ flavor symmetry and QCD factorization the size of any deviations between the level of *CP* violation $\sin 2\beta$ in the mode $B^0 \to K^0_S\, K^0_S\, K^0_S$ and $\sin 2\beta$ as measured in the mode $B^0 \to J/\psi\, K^0_S$. The factorization model allows us to write the effective weak Hamiltonian as [19]

$$\langle K^0_S(p1)K^0_S(p2)K^0_S(p2)|\mathcal{H}_{\mathrm{eff}}|B^0\rangle = \frac{G_F}{\sqrt{2}} \sum_{p=u,c} \lambda_p \langle K^0_S(p1)K^0_S(p2)K^0_S(p3)|T_p|B^0\rangle, \qquad (2.66)$$

where $\lambda_p \equiv V_{pb}V^*_{ps}$ and T_p is a sum of vector-vector and pseudoscalar-pseudoscalar modes with coefficients called *Wilson coefficients*. Each matrix element can then be written in a factorized form such that

$$\begin{aligned}\langle K^0_S(p1)K^0_S(p2)K^0_S(p3)|j\otimes j|B^0\rangle \Rightarrow &\langle K^0_S(p1)K^0_S(p2)|j|B^0\rangle\langle K^0_S(p3)|j|0\rangle,\\ &\langle K^0_S(p1)|j|B^0\rangle\langle K^0_S(p2)K^0_S(p3)|j|0\rangle, \text{or}\\ &\langle 0|j|B^0\rangle\langle K^0_S(p1)K^0_S(p2)K^0_S(p3)|j|0\rangle. \end{aligned} \tag{2.67}$$

This calculation leads to a bound on the difference between the mixing-induced *CP* asymmetry in $B^0 \to K^0_S\, K^0_S\, K^0_S$ and $B^0 \to J/\psi\ K^0_S$, $\Delta\sin 2\beta_{\text{eff}} \equiv \sin 2\beta_{\text{eff}} - \sin 2\beta_{J/\psi\, K^0_S}$

$$\Delta\sin 2\beta_{K^0_S K^0_S K^0_S} = 0.02^{+0.00}_{-0.04}. \tag{2.68}$$

Thus, we see that the deviation is expected to be very small [19].

The $SU(3)$ calculation provides a less stringent bound on $\Delta\sin 2\beta_{\text{eff}}$. This calculation relies on the knowledge of branching fractions for other three-body channels, some of which have not yet been observed and exist only as limits [20]. Using the symmetry of the $|K^0_S K^0_S K^0_S\rangle$ final state we can write the decay amplitude of $B^0 \to K^0_S\, K^0_S\, K^0_S$ as

$$\vec{A}_{3K^0_S} = \left(V^*_{cb}V_{cs}\vec{a}^c_{\mathcal{S}}(K^0K^0\overline{K}^0) + V^*_{ub}V_{us}\vec{a}^u_{\mathcal{S}}(K^0K^0\overline{K}^0)\right)\sqrt{3/8}[V^*_{cs}V_{cd}/|V^*_{cs}V_{cd}|]. \tag{2.69}$$

We can introduce a parameter ξ

$$\xi \equiv \frac{|V^*_{ub}V_{us}|}{|V^*_{cb}V_{cs}|}\frac{\vec{a}^c_{\mathcal{S}}(K^0K^0\overline{K}^0)\cdot\vec{a}^u_{\mathcal{S}}(K^0K^0\overline{K}^0)}{||\vec{a}^c_{\mathcal{S}}(K^0K^0\overline{K}^0)||^2}, \tag{2.70}$$

which gives a measure of $\Delta\sin 2\beta_{K^0_S K^0_S K^0_S}$ through the relation

$$\Delta\sin 2\beta_{K^0_S K^0_S K^0_S} = 2\cos 2\beta\sin\gamma\Re(\xi). \tag{2.71}$$

Using $SU3$ relations we can bind $\Re(\xi) < 0.31$. Using the values of $\sin 2\beta = 0.73$ and $\gamma = 50$ gives a very loose bound of $\Delta\sin 2\beta_{K^0_S K^0_S K^0_S} < 0.32$. $SU(3)$ breaking effects can be as large as 30% however so this result cannot be trusted to better accuracy than that.

Chapter 3

The *BABAR* Experiment

The PEP-II asymmetric collider is one of two B factories in the world. The main goal of the B factories is to measure *CP* violation in B decays. In order to perform such measurements it is necessary to measure the time difference of the decay of the two B mesons. The lifetime of the B meson is 1.5 ps which translates to about a distance of 30 microns in the center of mass frame of the meson pair. While running at high luminosities, this distance is too small to be measured by current detectors therefore the decay is boosted in the lab frame to achieve larger spatial separation of the decays and hence allow us to measure the time difference.

The other challenge which faces the B factory is running at high luminosities since the branching fraction of the $\Upsilon(4S)$ decay to B mesons is small, 10^{-4}. The PEP-II storage rings address both of these issues by storing particles of asymmetric energies and operating at high luminosities.

A key ingredient for performing time-dependent *CP* measurements is determining the flavor of the tag side B. *BABAR*'s excellent particle identification and tracking system allow for this.

The sections to follow show how the *BABAR* detector and PEP-II accelerator address the challenges for performing time-dependent *CP* measurements. A full detailed description of PEP-II and the *BABAR* detector can be found at [21].

3.1 PEP-II

PEP-II consists of two separate storage rings for electrons and positrons that are arranged in a single 2.2-km long tunnel on the SLAC site. The two beams are brought into collision at one interaction region, where the *BABAR* detector is located. PEP appropriately stands for *Positron Electron Project*; PEP-II is an upgrade of the original storage PEP ring which was constructed between October 1993 and May 1999.

3.1.1 Design

PEP II is an asymmetric energy e^+e^- storage rings operating at a center-of-mass energy of $10.580\ \mathrm{GeV}$, which is the mass of the $\Upsilon(4S)$ resonance. The collider has two components, the $9.0\ \mathrm{GeV}$ high energy ring (HER) which store the electrons and a $3.1\ \mathrm{GeV}$ low energy ring (LER) storing the positrons. The 2200 meter long PEP-II rings are filled by SLAC's 2 mile long linear accelerator. An aerial view of PEP-II and the storage rings is shown in fig. 3.1.

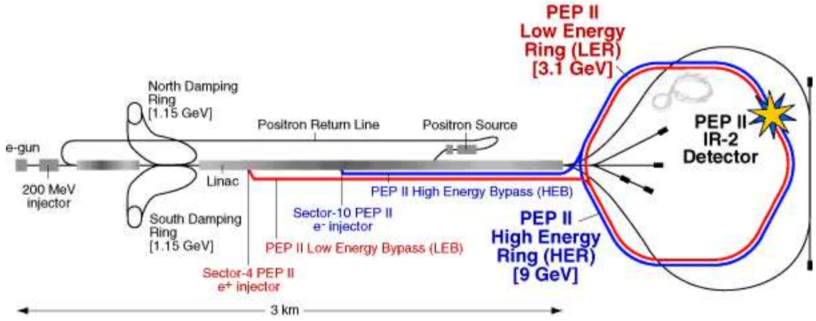

Figure 3.1: Schematic drawing of SLAC's linear accelerator and PEP-II.

The beams consist of some 1600 individual bunches spaced at about 8 foot intervals circulating in vacuum systems in the rings. The beams are brought into head-on collision at one interaction point alone which is also in high vacuum. This is accomplished by a pair of dipole bending magnets. Two pairs of quadrupole magnets on each side of the interaction region provide final focusing of the HER and LER beams to maximize the probability of collisions. The bending magnets and two of the quadrupoles are located close to the IP in the solenoidal magnetic field of the *BABAR* detector. To minimize perturbation of the beam from the solenoid field, the collision axis is offset by 20 mrad in the horizontal plane. These requirements define the solid angle acceptance for the detector and therefore the overall efficiency for B meson reconstruction.

The IP region is surrounded by a 27.9 mm radius tube, called the beam pipe, with a 1.48 mm water channel for cooling the region. The inner layer of the tube is coated with a thin layer of gold to reduce the effect of synchrotron radiation. The beam pipe, permanent magnets, and the SVT are housed in a 4.5 m long support tube which covers the IP region. The support tube is mounted on the PEP-II accelerator supports allowing movement of the SVT with respect to the rest of *BABAR*.

In the detector $\Upsilon(4S)$ mesons are created with a boost of $\beta\gamma = 0.55$ in the lab frame along the high energy beam direction. With this boost the B mesons of the decay travel an average of 260

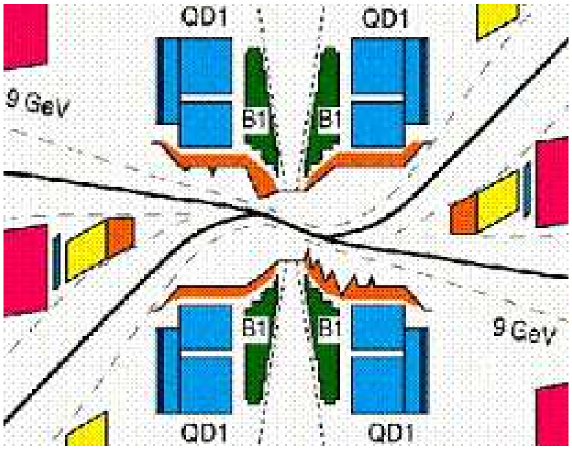

Figure 3.2: Schematic view of magnets and interaction region.

microns before decaying, as opposed to 30 microns in the rest frame. In order to study the decay properties of the processes $e^+e^- \to q\overline{q}$ with $q = u, d, s, c$, the machine is operated at an energy of 40 MeV below the $\Upsilon(4S)$ resonance (off-resonance data). These events represent most of the combinatorial background in certain decays.

3.1.2 Performance/Luminosity

The first beams delivered to *BABAR* for data taking with the completed detector was in October 1999. Data acquisition since then has been conveniently divided into four running periods. By July 2004, the full sample consisted of 244.0 fb^{-1}, as shown in fig. 3.3. The peak luminosity achieved is $9.213\mathrm{x}10^{33}\,\mathrm{cm}^{-1}\,\mathrm{s}^{-1}$ which is almost three times higher than the design specifications. Other operating parameters are shown in table 3.1.2.

The characteristics of the beam energy directly effect physics variables used for analysis as seen in section 4.2.2. The beam-energy is calculated from the total magnetic bending strength and the average deviations of the accelerating frequencies from their central values. The energy setting of each beam is accurate and stable to about $1\,\mathrm{MeV}$ with an rms energy spread of 2.3 MeV for the LER and 5.5 MeV for the HER.

The high luminosity achieved by PEP-II poses a problem of radiation damage and large backgrounds seen in the detector. The major sources of backgrounds are from synchrotron radiation near the interaction region, beam-gas interactions, and electromagnetic showers from beam-beam interactions. The beam orbits, vacuum-pipe aperture, and synchrotron radiation masks are designed such that most of photons produced in the dipole and quadrupole magnets in the final focus are dumped outside the detector. Beam-gas backgrounds from bremsstrahlung and Coulomb scattering off of gas molecules was reduced in the first year of running by scrubbing of residual absorbed surface gasses on the vacuum surface. These types of backgrounds are the major source of radiation to the SVT and the dominant background in most other detectors. Finally electromagnetic showers from radiative Bhabha scattering are a source of background which scales with the luminosity. Comparisons of data taken from beams in collision and beams separated show larger EMC crystal occupancy and higher trigger rates. This increase is due to the flux of photons originating from small angle radiative Bhabha scattering. This effect will increase with luminosity and therefore limit the EMC energy resolution.

Table 3.1: PEP-II design and highest luminosity operating parameters. LER and HER refer to the high energy e^- and low energy e^+ ring respectively. σ_x, σ_y, and σ_z refer to the horizontal, vertical, and longitudinal size of the luminous region.

Parameters	Design	Best/typical
Energy HER/LER (GeV)	$9.0/3.1$	$9.0/3.1$
Current HER/LER (A)	$0.75/2.15$	$2.450/1.55$
Number of Bunches	1658	1588
Bunch spacing (ns)	4.2	$6.3 - 10.5$
σ_x (μm)	110	120
σ_y (μm)	3.3	5.6
σ_z (mm)	9	9
Luminosity ($10^{33}\text{cm}^{-2}\text{s}^{-1}$)	3	9.213
Luminosity ($\text{pb}^{-1}/\text{day}$)	135	710.5

3.2 Detector

The *BABAR* detector is made of five sub-detectors used for tracking and/or particle identification. The tracking components of the detector operate in a 1.5 T magnetic field produced by the super-conducting solenoid. The detector center is shifted by 37 cm with respect to the Interaction Point (IP) in the direction of the LER to increase detection acceptance of the boosted system.

The detector is designed to have a minimum amount of material in the tracking region before

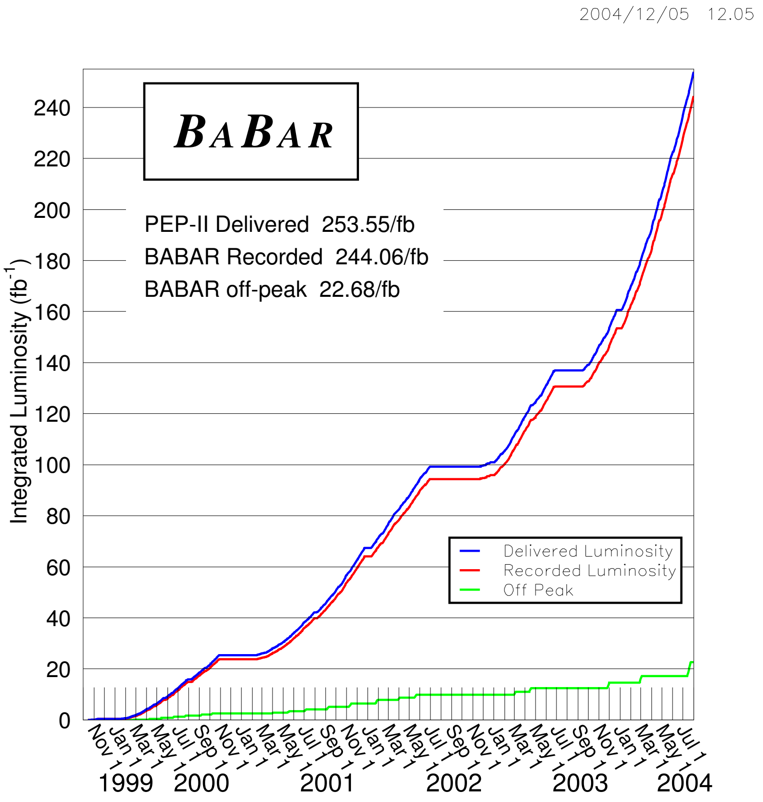

Figure 3.3: *BABAR* integrated luminosity from October 1999 to July 2004.

reaching the Calorimeter to avoid multiple scattering of tracks and enhance detection of low energy photons. The Silicon Vertex Tracker (SVT) and the Drift Chamber (DCH) provide optimal tracking capability over a wide range of momenta. The SVT is positioned close to the IP and provides excellent vertex resolution and tracking for low momentum particles. The DCH determines the momentum of charged particles to a great precision. The next detector going radially out from the center is the Detector of Internally Reflected Cherenkov light (DIRC) which provides particle identification for higher momentum particles. Next is the Electromagnetic Calorimeter which measures the electromagnetic energy deposited in the crystals. Then the outermost sub-detector is the Instrumented Flux Return (IFR) which aids in muon identification and neutral hadron detection. Longitudinal and transverse diagrams of the detector are shown in fig. 3.4.

3.2.1 Silicon Vertex Tracker (SVT)

The SVT is designed to measure the angle and position of charged tracks to great precision. This level of precision is defined by the need to determine the B longitudinal decay vertex position,

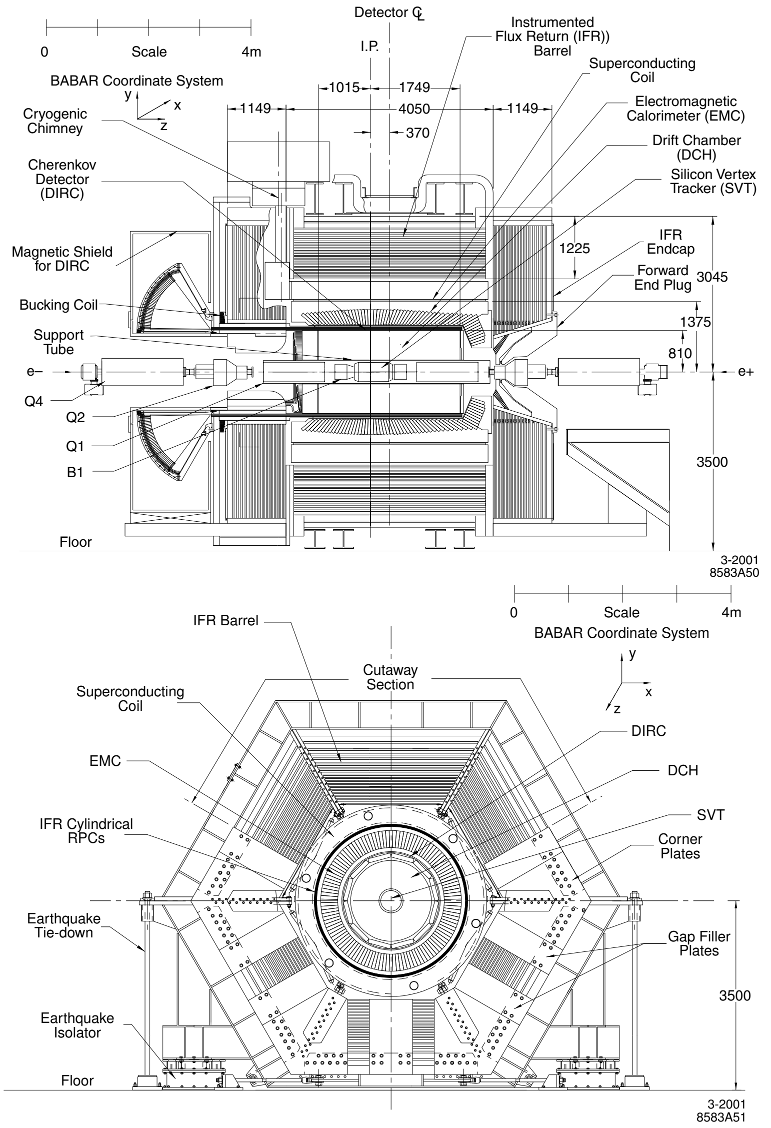

Figure 3.4: $y-z$ (left) and $x-y$ (right) cross-section schematic of *BABAR* detector

which translates into the time decay difference needed for time-dependent CP violation measurements. The track measurements are also important for extrapolating to the DIRC, EMC, and IFR and directly effect the angular measurements of the DIRC. The hit resolution of the SVT is about 10-15 μm in the inner layers and about 40 μm in the outer layers. The required vertex resolution for doing CP measurements is 80 μm in the $x-y$ plane and 100μm in the z plane and is achieved by the hit resolutions quoted earlier. The SVT also aids in finding low momentum tracks, $< 120\,\mathrm{MeV}/c$ which cannot be reliably detected by the DCH. This is a key factor for identifying slow pions from D^* decays which can be used for B tagging, see sec 5.1.1.

The design and coverage of the SVT is mostly constrained by the dipole magnets used to bring the beams into collision. In the forward direction it covers up to 350 mrad in polar angle from the beam line and 520 mrad in backward direction. This sub-detector is made of five layers of 340 double-sided silicon strip wafers mounted on a carbon-fiber frame. The silicon semiconductor works basically as a reversed bias p-n junction; when a charged particle traverses the volume it creates an electron-hole pair which under a voltage will flow to the surface where it is measured by charge integrating contacts. The detector is separated into p-n junction strips with individual readouts so that the path of the particle can be traced by the location of the strips which produce a signal.

The sensors on each side of the wafers are orthogonal to each other allowing for both a z and ϕ position measurement of the track and provide 150,000 channels of information. To avoid having too much material in the acceptance region, which causes scattering, the readout electronics are all housed in the backward region of the SVT, outside the fiducial volume. The inner three layers are placed close to the beam-pipe to determine position and angle of the B vertex while the outer two are placed closer to the DCH for extrapolating tracks into the DCH. Fig. 3.5 shows the longitudinal and transverse schematic drawings of the SVT.

3.2.2 Drift Chamber (DCH)

The main purpose of the DCH is to determine the momentum of charged particles in the plane transverse to the beam. A particle must have a minimum transverse momentum of 50 MeV to reach the DCH and a momentum of about 120 MeV to be reliably reconstructed. The DCH measures 280 cm long and occupies the radial volume from 23.6 to 80.9 cm. This area is filled with a 80:20 mixture of helium and isobutane gas at 4 mbar above the atmospheric pressure. Charged particles traveling in the DCH ionize the gas thereby creating electrons which drift along field lines to sense wires at the center of each drift chamber cell. Near the sense wire, the electron causes an avalanche in the locally high field gradient, resulting in a detectable signal that can be used to measure the drift time. With the help of a time-to-distance relation one can relate the drift time to the distance away from the wire in a given cell.

The DCH is made of 40 layers of 7104 hexagonal shaped cells of about 1 cm width. Each cell contains a sense wire surrounded by six field wires, see fig 3.6. The aluminum field wires are held at a ground potential while the tungsten-rhenium sense wires are held at a positive high voltage of 1930 V.[1]

---

[1] DCH operated at voltage of 1960V from , a voltage of 1900 V from, and a voltage of 1930 V from till present.

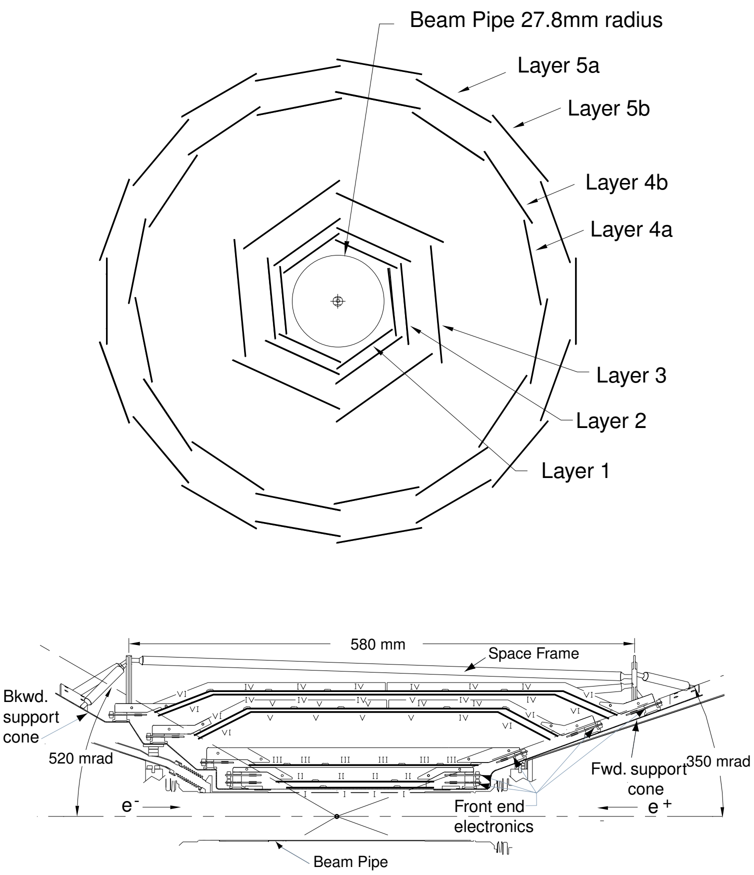

Figure 3.5: $x-$ (left) and $y-z$ (right) cross-section schematic of *BABAR* SVT.

The layers of the DCH are organized in subsets of 4 layers, or 10 superlayers. Four of the ten superlayers are axial layers where the wires run parallel to the axis of the chamber and the remaining six are stereo layers where they are rotated by some angle. The stereo superlayers alternate in stereo angle rotation to allow a determination of the z-coordinate of the tracks. The axial layers determine the ϕ-coordinate of the track.

At low momentum the DCH energy loss per unit distance can be used for particle identification. The transverse momentum resolution of the track is given by:

$$\sigma p_T = (0.13 \pm 0.01)\% p_T + (0.45 \pm 0.03)\% \tag{3.1}$$

3.2.3 Detector of Internally Reflected Cherenkov Light (DIRC)

The DIRC is perhaps the most innovative sub-detector providing particle identification at high momentum by measuring Cherenkov radiation from particles traveling through synthetic fused silica bars. The DIRC is used for separating kaons and pions which is useful for flavor identification in

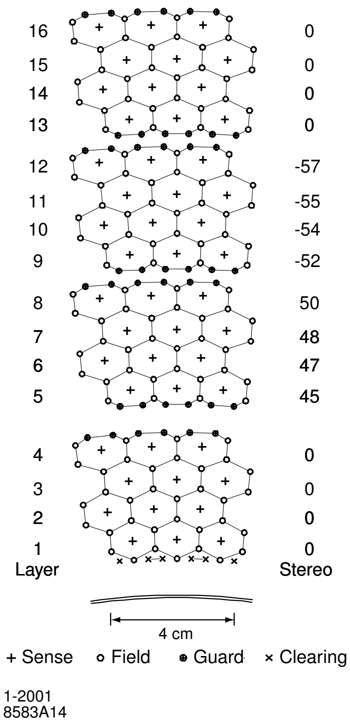

Figure 3.6: Schematic layout of DCH cells for the four inner superlayers. The numbers on the right indicate the stereo angle for each layer.

cascade processes like $b \rightarrow c \rightarrow s$. It is also used for separating two-body charmless decays to pions and kaons to great precision. The DIRC can measure photon arrival time to an accuracy of 1.7 ns, which allows it to distinguish signal and background in a high luminosity environment.

The $1444\ 9\,\mathrm{m} \times 1.7\,\mathrm{cm} \times 3.5\,\mathrm{cm}$ silica bars are arranged into a 12-sided polygonal barrel. The light produced is transmitted through total internal reflection to the array of photomultiplier tubes at the backward end of the magnet (see fig. 3.7). Before reaching the PMT, the light passes through a water filled standoff box and produces rings of light in the shape of cones. The opening angle of the cone is the Cherenkov production angle modified by refraction at the end of fused silica bars. Upon exiting the bars the photons are focused on the PMT through the aperture of the bar which acts as a pinhole source. The vector pointing from the center of the bar end to the center of each PMT is taken as the photon propagation angle. Together with the polar angle measured from the tracking system which can be associated with the photon transversing the bar one can determine the Cherenkov angles. The timing info from the PMTs provides an extra constraint on the system which can help in identifying backgrounds and ambiguous signal.

The DIRC has a $K - \pi$ separation power of 4σ at $3\ \mathrm{GeV}$, but for tracks of order $0.7\ \mathrm{GeV}$ the

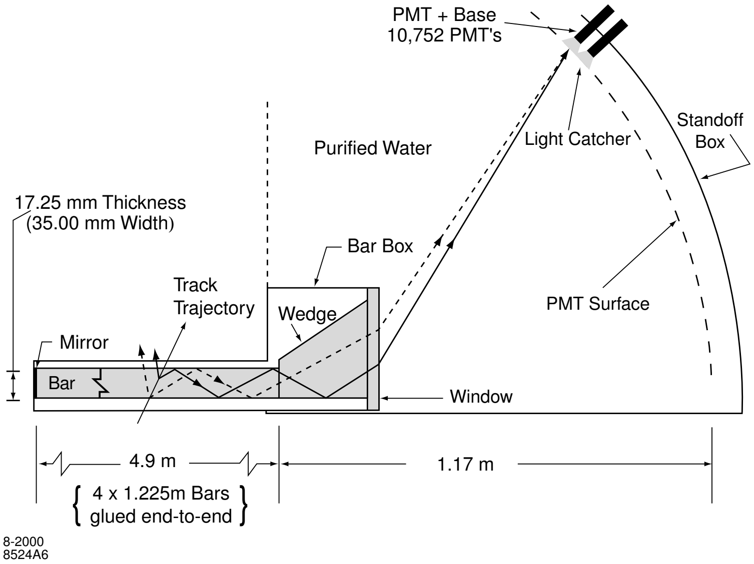

Figure 3.7: Schematic drawing illustrating the detection of Cherenkov photons by the DIRC.

SVT and DCH $\mathrm{d}E/\mathrm{d}x$ is used for particle identification. The average resolution on the Cherenkov angle is 2.5 mrad and the timing resolution is such that photons from different beam crossings are distinguished as separate events.

3.2.4 Electromagnetic Calorimeter (EMC)

The EMC is designed to measure electromagnetic showers with excellent resolution in angle and energy for particles ranging in energy from $20\,\mathrm{MeV}$ to $9\,\mathrm{GeV}$. This allows for detection of photons from π^0 or η^0 decays, and electromagnetic and radiative processes. Lepton identification aids in flavor tagging of neutral B decays. QED processes like $e^+e^- \rightarrow e^+e^-\gamma$ and $e^+e^- \rightarrow \gamma\gamma$ are used for calibrations and luminosity determinations. At the low energy detection scale is set by the need to reconstruct π^0 or η^0 from B decays. Below energies of 2 GeV π^0 reconstruction is dominated by energy resolution, 1-2%, and at higher energies by the angular resolution.

The EMC is made of 6,580 Cesium-Iodide crystals doped with a small amount of Thalium. Most of the crystals cover the barrel region of the detector in ϕ, (see fig 3.8), and about 10% are in the forward end-cap region, the direction of the boost to achieve larger acceptance. The EMC is more than 96% efficient for photons with energy greater than 20 MeV. The energy resolution is given by

$$\frac{\sigma(E)}{E} = \frac{2.32 \pm 0.30)\%}{E^{1/4}} \pm (1.85 \pm 0.12)\%. \tag{3.2}$$

The angular resolution is determined from the reconstruction of π^0 and η^0, which decay into two photons, and is

$$\sigma(\phi) = \sigma(\theta) = \frac{3.87 \pm 0.07)\%}{E(\,\mathrm{GeV})^{1/2}} \pm (0.00 \pm 0.04)\mathrm{mrad}. \tag{3.3}$$

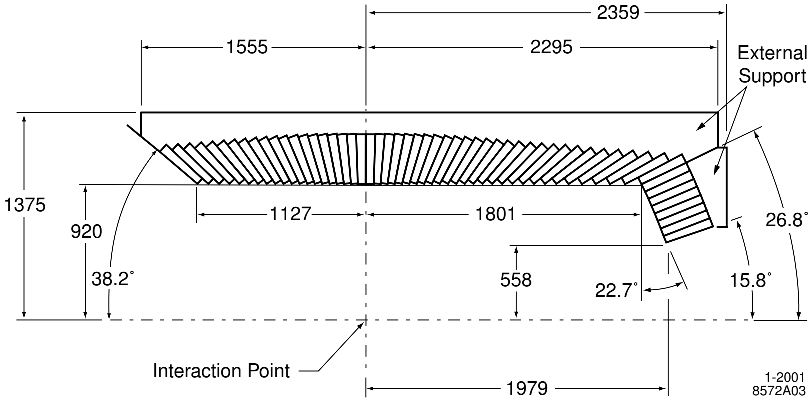

Figure 3.8: Schematic drawing of top half of EMC in y-z. Dimensions are in mm.

3.2.5 Internal Flux Return (IFR)

The IFR is used for muon and neutral hadron identification over a wide range of angles and momenta. The detection of muons is essential for determining the flavor of a B decaying semileptonically. The relative fraction of muon tags to all other flavor tagged channels is about 6%. This lepton channel suffers from a much lower flavor identification uncertainty, however, making the relative effective efficiency about twice as high, (see sec. 5.1.3). K_L^0 detection allows for reconstruction of B meson decays in additional CP eigenstates.

The IFR is instrumented with 806 Resistive Plate Chambers (RPC) placed between the steel plates that make up the magnet flux return for the detector. The RPCs are sandwiched between layers of steel increasing from thickness from 2 cm in the inside to 10 cm on the outside. There are 19 layers of RPCs in the barrel section and 18 layers in the end caps (see fig. 3.9).

Muons with at least 1 GeV of energy travel through the RPCs where they are detected by limited streamer discharge. Particles are identified as muons if they have a long penetration distance in the iron. A K_L^0 produces a larger cluster in the RPCs when it interacts in the iron, with the additional signature of having no track leading to the energy deposition.

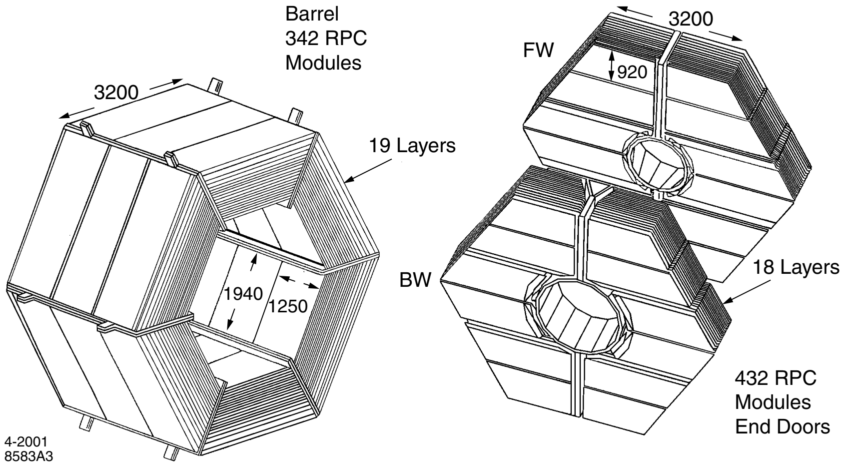

Figure 3.9: Schematic drawing of IFR barrel and endcap.

3.2.6 Trigger

There are two levels of trigger used on the *BABAR* experiment. The first, *Level 1* trigger, is a hardware trigger operating at 2 kHz during normal running. The second is a software trigger *Level 3* operating at $\sim$ 200 Hz for physics and $\sim$ 100 Hz for other special event categories. The trigger is used to reject the uninteresting events and accept the ones which would be of physics interest in an efficient and unbiased method while keeping the total event rate under 120 Hz. The rates for the Level 1 trigger for events of interest are shown in table 3.2. The Level 1 trigger operates on a 11-12 μs latency with respect to the e^+e^- collisions and delivers triggers to the Fast Control and Timing System (FCTS). The Level 1 accept algorithm is based on charged track candidates in the DCH, showers in the EMC, and tracks in the IFR. The hardware for the Level 1 trigger is stored in several VME crates associated with each subsystem. Once a valid trigger remains a Level 1 accept is issued and events are read out and sent to the software Level 3 trigger. The Level 1 trigger takes approximately 1 μs to receive the accept from the FCTS and initiate readout from the Read Out Modules (ROM).

The Level 3 trigger runs on the assembled events, and so can use sophisticated algorithms based on complete events to reduce background and keep interesting events. The software runs on commercial machines (*nodes*) which run the Online Processing Software (OEP) which partially reconstructs the event in order to apply the Level 3 trigger and also provide plots for monitoring data to people on shift.

Table 3.2: Cross sections, production and trigger rates for the principal physics processes at 10.58 GeV for a luminosity of $3 \times 10^{33}\,\mathrm{cm}^{-2}\mathrm{s}^{-1}$. The e^+e^- cross section refers to events with either the e^+, e^-, or both inside the EMC detection volume.

Event type	Cross section (nb)	Production Rate (Hz)	Level 1 Trigger Rate (Hz)
$B\bar{B}$	1.1	3.2	3.2
$u\overline{u}$ +$d\overline{d}$ +$c\overline{c}$ +$s\overline{s}$	3.4	10.2	10.1
e^+e^-	~53	159	156
$\mu^+\mu^-$	1.2	3.5	3.1
$\tau^+\tau^-$	0.9	2.8	2.4

3.3 Data Acquisition System

The data acquisition system (DAQ) transports data from the front end electronics (FEE) through the trigger to the OEP. The schematic drawing of the DAQ system is show in 3.10. The FEE perform signal processing, digitization, and data transfer, which include buffering and transfer latencies. The FEE are installed on the detector to increase reliability of signal and avoid noise in the long cables which transfer the signal to the VME crates. Each sub-detector has dedicated Level 1 trigger processors which pass output to the FCTS at a rate of 30 MHz. Once a Level 1 accept is issued from the FCTS, the data from the Level 1 latency buffer is read out using the ROMS. The VME crates house the ROMS for the sub-detectors and are divided accordingly.

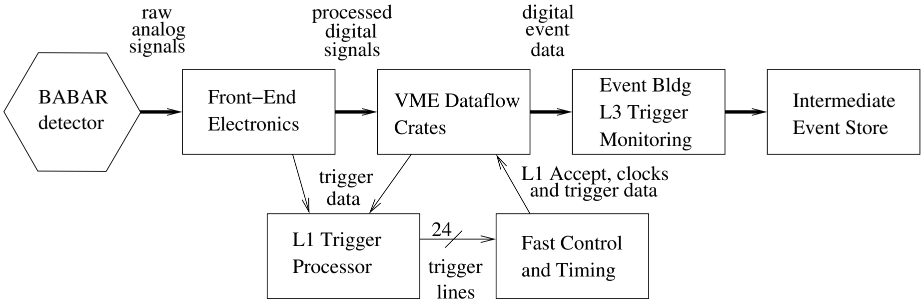

Figure 3.10: Schematic drawing of dataflow layout.

ODF is responsible for the acquisitions and building of events from the FEEs with great efficiency and as little deadtime as possible. The *BABAR* ODF is more than 98% efficient during normal running. ODF builds events by harvesting data from each crate into another set of ROMS which are connected to the online nodes (farm) via an Ethernet network. After passing through the Level 3 trigger which is described above, the data is passed onto the online prompt reconstruction (OPR). OPR is responsible for an more extensive monitoring system and selection of physics events. Rolling calibrations which involve applying constants calculated from one run to a future run are also done on OPR. These constants and the events reconstructed at OPR are stored in the conditions database and the object oriented event store. This data is accessible to users for running analysis programs.

3.3.1 Online Detector Control and Run Control

During data taking there are personnel on shift monitoring the detector and the plots provided by the OEP to insure all elements of the detector and the DAQ system are working properly. The Online Detector Control (ODC) system controls and monitors the detector through the use of EPICS, Experimental Physics and Industrial Control System. Through the EPICS controls one can monitor, diagnose, and control the detector. EPICS also provides alarms in case of problems from the detector and has an interface to PEP-II and the magnet controls. The online run control (ORC) allows for operation of the DAQ system. One can take out certain VME crates during running, configure the ROMS, start up OEP, and begin, pause, or end runs. Calibrations of the subsystems can also be done using ORC. All this functionality is stored into one graphical interface at IR2.

3.4 Candidate Reconstruction

The particles which are identified by the detector are pions, electrons, muons, kaons, protons, photons, and K_L^0 mesons. All other particles are made of some combination of those on this list. Charged particles have an associated track which can be identified by the SVT and DCH. Neutral particles will only leave a signature in the EMC and IFR. Photons are detected by the EMC and muons and K_L^0 mesons by the IFR. The difference between a kaon and pion is determined by the SVT and DCH $\mathrm{d}E/\mathrm{d}x$ for lower energies and for higher energies by the DIRC. The next two sections describe track reconstruction and particle identification in the detector.

3.4.1 Track Reconstruction

The reconstruction of charged tracks relies on information from the SVT and DCH. There are five parameters describing the helical shape of the track in the detector. These parameters are d_0, ϕ_0,

ω, z_0, and $\tan\lambda$; see fig 3.11 for a graphical representation of the variables. d_0 and z_0 are measured at the point of closest approach to the z axis and are defined as the distance in $x - y$ to this point and the distance in z to this point respectively. ϕ_0 and λ are the azimuth angle and dip angle with respect to $x - y$ respectively. And finally ω is the curvature and is defined as $1/p_T$. ω and d_0 carry signs which are related to the sign of the particle.

The track finding algorithm starts with information from the trigger system. The Level 1 trigger recognizes tracks as four contiguous track segments (*hits*) in two dimensions. Then the Level 3 trigger software goes one step further with DCH hit pattern recognition which provides the first estimate of $d_0, \phi_0,$ and the event start time t_0. After passing several other offline track finder algorithms in the DCH, the tracks are fit with a Kalman-Filter fitter which takes into account material interactions, energy loss, and non-uniformity of the magnetic field in the detector. One of the DCH algorithms is designed to find long-lived particles, such as the K^0_S meson, which may not leave hits in the SVT.

The fitted DCH track is then extrapolated into the SVT and SVT track segments are added. The SVT segment with the smallest residuals and largest number of SVT hits is used to connect to the DCH track. Again a Kalman fit is performed to the whole SVT-DCH track to obtain a more refined fit to the track. Any remaining SVT hits are used in two separate algorithms to search for tracks. One of the algorithms searches for spatially dispersed hits in z_0 and d_0 and the other for hits which are confined to a small area in z. Finally the algorithms try to match SVT and DCH tracks which could have discontinuities due to scattering.

Track reconstruction resolution is determined with cosmic ray events by comparing fits to cosmic track halves in the upper and lower region of the detector. The resolutions for particles with energy $> 3\,\mathrm{GeV}$ are $\sigma_{d_0} = 23\mu$m, $\sigma_{\phi_0} = 0.43$ mrad, $\sigma_{z_0} = 29\mu$m, and $\sigma_{\tan_\lambda} = 0.53$ x10^{-3}. The p_T resolution as a function of p_T is also shown in fig 3.12.

3.4.2 Particle Identification (PID)

As noted in section 3.4 there are a few long-lived particles which leave signals in detector systems. In general, among these long-lived objects, we need to differentiate between kaons and pions, differentiate energy deposits in the EMC from photons or charged tracks, and identify muons and K^0_L mesons from the IFR. Particle identification is a key ingredient for determining the flavor of the B mesons as described in 5.1.

For charged particles with momenta below about 0.7 GeV$/c$, the the SVT and DCH $\mathrm{d}E/\mathrm{d}x$ is used for PID. The 80% truncated mean $\mathrm{d}E/\mathrm{d}x$ in the DCH is used to compute likelihoods for pions,

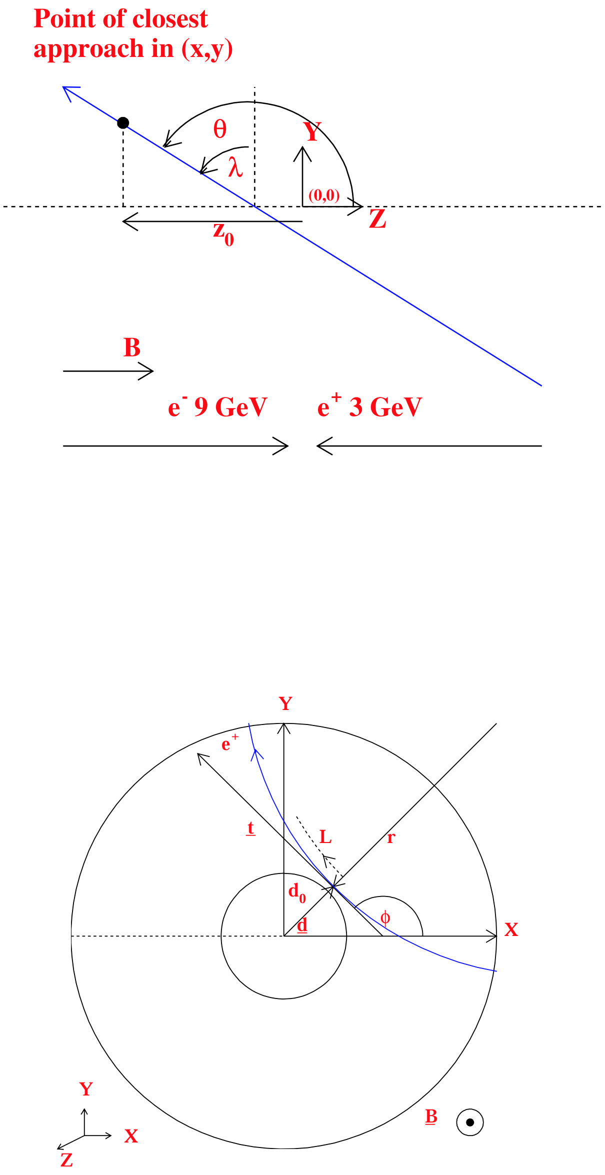

Figure 3.11: Track parameters shown in y-z coordinates (top) and x-y coordinates (bottom).

kaons, and protons assuming a Gaussian error around the nominal Bethe-Block expectation for the known momentum. The distribution of $\mathrm{d}E/\mathrm{d}x$ in the DCH as a function of momentum is shown

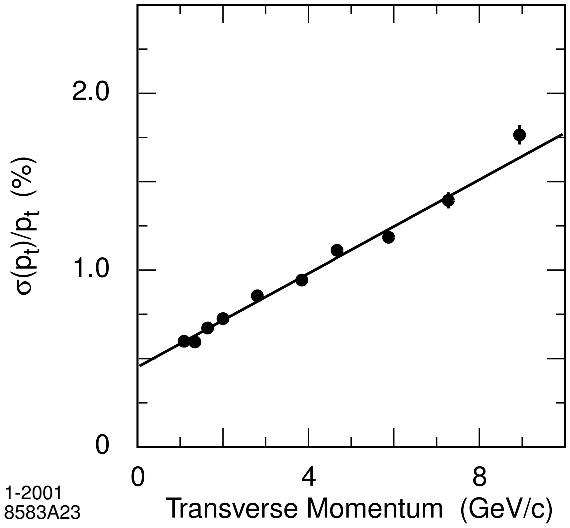

Figure 3.12: Transverse momentum resolution as a function of p_T measured with cosmic rays.

in fig. 3.13. In the SVT a 60% truncated mean $\mathrm{d}E/\mathrm{d}x$ is used and described by an asymmetric Gaussian distribution. An asymmetric Gaussian is a Gaussian with a different width left and right of the mean. The SVT achieves a 2σ separation between kaons and pions up to momentum of 500 MeV/c.

Cherenkov radiation is emitted whenever charged particles pass through matter with a velocity exceeding the velocity of light in the medium. The charged particles polarize the molecules, which then turn back rapidly to their ground state, emitting prompt radiation. The emitted light forms a coherent wavefront if $v > v_t$ where v_t is the threshold velocity defined as $1/n = v_t/c$ where $n = 1.473$ is the refraction index of silica. Cherenkov light is emitted under a constant Cherenkov angle with respect to the particle trajectory.

The Cherenkov angle, θ_c, is used to determine the particle species by using the DIRC's fused silica to internally reflect the Cherenkov light to the PMT where they are detected. The DIRC provides a separation of 4σ or greater for particles from the Cherenkov threshold velocity, about 700 MeV/c, up to 4.2 GeV/c. A likelihood is obtained from the product of expected number of Cherenkov photons, N_γ, and the difference between the average Cherenkov angle θ_c and the expected angle θ_c^0 for a given particle hypothesis. The curves shown in fig 3.14 are governed by the equation, $\cos\theta_c = 1/n\beta$. The ratio of the likelihoods for each particle hypothesis is used to determine the particle species.

Energy is deposited in the EMC crystals in the form of electromagnetic showers which cause

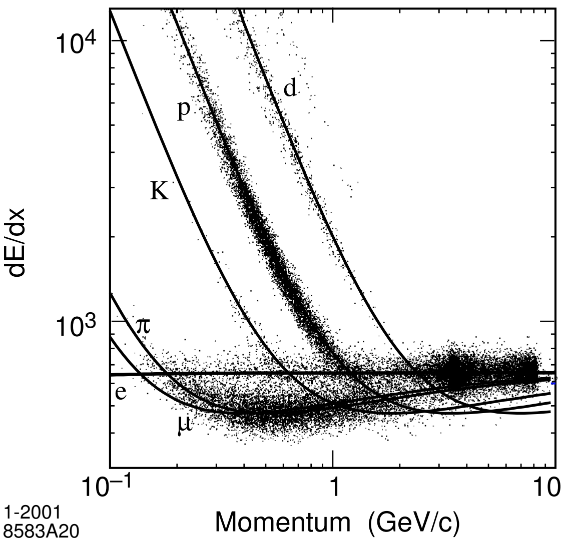

Figure 3.13: DCH $\mathrm{d}E/\mathrm{d}x$ as a function of track momenta. The solid curves are the Bethe-Bloch expectations for different long-lived particle species.

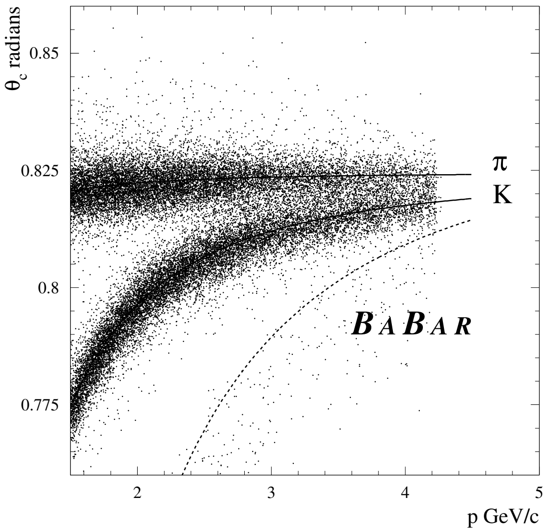

Figure 3.14: The measured Cherenkov opening angle θ_c for kaons and pions versus momentum.

energy deposition in *clusters* of many adjacent crystals. Photons from high momentum π^0 and η^0 decays can produce two energy maxima (bumps) within a cluster due to the small opening angle. The EMC reconstruction algorithm starts with crystals with an energy deposit $> 10\,\mathrm{MeV}$ and adds energies from adjacent crystals until a bump is built. A bump is associated with a charged track if the projection from the bump onto the inner face of the EMC is consistent with a extrapolated track trajectory. Otherwise the bump is associated with a neutral particle with a trajectory originating at the interaction point.

The photon energy scale is calibrated with a radioactive source at low energies, with e^+e^- Bhabha scattering events at high energies, and with decays of π^0 and η mesons at energies below 2 GeV (fig. 3.15). The ratio of energy E deposited in the EMC to the track momentum p, E/p, is equal to one for electrons in an ideal calorimeter. The E/p distribution for electrons is shown in fig. 3.16. The distribution peaks at E/p slightly less than unity due to shower leakage and other resolution effects.

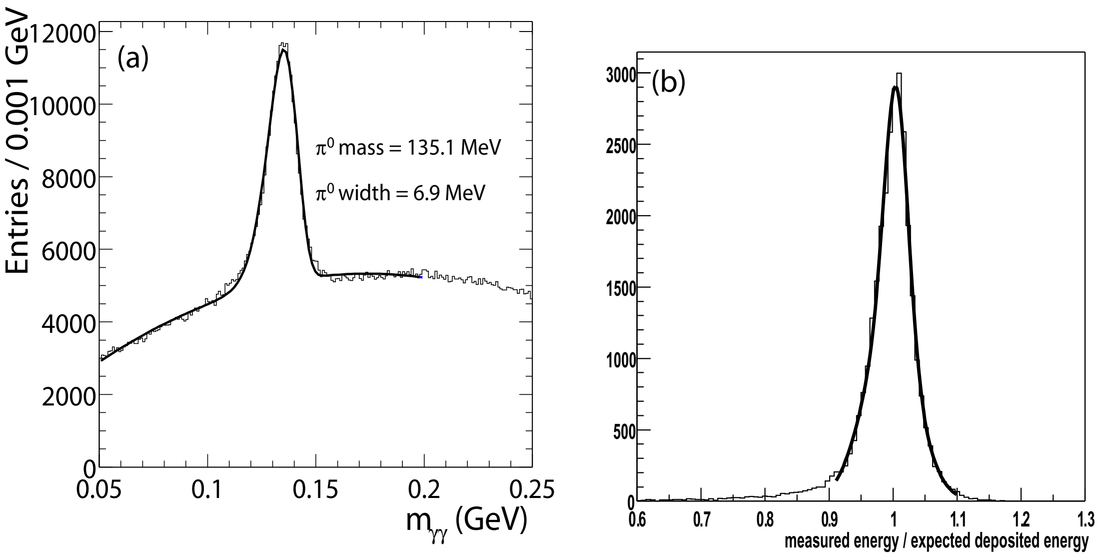

Figure 3.15: (a) π^0 mass distribution constructed from two photon candidates in hadronic events (histogram) overlaid with a fit (curve). (b) Ratio of measured to expected energy for electrons in Bhabha events (histogram) overlaid with a fit (curve).

Muons are identified by comparing the expected interaction length, λ_{exp} and the measured λ. Other variables such as the average multiplicity of hit strips per layer and it standard deviation, the χ^2 of the track, and the continuity of the tracks T_c, help reject contamination from hadronic showers. Hadrons can interact in the material and therefore lead to a broader distribution of hits, hence a larger χ^2. Muons on the other hand will match the track extrapolation into the IFR reasonably well.

The muon efficiency for particles with momentum $> 1.5\,\text{GeV}$ is about 60% with a pion fake rate of $< 2.5\%$. The muon efficiency at *BABAR* has been degrading at a rate of 1% per month. This decrease is due to the contamination of linseed oil used to coat the RPC chambers. The contam-

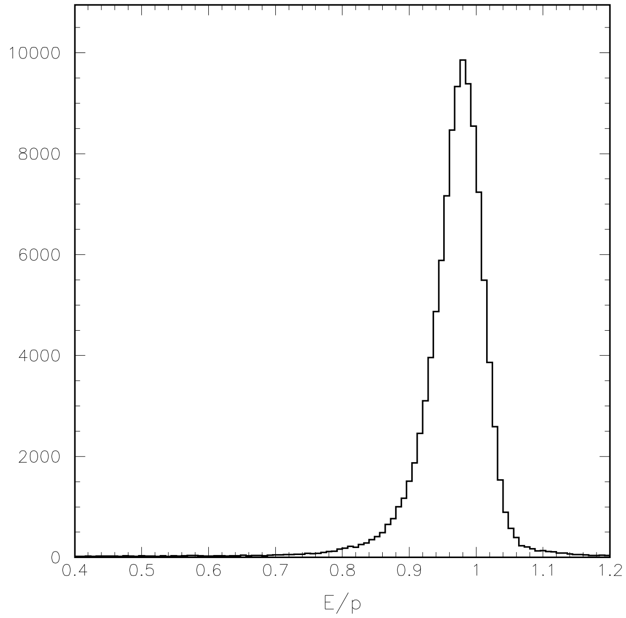

Figure 3.16: E/p of energy deposited in EMC for electrons from the process $\gamma\gamma \rightarrow eeee$

ination decreases the resistivity of the oil which has a direct consequence on the efficiency of the chambers.

Chapter 4

Event Reconstruction and Fitting Technique

In this chapter we will discuss and define the variables needed to select the events which will be used in the time-dependent *CP* analysis. Chapter 5 is reserved for discussion of the time components of the decay while this chapter focuses on the reconstruction and selection of events. At the end of the chapter we will discuss the method for extracting information from the maximum likelihood fit and define Toy MC samples.

Once the data is processed at OPR as discussed in sec. 3.3, it is stored in the event store database for use in analysis. A series of very loose selection requirements similar to analysis code only less specialized are used in OPR to separate out events of interest to certain groups. These lists are called *skims* and are stored in the database and labeled for the specific mode of reconstruction. This analysis uses the BKsKsKs3body skim which selects only 0.01% of the total events. Having the skims makes it much faster and requires fewer computing resources to run more complicated analysis code over the small sample of interest.

From the skims one can run analysis software which takes the list of K_S^0 candidates in the events and applies combinatorics and vertexing code with some loose kinematic selections. From here a set of analysis ntuples are made which can be used for modifying and fine tuning the final selection requirements for the analysis. For this analysis, the same set of signal-to-background optimized requirements are made as for the branching fraction measurement [22].

Once the final selection requirements are made another set of smaller ntuples are made with corresponding datasets and ascii files for use in the maximum likelihood fit to extract the *CP* asymmetries. The maximum likelihood fit is done in a fitting package which interfaces to RooFit, a fitting package used in high energy physics experiments [23]. From the small set of ntuples one can use the data sidebands (see sec. 4.2.2) to parametrize the backgrounds events. The signal MC events are used for parameterizing the signal events.

A fit with no Δt information is made to determine the approximate yields expected from the sample for the purpose of generating Toy MC events as described in sec. 4.5. Once tests are done with the Toy MC events to show the fit is unbiased one can perform a *blind* fit to compare the uncertainties on the asymmetries with the Toy MC expectations. The analysis is done *blind* meaning that the actual value of the asymmetries are hidden in order to avoid any bias from the experimenter. Once all validations are performed and the fit is determined to be unbiased, we can *unblind* the result.

We've only touched briefly on the time-dependent part of the analysis in this overview. We will discuss vertexing and determining Δt in greater detail in chapter 5.

4.1 Event Samples

The samples used for this analysis are on and off resonant data and signal MC. The signal MC are divided into SP5 and SP6 which correspond to conditions in runs 1-3 and run 4 respectively.

- Data: Run 1-4 on-resonance data corresponding to 205 fb^{-1}.
- Data: Run 1-4 off-resonance data corresponding to 16 fb^{-1}.
- MC: SP5 $B^0 \to K^0_S K^0_S K^0_S$ 120K $K^0_S \to \pi^+\pi^-$ and $\pi^0\ \pi^0$
- MC: SP6 $B^0 \to K^0_S K^0_S K^0_S$ 200K $K^0_S \to \pi^+\pi^-$ only
- MC: $B^0\overline{B}^0$ 269,590K $\approx 513\,\mathrm{fb}^{-1}$
- MC: B^+B^- 280,030K $\approx 533\,\mathrm{fb}^{-1}$

4.2 Event Selection

There are several physics events which occur at the B factory. Some of these events are background events which need to be removed. Other event types are used for calibrations and luminosity studies. The $\Upsilon(4S)$ decays are of course of interest for our analysis and therefore need to be selected from the whole set of physics events. It is therefore useful to distinguish the different set of events which can be used for various studies. Table 4.2 lists the various event types.

Physics events can be distinguished into different types through the use of two discriminating variables: the visible energy $\mathcal{W}$ and the event topology R_2 which will be discussed in this section.

Events with $\Upsilon(4S) \rightarrow B\overline{B}$ decays will have a large number of hadrons and an isotropic topology since the left over energy from the decay is small. Continuum physics events will have distinguishing traits like having jet-like topology from the hadronization of quarks produced back-to-back. Other decays, like $e^+e^- \rightarrow \gamma\gamma$ will have large missing energy and a small number of tracks. So in general by monitoring the visible energy, the event topology, and the track multiplicity we are able to distinguish between different physics events. Table 4.2 shows the characteristics of different physics results.

Table 4.1: Main characteristics of the physics processes at the $\Upsilon(4S)$ energy, in the center-of-mass frame.

Event type	Topology	Visible Energy	Number of Tracks
$e^+e^- \rightarrow e^+e^-$	Back-to-Back	Deposit in EMC	2 high momentum
$e^+e^- \rightarrow \mu^+\mu^-$	Back-to-Back	Visible	2 high momentum
$e^+e^- \rightarrow \tau^+\tau^-$	Back-to-Back	large missing energy from neutrinos from semileptonic decays	2 leptons
$e^+e^- \rightarrow \gamma\gamma$		large missing energy	small number of tracks
$e^+e^- \rightarrow q\bar{q}$ with $q = u, d, s, c$	jet-like from hadronization of quarks produced back-to-back	mean of 6 GeV	large
$e^+e^- \rightarrow \Upsilon(4S) \rightarrow B\bar{B}$	Isoptropic	mean of 6 GeV	large

The visible energy $\mathcal{W}$ is defined as the sum over all charged and neutral tracks in the tracking fiducial area,

$$\mathcal{W} = \sum_{i}^{charged} \sqrt{m_\pi^2 + p_i^2} + \sum_{j}^{neutral} E_j. \tag{4.1}$$

The distribution of the number of charged tracks and $\mathcal{W}$ are shown in figures 4.1 and 4.2 respectively for MC events. We remove QED events by selecting events with at least three charged tracks and a total visible energy greater than $4.5\,\mathrm{GeV}$.

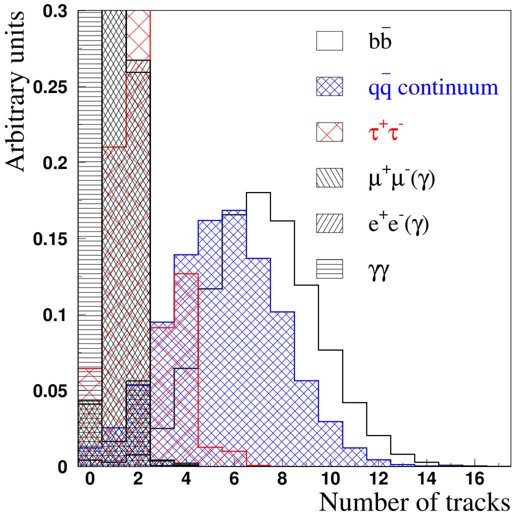

Figure 4.1: MC distribution of the number of charged tracks in the fiducial area in the main physics processes at the $\Upsilon(4S)$ energy. The distributions are normalized to the same area, rather then the relative rate..

To further discriminate from continuum $u\overline{u}$, $d\overline{d}$, $s\overline{s}$, and $c\overline{c}$ events we use a variable R_2 that is sensitive to the overall event topology. R_2 is defined as the ratio of the second to zeroth order Fox-Wolfram moments H_l

$$H_l = \sum_{i,j} \frac{|\mathbf{p_i}||\mathbf{p_j}|}{E_T^2} P_l(cos\theta_{ij}), \tag{4.2}$$

where P_l are the Legendre polynomials, $\mathbf{p_i}$ are the particle momenta, $\theta_{i,j}$ is the angle between the particles i and j, and E_T is the total energy in the event. The distribution of $R_2 \equiv H_2/H_0$ for different physics events is shown in fig 4.3.

4.2.1 Reconstruction of $K_S^0 \to \pi^+\pi^-$

K_S^0 candidates are reconstructed in the decay mode $\pi^+\pi^-$ which has a branching fraction of 68.95% [13]. A pair of charged track candidates are required to originate from the same point in space (vertex fit). Candidates with an invariant mass of $|M_{K_S^0} - M_{K_S^0}^{PDG}| < 12\,\mathrm{MeV}$ are selected, where $M_{K_S^0}^{PDG} = 497.6\,\mathrm{MeV}$ [13]. The invariant mass m($\pi^+\,\pi^-$) of the selected candidates is shown in fig. 4.4. Other selection requirements made on the K_S^0 candidate are:

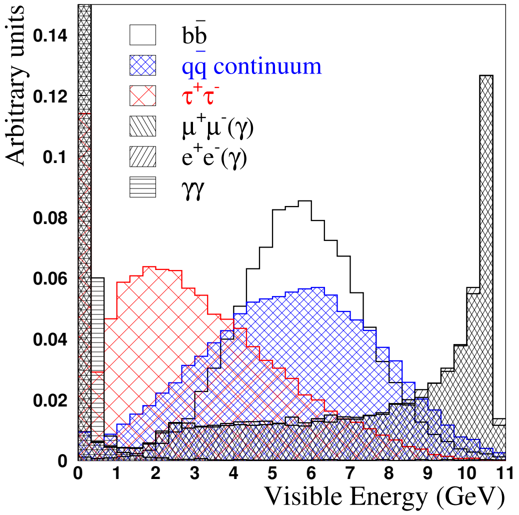

Figure 4.2: MC distribution of the visible energy $\mathcal{W}$ in the main physics processes at the $\Upsilon(4S)$ energy. The distributions are normalized to the same area.

- Vertex probability, $P(\chi^2) > 10^{-6}$. The distribution of the vertex probability is shown in fig. 4.5.
- K_S^0 flight length in the transverse direction, $0.2 < R_D < 40\,\mathrm{cm}$. The distribution of the flight length is shown in fig. 4.6.
- Angle α, $\alpha < 200 mrad$. α is defined as the angle between the flight direction and the momentum vector of the K_S^0 candidate. The distribution of the angle α is shown in fig. 4.6.

4.2.2 B Meson Reconstruction

Once the K_S^0 candidates are selected we choose three from the same event which satisfy several kinematic requirements. In addition we use other variables to discriminate between signal and background events which can look very similar to the signal in all other respects. The next two sections will describe the kinematic and continuum suppression variables which are used on the *BABAR* experiment and in this analysis.

Kinematic Variables

The *BABAR* experiment uses two nearly orthogonal kinematic variables to select B meson candidates [24]:

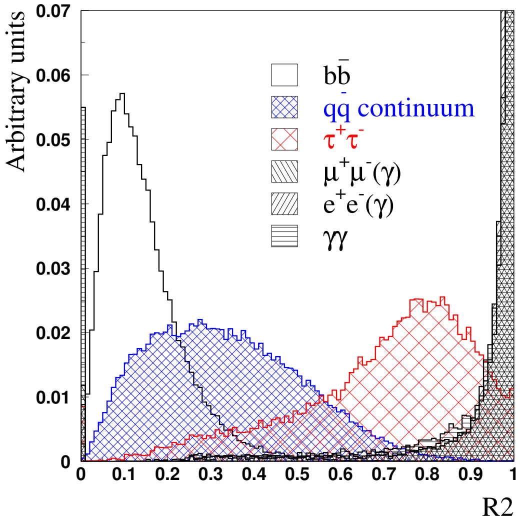

Figure 4.3: MC distribution of R_2 for the main physics processes at the $\Upsilon(4S)$ energy. The distributions are normalized to the same area.

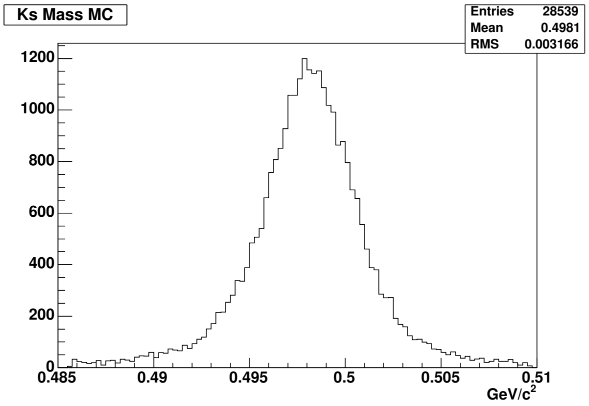

Figure 4.4: Distribution of K_S^0 mass with $|M_{K_S^0} - M_{K_S^0}^{PDG}| < 12\,\mathrm{MeV}/c^2$ requirement.

- The energy difference $\Delta E = E^* - E_b^*$,
- The beam-energy-substituted mass $m_{\mathrm{ES}} = \sqrt{E_b^{*2} - p^{*2}}$.

E^* and E_b^* are the energy of the B candidate and the beam energy in the $\Upsilon(4S)$ rest frame respectively. p^* is the measured momentum of the B candidate in the $\Upsilon(4S)$ center-of-mass frame. In the rest frame E_b^* is half the $\Upsilon(4S)$ energy and is the best estimate of the true energy of the B meson. Signal candidates will peak at $\Delta E = 0$ and $m_{\mathrm{ES}} = 5.27\,\mathrm{GeV}$. The uncertainty of ΔE is dependent on the decay and is about 10 MeV for the $B^0 \to K_S^0 K_S^0 K_S^0$ decay. On the other hand the RMS

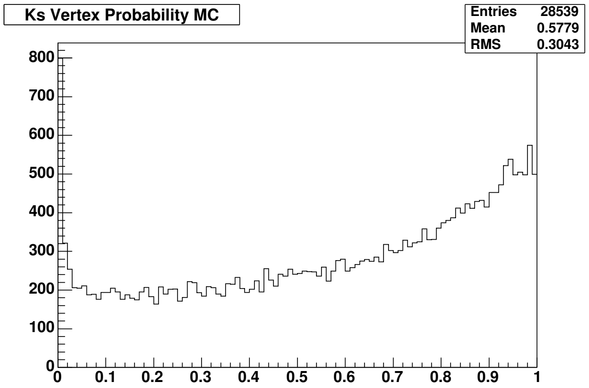

Figure 4.5: Distribution of K_S^0 vertex probability.

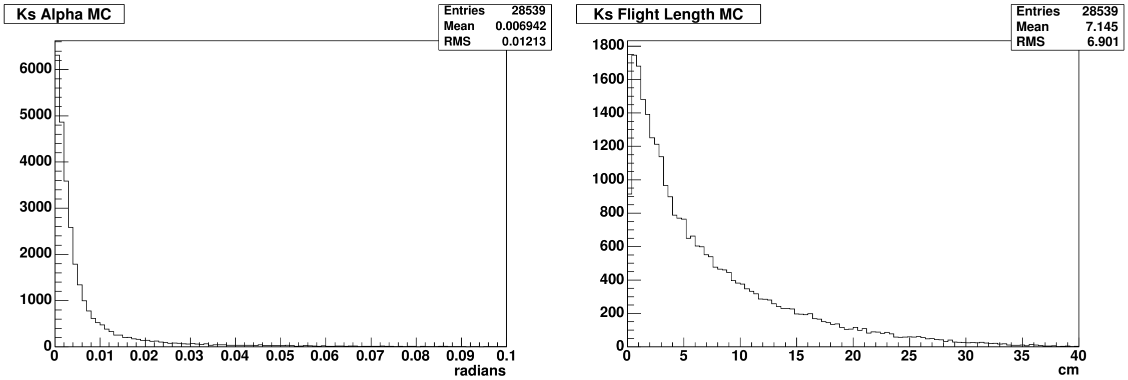

Figure 4.6: Distribution of K_S^0 angle α (left) and K_S^0 flight length R_D (right).

spread of m_{ES} is given by

$$\sigma^2(m_{\mathrm{ES}}) \approx \sigma_B^2 + (\frac{p}{M_B})^2\sigma_p^2, \tag{4.3}$$

where σ_p is the uncertainty of the momentum of the B candidate and σ_B is the beam energy spread. Since $\frac{p}{M_B} \approx \frac{325\,\mathrm{MeV}/c}{5279\,\mathrm{MeV}/c^2} \approx 0.06c$, the uncertainty of m_{ES} is dominated by the beam energy spread which is $\approx 2.6\,\mathrm{MeV}$ [24].

Signal event will peak near the B mass, $5.27\,\mathrm{GeV}/c^2$, and also peak around $\Delta E = 0$. Combinatorial background, which is usually comprised of $q\overline{q}$ events, can have events around $\Delta E = 0$ and in m_{ES} be smoothly distributed and taper off at the beam energy, 5.291 GeV. Fig. 4.7 shows a simple depiction of signal and background components in the m_{ES} distribution. Peaking background are defined as B decays which resemble signal, i.e. peak in both ΔE =0 and m_{ES} =5.27 GeV/c^2, but are events which we either discard or subtract from the total number of signal events. In this experiment the peaking background, or B background, component is negligible. Distributions of

ΔE and $m_{\rm ES}$ for signal MC and background data are shown in figs. 4.8 and 4.9 respectively.

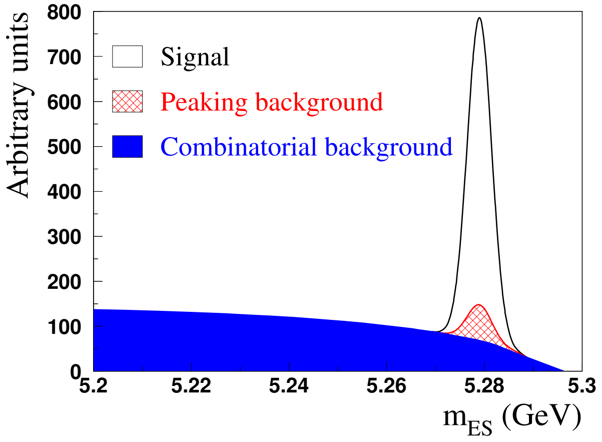

Figure 4.7: Simple depiction of $m_{\rm ES}$ distribution showing various signal and background components.

To parametrize the background probability distribution functions (PDF) for the maximum likelihood fit we use the distribution for events from a certain region on the two dimensional $m_{\rm ES}$-ΔE plane where we would only expect background events. The regions are defined in table 4.2.2. The $m_{\rm ES}$ sideband is used to parametrize the background ΔE distribution and the other variables in the fit, see sec. 4.4, and the ΔE sideband is used for parameterizing the background $m_{\rm ES}$ shape.

Table 4.2: Definition of signal and sideband regions in the $m_{\rm ES}$-ΔE plane.

Region	$m_{\rm ES}$ Window (GeV/c^2)	ΔE Window (Gev)
Signal	$5.27 < m_{\rm ES} < 5.291$	$\lvert\Delta E\rvert < 3\sigma_{\Delta E}$
$m_{\rm ES}$ sideband	$5.22 < m_{\rm ES} < 5.27$	$\lvert\Delta E\rvert < 120\,\rm MeV$
ΔE sideband	$5.22 < m_{\rm ES} < 5.291$	$\lvert\Delta E\rvert > 3\sigma_{\Delta E}$

Continuum Suppression Variables

The continuum suppression variables used in this analysis are $\cos\theta_T$ and a Fisher discriminant. We will define these variables in this section.

The *thrust axis*, $\vec{A}_B$, of a selected B candidate can be used to suppress continuum events by

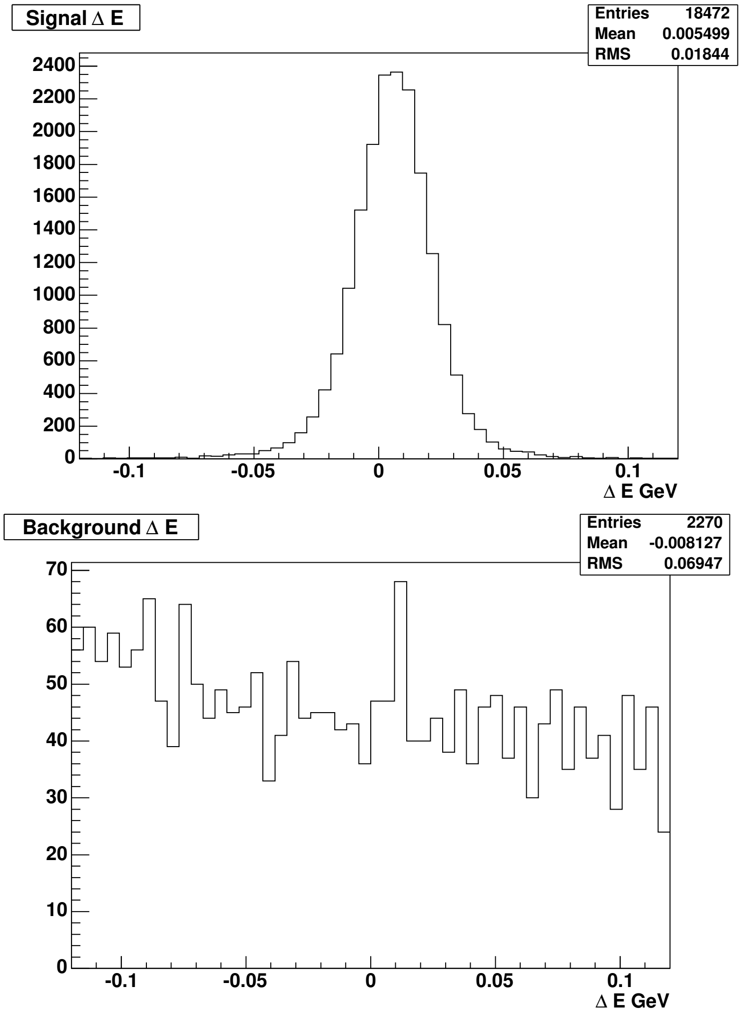

Figure 4.8: Distributions of ΔE for signal MC (top) and background from data with $m_{\mathrm{ES}} < 5.27\,\mathrm{GeV}/c^2$ (bottom).

maximizing the ratio

$$R_T = \frac{\sum_i^{1,N} |\vec{A}_B \cdot \vec{p_i}|}{\sum_i^{1,N} \sqrt{\vec{p_i^*} \cdot \vec{p_i^*}}} \tag{4.4}$$

with respect to $\vec{A}_B$. The sum is over the charged and neutral particles in the event which are not used in reconstructing the B candidate; $\vec{p_i}$ is their three-momentum vector in the $\Upsilon(4S)$ rest frame. The actual variable which is used for rejection of events is

$$\cos\theta_T = \frac{\vec{p_B} \cdot \vec{A}_B}{|\vec{p_B}||\vec{A}_B|} \tag{4.5}$$

where p_B is the B meson momentum. The distribution of $\cos\theta_T$ peaks at ± 1 for the jet-like contin-

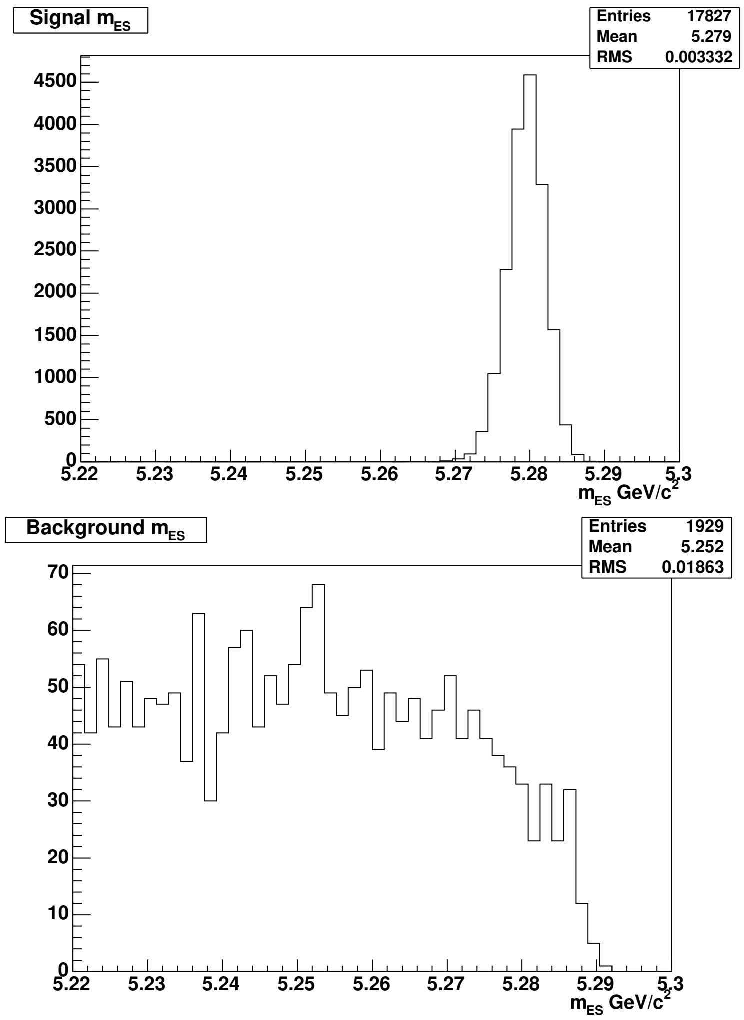

Figure 4.9: Distributions of m_{ES} for signal MC (top) and background from data with $|\Delta E| < 40\,\mathrm{MeV}$ (bottom).

uum events but is uniformly distributed in the isotropic $B\,\overline{B}$ events as see in fig 4.10. A selection requirement of $|\cos\theta_T| < 0.9$ is made to reject about 60% of continuum events in the sample.

The next continuum rejection variable is a Fisher Discriminant [25],

$$\mathcal{F} = C + \sum_j l_j L_j \tag{4.6}$$

where

$$L_i = \sum_j^{ROE} p_j |\cos\theta_j|^i \tag{4.7}$$

and C is an arbitrary constant. The sum includes all tracks and neutral particles not used in reconstructing the B candidate (rest of the event ROE). The variables θ_j is the angle between the

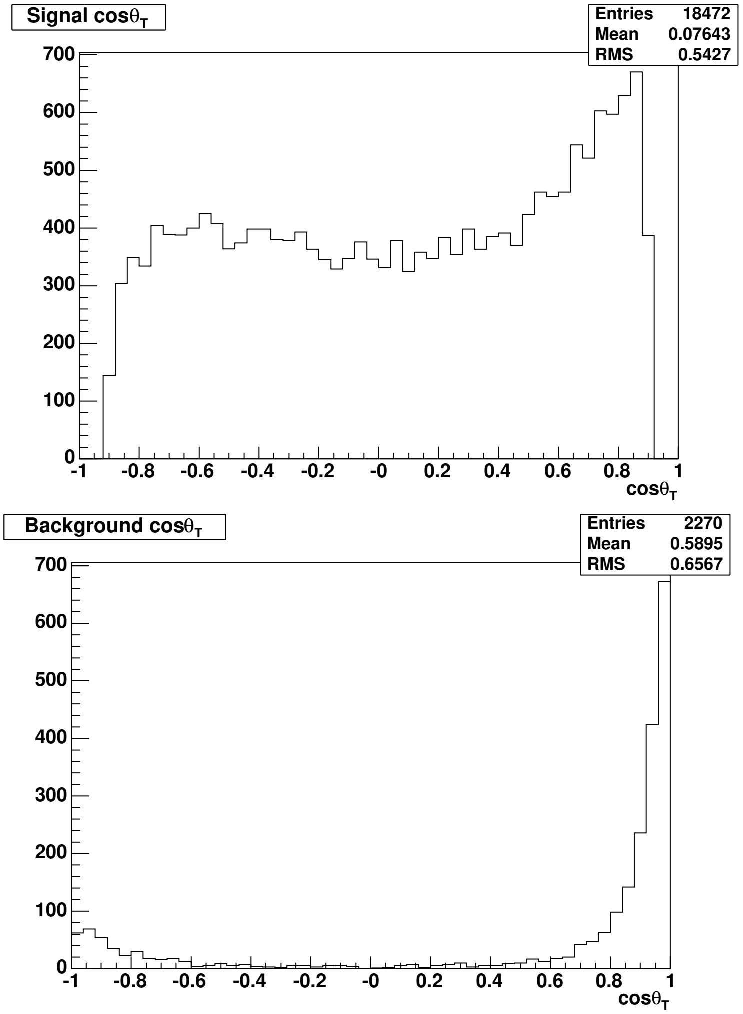

Figure 4.10: Distributions of $\cos\theta_T$ for signal MC (top) and background from data with $m_{\text{ES}} < 5.27\,\text{GeV}/c^2$ (bottom).

particle's momentum, p_j, direction and the *thrust axis*.

We use the coefficients optimized for the quasi-two body modes which should have a similar topology to our decay. The Fisher Discriminant used for this analysis is

$$\mathcal{F} = 0.5264 - 0.1882 L_0 + 0.9417 L_2. \tag{4.8}$$

The distributions of $\mathcal{F}$ for signal MC and background events are shown in fig 4.11.

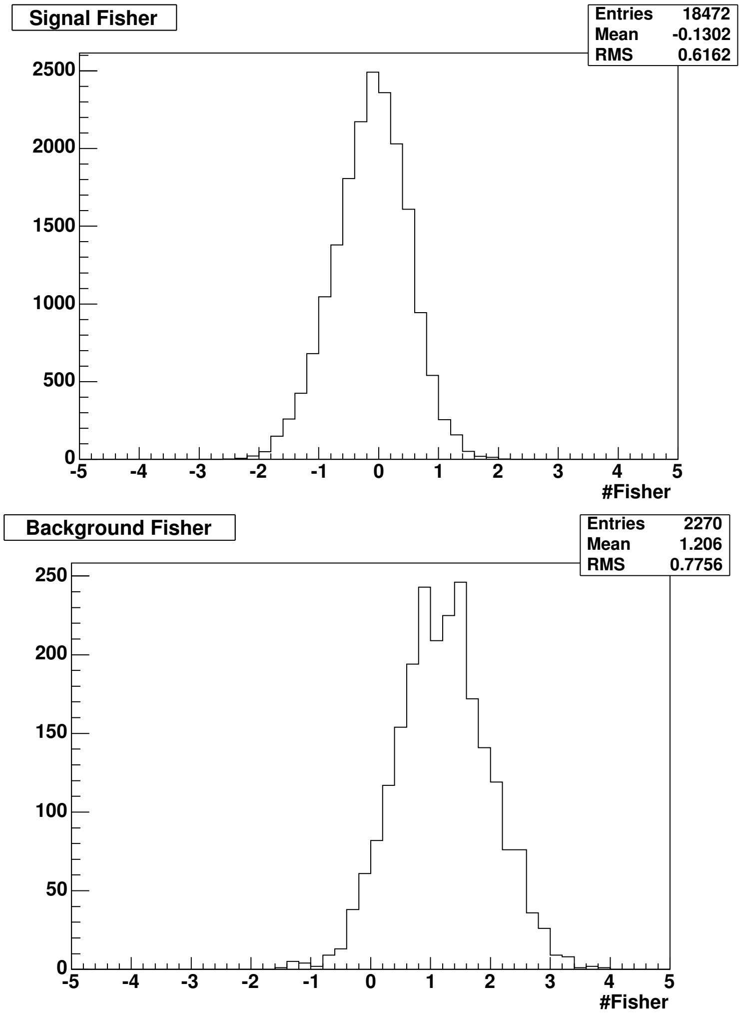

Figure 4.11: Distributions of $\mathcal{F}$ for signal MC (top) and background from data with $m_{\text{ES}} < 5.27\,\text{GeV}/c^2$ (bottom).

4.3 Selection Requirement and Efficiency

The selection requirements described in this section are used in the second pass of ntuple making before writing out datasets and ascii files for the fit. Tables 4.3 and 4.3 summarize the final selection requirements before applying vertexing algorithms and time-dependent selection requirements for data and MC respectively. The data is split into several datasets which were labeled for the purpose of efficiently processing the data when it became available and identifying the samples used for a specific analysis. The datasets used in this analysis are run1-3, Green Circle, and Black Diamond-Green Circle. The difference in efficiency for m_{ES} and ΔE between runs 1-3 and run 4 is because of a skim difference. The skim for run 4 has $K^0_S \to \pi^0\,\pi^0$ events which are not used in this analysis and are essentially removed after the $m_{\rm ES}$ and ΔE selection requirements. The expected number of signal and background events is 89 ± 10 and 439 ± 21 respectively which is the yield obtained from a maximum likelihood fit to $m_{\rm ES}$, ΔE, and $\mathcal{F}$.

The level of B background is predicted to be negligible since scaling the $B\ \overline{B}$ MC sample, 14 events, from 520 fb^{-1} to 205 fb^{-1}, we would expect 6 events. Of the 14 events in the full $B\ \overline{B}$ MC sample, 4 are charmonium final states χ_{c0} (3) and χ_{c2} (1), which are removed explicitly. There are then only 4 expected B background events in the data sample.

We choose to remove the χ_c events from our sample since they are known $cc\overline{s}$ events rather than $sq\overline{q}$ events under study here. We remove events that fall within 3σ of the fitted mean mass of the two χ_c modes. The fit to the two distributions is shown in fig 4.12. The mass cuts used are $3.3715 <$ $\mathrm{M}_{\chi_{c0}} < 3.4708\,\mathrm{GeV}/c$ and $3.5224 < \mathrm{M}_{\chi_{c2}} < 3.6016\,\mathrm{GeV}/c^2$. The branching fraction in the MC for the two modes are $2\mathrm{x}10^{-7}$ and $6\mathrm{x}10^{-7}$ respectively. These decays have not been observed and only a limit of $B^0 \rightarrow \chi_{c0}K^0 < 5.0 \times 10^{-4}$ at 90% confidence level has been measured experimentally.

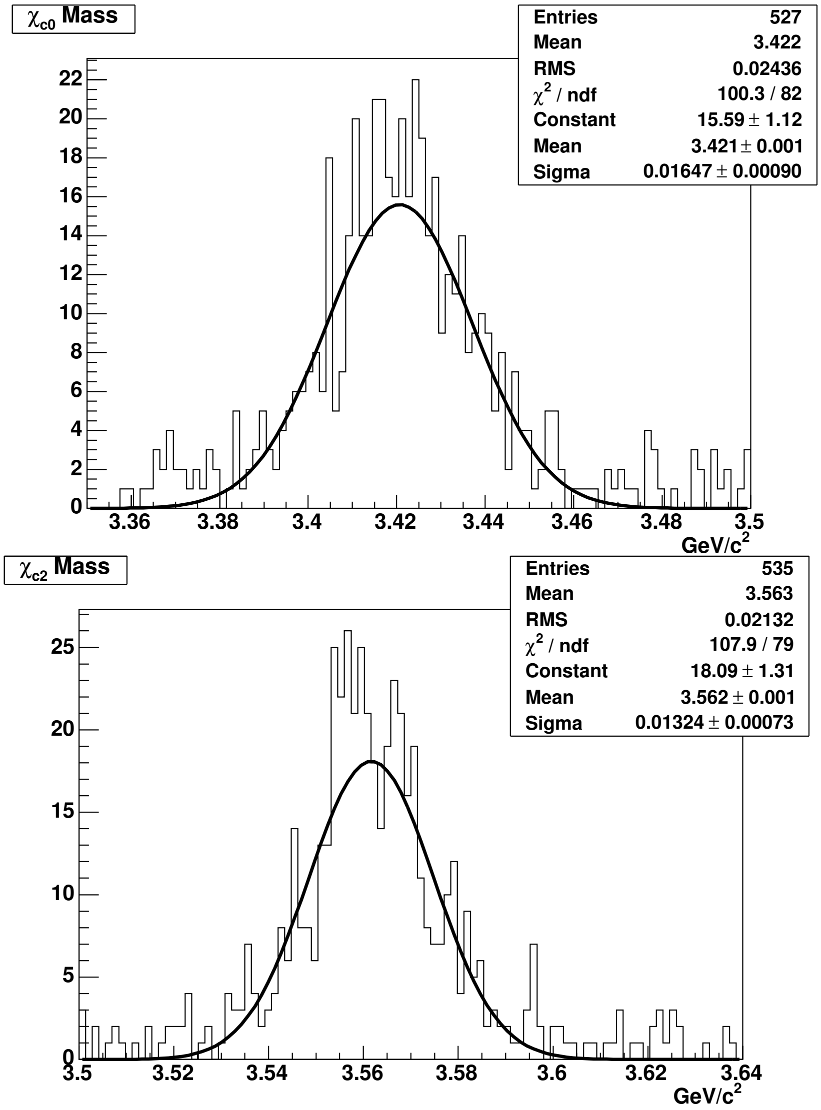

Figure 4.12: Fitted mass distribution of χ_{c0} and χ_{c2} candidates in signal MC.

Table 4.3: Selection efficiency for analysis cuts in data. First Column for each category is the relative ϵ and the second column is cumulative efficiency, ϵ.

Cut	Run1-3 Data		Run4 Data GC		Run4 Data BD-GC		Offres Run1-3		Offres Run1-4 BD	
Total Events Before cuts	399,778		281,032		204,651		40,631		21,345	
$5.22 < m_{\rm ES} < 5.3\,{\rm GeV}$	74.2	74.2	66.7	66.7	66.4	66.4	53.5	53.5	47.2	47.2
$\lvert dE\rvert < 120\,{\rm MeV}$	36.2	26.9	28.7	19.2	28.5	18.9	34.4	18.4	27.6	13.0
K_S^0 flight length $0.2 < R_D < 40$ cm	14.5	3.9	15.2	2.9	16.0	3.0	14.3	2.6	14.4	1.9
K_S^0 mass 12 MeV	30.6	1.2	29.8	0.9	29.4	0.9	31.2	0.8	29.2	0.5
K_S^0 angle cut $\alpha < 200$ mrad	32.5	0.4	31.4	0.3	30.0	0.3	27.2	0.2	29.9	0.2
$\lvert\cos\theta_T\rvert < 0.9$	40.7	0.2	38.2	0.1	41.1	0.1	37.4	0.1	25.7	0.04
K_S^0 vertex prob $P(\chi^2) > 10^{-6}$	63.3	0.1	52.9	0.06	60.9	0.07	58.8	0.05	55.6	0.02
Luminosity	$110.8\,{\rm fb}^{-1}$		$55.0\,{\rm fb}^{-1}$		$39.6\,{\rm fb}^{-1}$		$11.6\,{\rm fb}^{-1}$		$4.4\,{\rm fb}^{-1}$	
Total # of Events After all cuts	401		155		137		20		5	
# of Events/ ${\rm fb}^{-1}$ After all cuts	3.6±0.2		2.8±0.2		3.5±0.3		1.7±0.4		1.1±0.5	

Table 4.4: Selection efficiency for analysis cuts in MC. First Column for each category is the relative ϵ and the second column is cumulative efficiency, ϵ.

Cut	Signal MC SP5		Signal MC SP6		$b\bar{b}$ MC	
Total Events Before cuts	22,613		6,540		30,680	
$5.22 < m_{\rm ES} < 5.3\,{\rm GeV}$	81.1	81.1	81.5	81.5	68.3	68.3
$\|dE\| < 120\,{\rm MeV}$	84.8	68.8	84.5	68.9	22.7	15.5
K_S^0 flight length $0.2 < R_D < 40$ cm	88.0	60.5	87.9	60.6	10.4	1.6
K_S^0 mass 12 MeV	86.3	52.3	86.2	52.2	28.9	0.5
K_S^0 angle cut $\alpha <$ 200 mrad	94.2	49.2	93.5	48.8	54.9	0.3
$\|\cos\theta_T\| < 0.9$	87.6	43.1	88.2	43.0	79.5	0.2
K_S^0 vertex prob $P(\chi^2) > 10^{-6}$	92.8	40.0	92.4	39.2	56.5	0.04
Luminosity/#Generated Signal MC	120 K		35 K		$520\,{\rm fb}^{-1}$	
Total # of Events After all cuts	9053		2563		14	

4.4 Maximum Likelihood Fit

The time-dependent CP asymmetries for this analysis are extracted from a multidimensional maximum likelihood fit. In this section we will describe the theory behind a maximum likelihood fit and show the probability density functions (PDFs) used for each variable in the fit.

The likelihood for extracting N measurements $x_1, x_2, ...x_N$ given the PDF P for an observable x is defined as

$$\mathcal{L}(\alpha_j) = \prod_i^N P(x_i|\alpha_j) \tag{4.9}$$

where α_j parametrize P. Maximizing L with respect to α_j provides an unbiased, unique value. We will use this fact to apply this method of extraction to our analysis.

The likelihood that describes the events in our sample is a multidimensional version of the equation listed above. We will simultaneously fit several variable distributions, x^k=m_{ES}, ΔE, $\mathcal{F}$, Δt. If these variables are uncorrelated the probability of obtaining an event with a specific set of measurements is the product of the individual probabilities

$$P(x^k) = P(m_{\mathrm{ES}})P(\Delta E)P(\mathcal{F})P(\Delta t). \tag{4.10}$$

Since we have signal and background events in our sample we can expand the total probability to

$$P(x^k) = f_S P^S(x^k) + f_B P^B(x^k), \tag{4.11}$$

where $f_{S,B}$ is the fraction of signal, background in the sample, $f_S = N_S/(N_S + N_B)$ and $f_B = N_B/(N_S + N_B)$. Then the likelihood becomes:

$$\mathcal{L}(\alpha_j, f_{S,B}) = \prod_i^{N_T} P(\{x^k\}_i|\alpha_j, f_{S,B}). \tag{4.12}$$

As it stands the likelihood does not take into account Poisson statistics. This can be remedied by adding a Poisson term $\frac{N_T'^{N_T} e^{-N_T'}}{N_T!}$ where $N_T' = N_S + N_B$. The extended likelihood becomes:

$$\mathcal{L}(\alpha_j, f_{S,B}) = \frac{e^{-N_T'}}{N_T!} \prod_i^{N_T} N_S P^S(\{x^k\}_i|\alpha_j) + N_B P^B(\{x^k\}_i|\alpha_j). \tag{4.13}$$

From the likelihood fit we can extract the number of signal and background events and the fit parameters α_j which are the parameterizations of the background PDFs. In general the signal PDF parametrization is fixed to values from the MC and allowed to float as a systematic uncertainty.

A loose estimate of the *goodness of fit* is estimated from $\chi^2 = -2\log\mathcal{L} + C(N_T')$ where $C(N_T')$ is a constant which dependents on the number of events extracted from the fit. We minimize

χ^2 when performing the fit which is easier to compute since the $\log$ term makes the product above into a sum and the minima remains the same. We can then use Toy MC experiments, described in the next section, to determine a distribution of χ^2. These distributions can be compared with the nominal fit used for extracting the result as a consistency check.

4.5 Toy MC

In order to test how probable the results are, it is necessary to repeat the experiment many times to determine whether the results are expected given the parameterization and the number of events expected. Once the PDF of the signal and background are obtained from MC and data, we can generate events according to these distributions to determine what uncertainties we would expect from the measurement, check the goodness of fit discussed in sec. 4.4, and also test for inherent biases in the fit. The number of events expected is taken from a fit using only kinematic and background suppression variables, m_{ES}, ΔE, and $\mathcal{F}$.

In terms of the likelihood fit, the Toy MC events are indistinguishable from the data. Since one can easily generate hundreds of experiments equivalent to the data sample, the Toy MC is a good way to check the the behavior of the fit and determine the expected variance of the uncertainties on the fitted values.

Chapter 5

Ingredients of Time-Dependent CP Measurement

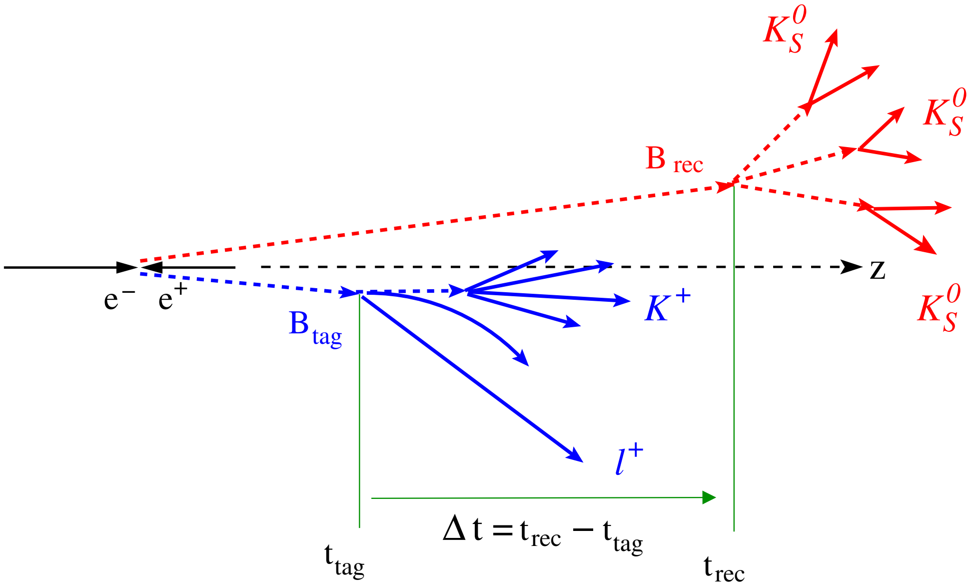

Figure 5.1: Topology of $B^0 \to K_S^0\, K_S^0\, K_S^0$ decay and Δt definition.

After the event selection we can turn to the time-dependent part of the analysis. Time-dependent

CP measurements require three basic ingredients to measure the asymmetries. These ingredient include determining the flavor of the other B meson in the $\Upsilon(4S)$ event, referred to as B_{tag}, determining the decay vertex of each B meson, and finally converting the spatial separation of the two B mesons into a proper time difference.

First we determine whether B_{tag} decayed as a B^0 or $\overline{B}^0$. This algorithm, which inclusively reconstructs the tag side B, is called B *tagging*. A large sample of MC and data called the B_{flav} sample is used to determine efficiencies and uncertainties in flavor identification. Once we know the flavor of B_{tag} as we saw in section 2.4.1, the flavor of the fully reconstructed B is determined by the time difference of the decay of the two B mesons. This works because the $B\,\overline{B}$ system is in an entangled state.

In addition to knowing the flavor of the tag side B we also need to have a decay vertex for both B mesons to determine the proper time lapse between the decays. In decays like $B^0 \to J/\psi\, K^0_S$ the J/ψ is produced promptly so its decay vertex, reconstructed from precision tracking measurements in the SVT, also determines the B decay vertex. Decays of K^0_S mesons are generally not used for determining the vertex since they they fly a significant distance from the primary B decay and therefore cannot always be reconstructed with high enough precision.

A novel method, initially used for the decay of $B^0 \to K^0_S\, \pi^0$ [26], allows a vertex to be determined for the B decay by constraining the K^0_S vertex to the beamspot in the transverse direction, which has a small uncertainty. This method is also applied to the $B^0 \to K^0_S\, K^0_S\, K^0_S$ decay since there are no primary charged tracks from which to determine a B vertex.

On the tag side, the B is reconstructed inclusively using charged tracks not used for reconstructing B_{rec}. To determine the decay vertex of the B meson a geometric fit is done constraining the particles to the beamspot. This is similar to what is done on the reconstructed side.

The boosted system, $\beta\gamma = 0.55$, makes the separation of the B vertices in z large enough that it can be measured by the detector. Once Δz is determined from the decay vertices of the B mesons, it can be translated into a time difference Δt by using the boost value and a simple conversion.

With the knowledge of Δt and flavor of B_{tag} the time spectrum can be fit. Because of detector effects and uncertainties from the tagging algorithm, the theoretical Δt spectrum has to be convolved with a resolution function which accounts for these effects. This is a method which is used by all time-dependent CP measurements like $J/\psi\ K^0_S$. However since the method of determining the B_{rec} vertex for this decay is different the resolution function must be checked to be the same as that of nominally vertexed decays.

5.1 B Flavor Determination

It's important to determine the B flavor of an event to great precision since the effective tagging quality directly effects the error on the asymmetry S. There have been several generations of tagging code at *BABAR*. Each generation aims to improve the efficiency of tagging and therefore involves changing the algorithm. The tagging algorithm used in this analysis is called *Tag04*. This tagger has an improved tagging capability of 0.5% over the previous version [27].

We mentioned earlier that the B tagging technique uses an inclusive method of reconstruction. Fully reconstructing the event would be too inefficient given the small branching fractions and the low efficiency for reconstructing all decay products. using an inclusive method gains efficiency but at the expense of having a non-zero probability for assigning the wrong flavor.

The current algorithm used at *BABAR* is a neural network trained with a large sample of MC events, from which the accuracy of the algorithm can be tested. In MC one knows the true flavor and therefore can compare it with what the algorithm determines. There are several categories used for determining the flavor. Each has its own efficiency and uncertainty. *BABAR*'s excellent particle identification capability and ability to track particles of a wide range of momentum is essential to determining the flavor of B_{tag}.

We will describe the algorithm and the relevant terms needed to do B tagging in the next three sections.

5.1.1 Definitions and Subtaggers

Several variables are used to characterize tagging and tagging performance. These are defined as follows.

- **Tagging Efficiency** ϵ: Fraction of events for which a B_{tag} is calculated.
- **Tagging Efficiency Asymmetry** $\Delta\epsilon$: Difference of tagging efficiency for B^0 and $\overline{B}^0$: $\Delta\epsilon \equiv \epsilon_{B^0} - \epsilon_{\overline{B}^0}$.
- **Mis-Tag Fractions** w: Fraction of events tagged incorrectly by the tagging algorithm.
- **Mis-Tag Fractions Asymmetry** Δw: Difference of mis-tag fraction for B^0 and $\overline{B}^0$: $\Delta w \equiv w_{B^0} - w_{\overline{B}^0}$.
- **Dilution** D : Attenuation of the *CP* asymmetry amplitude due to mis-tag, or tagging imperfection: $D \equiv (1 - 2w)$.

- **Effective Tagging Efficiency** Q: Quality factor which summarizes the performance of tagging: $Q \equiv \epsilon(1-2w)^2$.

- **Effective Tagging Efficiency Asymmetry** ΔQ: Difference of effective tagging efficiency for B^0 and $\overline{B}^0$: $\Delta Q \equiv Q_{B^0} - Q_{\overline{B}^0}$.

The error on S is effected by the value of the effective tagging efficiency, Q as seen from the relation

$$\sigma(S) = \frac{1}{\sqrt{QN_{sig}}}. \tag{5.1}$$

Tag04 contains nine subtaggers which are shown in table 5.1.1. Each of the subtaggers utilizes the correlation of the flavor of the B meson with its decay products, such as the charge of leptons, kaons, soft pions, lambdas, and angle correlations between fast and slow tracks in the final state. There are several discriminating variables used to determine the tag. This variables are applied after all the tracks corresponding to B_{rec} are removed. These variables are:

- $\mathbf{p}^*$: Center of mass momentum of particle in question.

- $\mathbf{E_{90}^{W}}$: Energy in the center-of-mass of B^0 in a 90 degree cone defined around the direction of the reconstructed virtual W boson.

- $\cos\theta_{\text{miss}}$: In the B^0 center-of-mass of $\Upsilon(4S)$ the angle between the lepton momentum and the missing momentum of the tagging B.

- $\mathbf{q}$: The charge of the track.

- $\mathbf{K}_{\text{id}}$: Kaon particle identification.

- $\mathbf{nK_S^0}$: Number of K_S^0 in event.

- $\mathcal{L}_{\mathbf{K}}$: Kaon likelihood.

- $\cos\theta_{\mathbf{i,j}}$: cosine of angle between particle i and j.

- $\cos\theta^{\mathbf{i}}_{\mathbf{Thrust}}$: cosine of the angle between particle i and the thrust axis in the center-of-mass of $\Upsilon(4S)$.

There are other variables used for the Λ decay which include:

- M_Λ: Reconstructed mass of the Λ.

- χ^2_{Vertex}: χ^2 probability of the fitted Λ decay vertex.

- $\cos\alpha$: The cosine of the angle between the flight direction and the momentum vector of the Λ .
- R_{D} : Flight length of the Λ candidate before decay.
- $p_{\Lambda,p}$: Momentum of track identified as a Λ or a p.

The discriminating variables for each subtagger are also listed in table 5.1.1.

Table 5.1: The nine subtaggers used in Tag04 tagger with the discriminating variables and training goals.

Sub-tagger Category	Discriminating Variables	Training Recognition
Electron	p^*, E_{90}^{W}, $\cos\theta_{\mathrm{miss}}$, q	B^0 versus $\overline{B}^0$
Muon	p^*, E_{90}^{W}, $\cos\theta_{\mathrm{miss}}$, q	B^0 versus $\overline{B}^0$
KinLep	p^*, E_{90}^{W}, $\cos\theta_{\mathrm{miss}}$, q	leptons from direct decays
Kaon	K_{id}^1, K_{id}^2, K_{id}^3, nK_S^0, $\sum p_T$	B^0 versus $\overline{B}^0$
Slow Pion	p^*, $\cos\theta_{Thrust}^{\pi}$	true slow pions
Max Pstar	p^*, doca_{xy}, $\cos\theta_{BCand_{maxp^*}}$	fast tracks
KPI	Kaon Tag, Slow Pion Tag, $\cos\theta_{K,\pi}$	pairs of true K and slow π
FSC	$p^*_{\mathrm{slow/fasttrack}}$, $\mathcal{L}_{Kslow/fast}$, $\cos\theta_{slow/fast}$, $\cos\theta_{Thrust}^{\mathrm{slow/fast}}$	fast-slow correlated tracks
Lambda	M_Λ, χ^2_{Vertex}, $\cos\alpha$, R_{D}, p_Λ, p_{proton}	Lambda decays

The variables contain discriminating physics information to classify the flavor of B_{tag}. There are underlying physics signatures which determine the flavor. In general we can separate them into four categories of which the nine subtaggers try to recognize variations to obtain greater Q. The four categories are leptons, kaons, soft and hard pions from D^* decays, and Λ decays. We will describe then in the next four sections.

Leptons

Fig. 5.2 shows the Feynman diagram for semileptonic decays producing primary or secondary leptons from the cascade process $b \to c \to s$. The sign of the primary leptons can distinguish the flavor of the B decay. A positive sign primary lepton indicates a B^0 decay while a negative sign

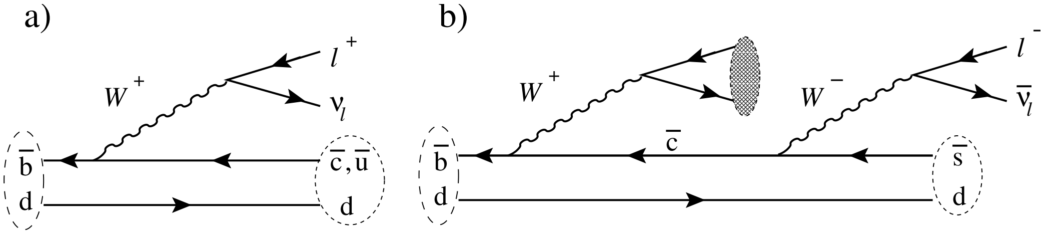

Figure 5.2: Feynman diagram for a B decay producing a primary lepton a), or secondary lepton with opposite charge from the cascade process $b \to c \to s$ b).

lepton is derived from a $\overline{B}^0$ decay. This correlation gives a very clean tagging signal with very low mistag rates. The fact that about 10% of all B mesons decay semileptonically makes for a large tagging sample. Sources of mistag can arise from secondary lepton decays and hadrons misidentified as leptons, fake leptons. A requirement that p^* for the lepton exceed $1.4\,\text{GeV}/c$ removes almost all secondary and fake leptons.

Kaons from cascade $b \to c \to s$ decays

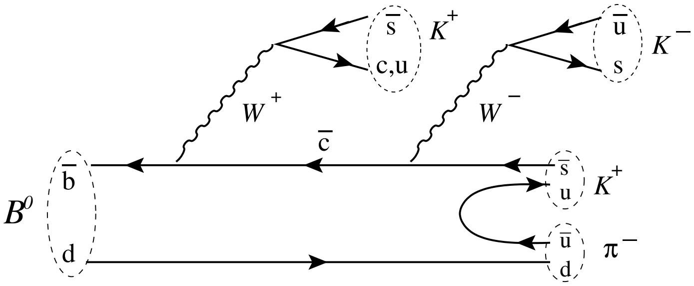

Figure 5.3: Sources of charged kaons in the decay of a B^0 meson.

Fig. 5.3 shows the Feynman diagram of B^0 decays to kaons and pions. In the cascade decay of $b \to c \to s$ a maximum of three kaons can be produced. Depending on the source of the kaon, it can either be *right-sign* or *wrong-sign*. The right-sign kaons come from hadronization of the $\overline{s}$ quark in the $\overline{b} \to \overline{c} \to \overline{s}$ reaction producing a K^+. A right-sign kaon can also be produced from the W^+ hadronization to a K^+. A wrong-sign Kaon, K^- can be produced from the W^- hadronization in the secondary decay of the intermediate charm meson state.

The W boson hadronization into kaons is Cabibbo-suppressed ($|V_{us}|^2 \sim 0.04$) and decays into pions or $D_s^+/- \equiv c\overline{s}$ are favored. The $D_s^+/-$ can be reconstructed inclusively for tagging information. The main source of mistag using kaons is from the presence of the wrong sign kaon and misidentifying pions as kaons.

Soft and hard pions from D^* decays

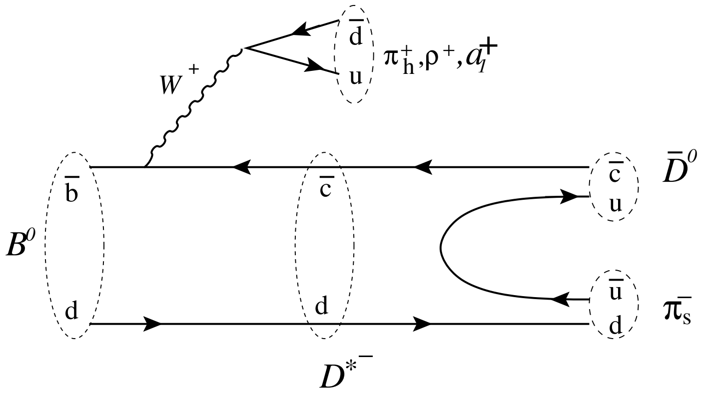

Figure 5.4: The $B^0 \to D^{*-}\pi^+, \rho^+, a_1^+$ decay. The charge of the soft pion $\pi_{\rm s}$ and that of the direct pion $\pi_{\rm h}$ are correlated with the flavor of the neutral B meson.

Fig. 5.4 shows decays of $B^0 \to D^*\ \pi^+$, ρ^+, and $a1^+$. The sign of the pion hadronizing from the W boson, π_h, has the right sign correlation with $B_{\rm tag}$ meson. This pion is called a *hard* pion since it has a large momentum.

The pion from the D^* decay, π_s, has the wrong sign correlation with $B_{\rm tag}$ and it can be distinguished from π_h by its momentum. The π_s is called the *soft* pion, because of its low momentum. This pion has a low momentum because the D^* and D masses differ by only 146 MeV, and therefore the energy available in the decay is small making the pion soft. The soft pion can be reconstructed inclusively using angular correlations between low momentum tracks and D^0 mesons.

Λ Decays

The quark content of the Λ baryon is uds. Cascade decays of $b \to c \to s$ can produce Λ mesons which need to be distinguished from kaon decays. Even though the Q of this subtagger is small, removing this subtagger would reduce the overall Q by 0.38 which is a non-negligible effect. Tag04 is the first tagger which uses this subtagger to distinguish the flavor of $B_{\rm rec}$.

5.1.2 Algorithm

Tag04 is a multivariate tagging algorithm exploiting the physics characteristics of the $B_{\rm tag}$ decay. It contains nine sub-taggers and assigns the events to six hierarchical, mutually exclusive

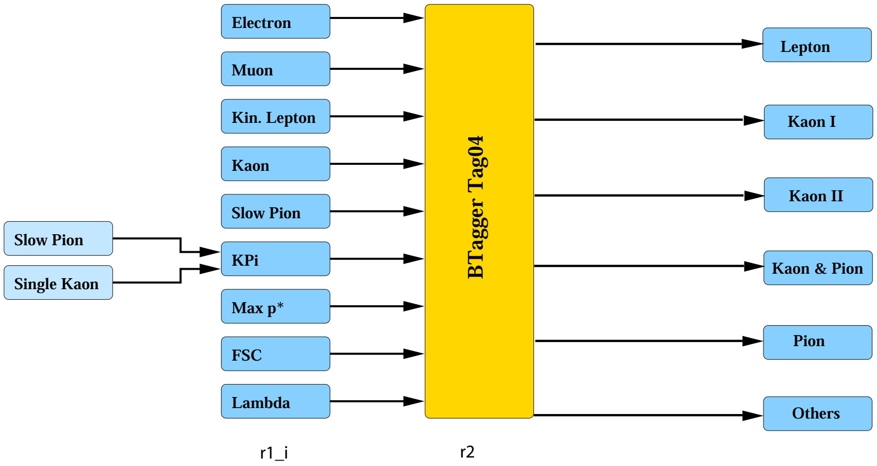

Figure 5.5: The schematic drawing of the subtaggers and tagging categories of Tag04. The outputs r_1^i and r_2 are described in the text.

categories which group events characterized by similar mis-tag fractions and underlying physics. The structure of Tag04 is shown in 5.5 and the definition of the tagging categories for Tag04 are shown in table 5.2.

Each subtagger provides a continuous output variable r_1^i which runs between +1 and -1. *ElectronTag* and *MuonTag* in the table corresponds to r_1 values from the Electron and Muon subtaggers respectively. Candidates with r_1 close to +1(-1) are more likely to be B^0 ($\overline{B}^0$). The r_2 output values, or Tag04 output, are also continuous between +1 and -1. The *btgtag* in table 5.2 corresponds to r_2 output. In the r_2 layer the outputs of the subtaggers are combined into the tagging categories.

A large sample of MC is used to train the subtaggers. The training procedure has access to the true flavor of B_{tag} and therefore can estimate p_w^i, the mistag probability for each subtagger. Each subtagger will have a different p_w^i which is governed by the physics of that selection.

There are six mutually exclusive tagging categories Lepton, Kaon I, Kaon II, Kaon & Pion, and Others with names that are meant to reflect the underlying dominant physics process for each category. Tag04 has the feature that each subtagger neural network is optimized for the specific subtagger instead of the total output from all tagging categories. The output of Tag04 is shown in fig 5.6.

5.1.3 Algorithm Performance

The performance of the Tag04 B flavor tagging algorithm in MC events is shown in table 5.3. These results are measured from a large sample of MC events with one B meson decaying to flavor

Table 5.2: Category definition used by BTagger Tag04.

Category	Cuts on input tags
Lepton	$\lvert btgtag\rvert > 0.8$ and ($\lvert ElectronTag\rvert > 0.7$ .or. $\lvert MuonTag\rvert > 0.7$)
Kaon I	$\lvert btgtag\rvert > 0.8$ and ($\lvert ElectronTag\rvert < 0.7$ .and. $\lvert MuonTag\rvert < 0.7$)
Kaon II	$\lvert btgtag\rvert > 0.6$
Kaon&Pion	$\lvert btgtag\rvert > 0.4$
Pion	$\lvert btgtag\rvert > 0.2$
Others	$\lvert btgtag\rvert > 0.1$

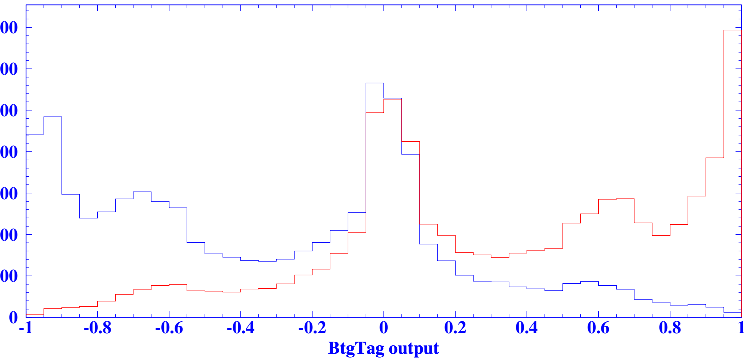

Figure 5.6: The Tag04 Neural Network output. The red and blue histograms denote true B^0 and $\overline{B}^0$ tags respectively.

eigenstates.

The Δ tagging parameters takes into account asymmetries in tagging B^0 versus $\overline{B}^0$ events. From the table above we can make some observations about the tagging categories and general tagging performance at *BABAR*.

- About 3/4 of all selected B candidates are assigned a flavor tag.
- As expected, the Lepton category has the smallest mistag rate.
- The Kaon II category has the largest efficiency.
- The best Q comes from the Lepton, Kaon I, and Kaon II categories.

- The largest mistag asymmetry comes from the Pions category. This is due to different reconstruction efficiencies of positive and negative soft pions.

The values listed above are parameters used in the maximum likelihood fit for fitting MC events. The tagging parameters are slightly different for data and we therefore have to use those parameters when fitting data events. There is a large sample of data events, flavor sample, with fully reconstructed flavor eigenstates which is used for determining the tagging parameters. The parameters can differ between data and MC because of differences in reconstruction and particle identification efficiencies. In general the efficiencies in MC are better than in data and therefore using values from MC to fit data would give unrealistic results. Additionally the branching fractions for many decays used in MC have not been measured experimentally and are generated using theoretical values. This can result in different rates of kaons and leptons between MC and data which translates into different mistag rates. The tagging parameters used in the maximum likelihood fit are slightly different than the ones shown here. The values used to fit data and MC samples can be found in table 6.1.2 in section 6.1.2.

5.1.4 Effect of Tagging Imperfections

In this section we show how tagging imperfections effect what we observe experimentally. We will start with the definitions used in chapter 2 and modify the probability distributions in the presence of mistagging and efficiencies of each tagging category.

In section 2.4.1 we introduced the time-dependent probability distributions for B meson mixing. We can now use these arguments to write the time-dependent probability distributions of B decays to tagged flavor eigenstates:

$$\Gamma_{B^0,\overline{B}^0}(\Delta t) = \Gamma_{\overline{B}^0,B^0}(\Delta t) = \frac{e^{-|\Delta t|/\tau}}{4\tau}(1+\cos(\Delta m_d \Delta t)), \tag{5.2}$$

$$\Gamma_{B^0,B^0}(\Delta t) = \Gamma_{\overline{B}^0,\overline{B}^0}(\Delta t) = \frac{e^{-|\Delta t|/\tau}}{4\tau}(1-\cos(\Delta m_d \Delta t)), \tag{5.3}$$

where $\Gamma_{A,B}$ means an event with one B tagged as B and the other reconstructed as A. If $A = B$ the event is unmixed otherwise it is mixed. Using these definitions then the probability of observing an event with a tagged flavor $T = \pm(+ = B^0 and - = \overline{B}^0)$ for one B and a reconstructed flavor $R = \pm$ for the other B in tagging category i is

$$P_i(\Delta t, T, R) = \frac{2\epsilon^r_{i(R)}}{\langle\epsilon^r_i\rangle}[\epsilon^t_{i(T)}(1-w_{i(T)})\Gamma_{R,T} + \epsilon^t_{i(-T)}(w_{i(-T)})\Gamma_{R,-T}], \tag{5.4}$$

where $\langle\epsilon_i^r\rangle \equiv \frac{\epsilon_{i+}-\epsilon_{i-}}{2}$. The first term above takes into account the correct tagged events and the second term is for the wrong tagged events. Then when normalizing such that $\sum_{T,R} P_i(\Delta t, T, R) = \epsilon_i^t$ we get the expression

$$\begin{aligned} P_i(\Delta t, T, R) &= \frac{e^{-|\Delta t|/\tau}\langle\epsilon_i^t\rangle}{4\tau}\frac{1+R\nu_i}{1-\mu_i\nu_i\xi} \times \\ &\quad [(\mu_i T D_i + 1 + T\Delta D_i) - \\ &\quad (TD_i + \mu_i(1 + T\Delta t D_i))R\cos(\Delta m_d \Delta t)] \end{aligned} \tag{5.5}$$

where $\xi \equiv \frac{1}{1+(\tau\Delta t m_d)^2}$, $\mu \equiv \frac{\Delta\epsilon^r}{(\epsilon_+^r+\epsilon_-^r)}$, and $\langle\epsilon^t\rangle \equiv (\epsilon_+^t + \epsilon_-^t)/2$.

Assuming the reconstructed B mesons are CP eigenstates we obtain the following expression with tagging imperfections taken into account,

$$\begin{aligned} P(\Delta t, T; \hat{q}_i) &= \frac{\bar{\epsilon}_i^t}{4\tau}\frac{1}{1-\mu_i\xi C_f} e^{-\frac{|\Delta t|}{\tau}} \times \\ &\quad ([\mu_i T D_i + (1 + T\frac{\Delta D_i}{2})] + [TD_i + \mu_i(1 + T\frac{\Delta D_i}{2})]A(\Delta t)), \end{aligned} \tag{5.6}$$

where $A(t) \equiv S_f \sin(\Delta m_d \Delta t) \mp C_f \cos(\Delta m_d \Delta t)$. To determine the effect of the imperfections of the tagging algorithm we set $\nu_i = \mu_i = \Delta D_i = 0$ in this equation to get

$$P_i(\Delta t, T) = \frac{\bar{\epsilon}_i^t}{4\tau} e^{-\frac{|\Delta t|}{\tau}} \left[1 + TD_i\left(S_f \sin(\Delta m_d \Delta t) \mp C_f \cos(\Delta m_d \Delta t)\right)\right]. \tag{5.7}$$

We see that the tagging mistakes only effect the amplitude of the sine and cosine term by the dilution D_i.

5.2 Measuring Decay Time, Δt

To determine the decay time difference Δt between the two B mesons in the event we need to find the decay vertex of both B mesons, B_{tag} and B_{rec}. Once the z position is determined for each decay vertex we can compute Δz which is defined as $\Delta z_{\text{rec}} - \Delta z_{\text{tag}}$. Because we know the boost of the $\Upsilon(4S)$ system we can then compute Δt from Δz by a simple conversion.

Remember that we can measure Δz because the $\Upsilon(4S)$ system is boosted in the high energy beam direction. In the $\Upsilon(4S)$ rest frame $\beta\gamma \sim 0.06$ and with the B lifetime of 1.5 ps the B mesons would be separated by only about $34\mu m$. This separation is too small to be measured experimentally however. So by boosting the system to $\beta\gamma = 0.55$ we get a separation of about $260\mu m$ in the z direction. The vertex resolution of the SVT is good enough to measure such separation quite easily.

The B pair from $\Upsilon(4S)$ is in a entangled or correlated state. This means that until one B decays there will always be one B^0 and one $\overline{B}^0$. If at time $t = t_{tag}$ $B_{\rm tag} = \overline{B}^0$ then $B_{\rm rec} = B^0$ if $B_{\rm tag}$ decayed before $B_{\rm rec}$. Since $\Delta t \equiv t_{\rm rec} - t_{\rm tag}$, $\Delta t > 0$ if $B_{\rm rec}$ decayed *after* $B_{\rm tag}$ and $\Delta t < 0$ if $B_{\rm rec}$ decayed *before* $B_{\rm tag}$. The boundary condition is set at $t_{\rm tag}$ however since at this time we know whether $B_{\rm tag}$ was a B^0 or $\overline{B}^0$. If $B_{\rm rec} = \overline{B}^0$ at $t = t_{\rm tag}$ then the time evolution of $B_{\rm rec}$ is given by

$$|\overline{B^0}_{\rm rec}(\Delta t)\rangle = (p/q)g_-(\Delta t)|B^0\rangle + g_+(\Delta t)|\overline{B^0}\rangle \tag{5.8}$$

$$g_-(t) = e^{-iMt}e^{-i\Gamma t/2} i\sin(\Delta m t/2) \tag{5.9}$$

$$g_+(t) = e^{-iMt}e^{-i\Gamma t/2}\cos(\Delta m t/2). \tag{5.10}$$

We call an event *mixed* if at $t = t_{\rm rec}$ $B_{\rm rec}$=B^0. Otherwise, if $B_{\rm rec}$=$\overline{B}^0$ the flavor stayed the same and is therefore called *unmixed*. We therefore see that we do not need to know any information about the decay time of the $\Upsilon(4S)$ which has a great experimental advantage.

5.2.1 $B_{\rm tag}$ Vertex

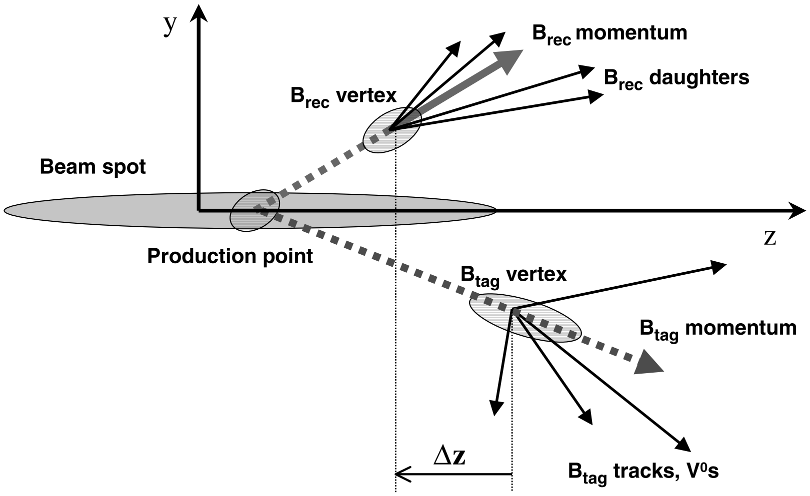

Figure 5.7: Schematic view of the $\Upsilon(4S) \to B\overline{B}$ decay in the y-z plane. Note that the scale in the y direction is substantially magnified compared to that in the z direction for illustration purposes.

The decay vertex of $B_{\rm tag}$ is reconstructed using an inclusive method which uses charged tracks in the event other than those required for the reconstruction of $B_{\rm rec}$. The algorithm removes charged tracks from long-lived particles like K_S^0 mesons and Λ baryons and replaces them by the reconstructed composite candidates in order to reduce the bias on the vertex position. Pairs of oppositely charged tracks from the decay $\gamma \to e^+e^-$ are also removed since they can have a large impact parameter. The composite particles and the remaining charged tracks are used in a geometrical fit for determining the $B_{\rm tag}$ decay vertex.

In the inclusive reconstruction the D meson decays are more difficult to remove because of the many possible final states. The D^0 and D^+ mesons have decay lengths of $c\tau$ of about $130\mu m$ and $300\mu m$ respectively. Therefore including the decay daughter in the determination of the B vertex will bias $z_{\rm tag}$. This effect is called the *charm bias* and it translates into a bias in Δz and therefore Δt. A schematic drawing of this effect is shown in fig. 5.8. The sign of the bias in Δz is always negative since $z_{\rm tag}^{meas} = z_{\rm tag}^0 + \delta z$ and since $\Delta z \equiv z_{\rm rec} - z_{\rm tag}$ $\Delta z^{\rm meas} = \Delta z^0 - \delta z$.

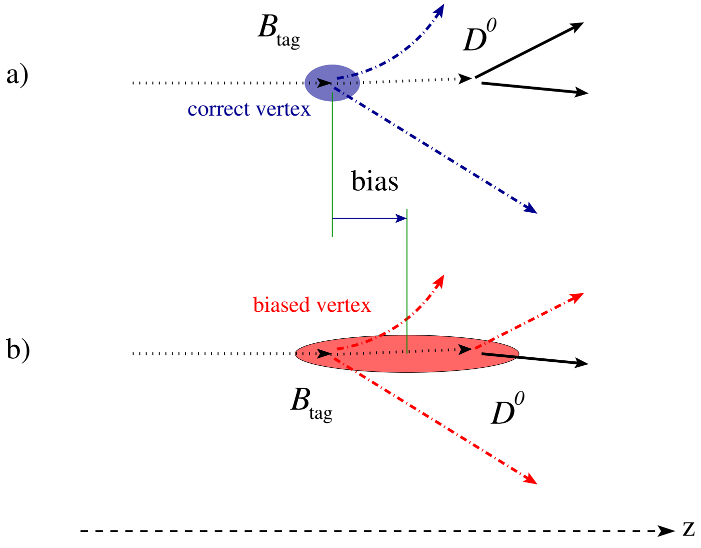

Figure 5.8: a) The correct $B_{\rm tag}$ vertex and b) the biased vertex position when the D^0 decay daughter is included. The ellipse represents the estimated uncertainty. The dash-dotted lines are the tracks used to compute the position of the vertex.

The vertex finding method uses an iterative technique which adds tracks to the fit and at each successive addition calculates a χ^2. If the track added increases the χ^2 by more than six, the track is removed from the fit. This process is continued until either all tracks satisfy the χ^2 requirement or only two tracks are left.

In general, the constraints used for determining the tag side decay vertex are the beamspot, beam energies, and the momentum and decay vertex of $B_{\rm rec}$ which are all well known quantities. For the decay of $B^0 \to K_S^0 K_S^0 K_S^0$ the $B_{\rm rec}$ vertex is not determined in the conventional way and in this case will not provide as good a constraint on B_{tag}. We will discuss this in more detail in section 5.2.2. The intersection of the momentum vector of B_{tag} with the beamspot gives the position of the $\Upsilon(4S)$ decay to B pairs. The momentum of the $\Upsilon(4S)$ is determined from the beam energies; momentum conservation then gives $\vec{p_{\text{tag}}} = \vec{p_{\Upsilon(4S)}} - \vec{p_{\text{rec}}}$. The $\Upsilon(4S)$ decay vertex and the momentum of B_{tag} are then used in a fit as kinematic and geometric constraints to determine the B_{tag} vertex. This method produces a z_{tag} resolution of about $180\mu m$.

5.2.2 B_{rec} Vertex

Since the decay of $B^0 \rightarrow K^0_S\, K^0_S\, K^0_S$ has only charged tracks from long lived K^0_S mesons, the vertex cannot be determined in the conventional way. The best constraint we have is the beamspot which is known to great precision in the transverse plane, $4\mu m$ vertically and $150\mu m$ horizontally. Therefore we can do a geometric fit constraining the B meson production vertex to the beamspot, called TreeFitter vertexing. This method gives an average uncertainty on z_{tag} of $75\mu m$ as determined from signal MC events.

This method of constraining the reconstructed B meson to the beamspot was pioneered for the $B^0 \rightarrow K^0_S\, \pi^0$ measurement [26]. The first published results were done using a vertexing technique which constrained the B *decay* vertex instead of the *production* vertex of the B to the beamspot, called beam constrained vertexing, (BC) vertexing. Fig 5.9 shows a schematic drawing of the two vertexing methods. The beamspot is shown as a green ellipse and the transverse size has been exaggerated for display purposes.

By constraining the decay vertex to the beamspot, one ignores the transverse motion of the B meson and therefore cannot accurately estimate the uncertainty on the vertex position in the transverse direction. This effect is especially noticeable in the vertical direction where the resolution is small enough to see the B motion which is about $30\mu m$. This can be seen in fig 5.10 where the pull distributions for the vertex are shown for the two vertexing methods. The pull for a variable x is defined as $x_{\text{pull}} \equiv \frac{x_i - \overline{x}}{\sigma x_i}$, where $\overline{x}$ is the average of the distribution of x_i. Notice the non-Gaussian shape of the y vertex pull for the BC vertexed events. All other pull distributions have an expected width. In the main analysis we use the TreeFitter vertexing method but as a cross-check we will also do a fit using values from the BC vertexing technique as well.

Although the error on z_{rec} using the two techniques discussed in this section is larger than for B decays with prompt tracks, the uncertainty on Δz is still dominated by z_{tag} determination. Therefore we will see in section 5.3 that the resolution is comparable to that in $B^0 \rightarrow J/\psi\ K^0_S$.

5.2.3 Extracting Decay Time Difference

Since the $\Upsilon(4S)$ system is boosted in the z direction by $\beta\gamma = 0.55$ the average separation of the B meson vertices is about $260\mu m$. The value of Δz is determined directly by the B_{tag} vertex fit to correctly determine correlations in variables. The fit also provides the uncertainty on Δz, $\sigma_{\Delta z}$, by taking into account the correlations between the B vertices.

A simple estimate of the time difference Δt is given by

$$\Delta z = \beta\gamma c\Delta t \tag{5.11}$$

where $\beta\gamma = 0.55$ and is known with a precision of 0.1%. However this relation only holds if the boost is only in the z direction and the B mesons are at rest in the $\Upsilon(4S)$ frame. However, the boost axis is actually rotated by 20 mrad with respect to the detector z axis and the momentum of the B meson is actually about 340 MeV/c in the $\Upsilon(4S)$ rest frame.

Correcting for these effects, the Δz relation then becomes

$$\Delta z = \beta\gamma\gamma^*_{\text{rec}} c\Delta t + \gamma\beta^*_{\text{rec}}\gamma^*_{\text{rec}} \cos\theta^*_{\text{rec}} c\langle t_{\text{rec}} + t_{\text{tag}}\rangle \tag{5.12}$$

where θ^*_{rec}, β^*_{rec}, and γ^*_{rec} are the polar angle, the velocity, and the boost factor of B_{rec} in the $\Upsilon(4S)$ frame respectively. The expected value of the sum of the decay times is $\langle t_{\text{rec}} + t_{\text{tag}}\rangle$ which can be estimated by

$$\langle t_{\text{rec}} + t_{\text{tag}}\rangle = \tau_B + |\Delta t|. \tag{5.13}$$

The difference in Δt computing with the two different relations has an an RMS spread of 0.20 ps which is small compared to the B^0 lifetime of 1.542 ± 0.016. The resolution on Δt improves by about 5% when using 5.12.

The pull distributions for Δt and Δz are shown in fig 5.2.3 and they all have widths close to one as expected.

5.3 Δt Resolution Function

In fitting the Δt decay distributions we must take into account the Δt resolution from the measurement of the B vertex locations. The Δt PDF 2.50 is convolved with the resolution function to model the impact of the detector effects on the Δt function. The resolution function is parameterized as a sum of three Gaussian distributions (listed in order of increasing width as core, tail, and outlier) as a function of the Δt residual $\delta_t \equiv \Delta t_{meas} - \Delta t_{true}$ and the uncertainty on Δt, $\sigma_{\Delta t}$. The functional form of the resolution function is:

$$\mathcal{R}(\delta_t, \sigma_{\Delta t}, \hat{v}_i) = \sum_{k=core,tail} \frac{f_k}{s_k \sigma_{\Delta t} \sqrt{2\pi}} e^{\left(\frac{(\delta_t - b_k^i \sigma_{\Delta t})^2}{2(s_k \sigma_{\Delta t})} \right)} + \frac{f_{out}}{\sigma_{out} \sqrt{2\pi}} e^{\left(\frac{\delta_t^2}{2\sigma_{out}^2} \right)} \tag{5.14}$$

where the parameters $\hat{v}_i$ are:

- $b_{core,tail}$: The core, tail bias scale factor.
- $s_{core,tail}$: The core, tail sigma scale factor.
- $f_{tail,out}$: The fraction of events in the tail, outlier Gaussian.
- σ_{out} : The width of the outlier Gaussian fixed to 8 ps.

The parameters of the Δt resolution function are determined from signal $B^0 \to K_S^0\ K_S^0\ K_S^0$ MC and for the background they are determined from the maximum likelihood fit.

The functional form of the resolution function allows for a global scaling of the event-by-event estimated errors $\sigma_{\Delta t}$ in both the core and tail Gaussian distributions, as well as a charm bias offset that is also expected to be proportional to $\sigma_{\Delta t}$. The effective widths, σ, and biases, δ^0, of the core and tail components can be written as

$$\sigma_{core,tail} = S_{core,tail} \sigma_{\Delta t}, \tag{5.15}$$

$$\delta^0_{core,tail} = b_{core,tail} \sigma_{\Delta t}. \tag{5.16}$$

Fig 5.12 shows the relation of $\sigma_{\Delta t}$ to the mean and RMS spread of δ_t for MC events with a regular decay vertex like the $B^0 \to J/\psi\ K_S^0$ decay. We will show that the $B^0 \to K_S^0\ K_S^0\ K_S^0$ decay has the same relations between the δ_t, $\sigma_{\Delta t}$, and the true Δt and therefore the same functional form of the resolution function can be used.

As already noted, the tag side vertex is biased due to inclusion of displaced tracks from charm decays. If the direction of the decay of the D meson is the same as the boost direction of the B, the bias along the z direction is enhanced as shown in fig. 5.13. D mesons decaying perpendicular to the flight direction of B have a better z resolution and the least bias in the B_{tag} vertex. The effect of the bias is seen clearly in fig 5.12b where for large values of $\sigma_{\Delta t}$ the residual is about $-0.2\,\text{ps}$.

The outlier Gaussian has no bias and scaling of its width. It has a fixed width of $8\,\text{ps}$ and typically accounts for only a few percent of the events.

5.3.1 Comparison of $B^0 \to K^0_S K^0_S K^0_S$ Decays with Other Decays

In order to use the same resolution function as described in section 5.3 we must confirm that correlations of the residual and $\sigma_{\Delta t}$ are the same as regularly vertexed events. This will be discussed in more detail in section 6.1.1.

We also need to show that the $\sigma_{\Delta t}$ distribution is about the same as regularly vertexed events. The error on the $z_{\rm tag}$ is usually about $180 \mu m$ and is the dominant contribution to the error on Δt for regularly vertexed decays. If the TreeFitter vertexing is to give similar results the Δt error should still receive its major contribution from the tag side. In other words $z_{\rm rec}$ needs to be reconstructed with a better resolution than $z_{\rm tag}$. In order for this to happen we need at least one K^0_S decaying within the SVT. If none of the K^0_S mesons decay inside the SVT the event cannot be used for a time dependent measurement.

In comparison to the decay $B^0 \to K^0_S \pi^0$ decay, which was the first to use this vertexing method, the K^0_S mesons in $B^0 \to K^0_S\ K^0_S\ K^0_S$ have lower average momentum and they therefore have a higher probability of decaying in the SVT. We also only need one K^0_S to reconstruct the vertex so the multiplicity of K^0_S mesons in this decay helps in obtaining a higher fraction of events which decay in the SVT.

In section 5.3.2 we will compare the $\sigma_{\Delta t}$ distributions for $B^0 \to K^0_S K^0_S K^0_S$ and regular vertexed events.

5.3.2 $\sigma_{\Delta t}$ and Classes

Events reconstructed with the TreeFitter vertexing method are classified based on their $\sigma_{\Delta t}$ values which also correspond to the hit pattern within the SVT. Since the K^0_S mesons have a long lifetime they may decay within the DCH or the outer layers of the SVT. The SVT structure is such that the extrapolation precision is achieved if there are hits in the first three layers closest to the beampipe. The outer two layers are mainly used to extrapolate the tracks within the DCH and are therefore placed further from the event vertex. Therefore the classes are defined as:

- Class I: Decays where both pions have at least one ϕ and one z hit in any of the first three inner SVT layers.
- Class II: Decays where both pions have at least one ϕ and one z hit in the SVT but are not in Class I. These events correspond to K^0_S decays beyond the inner three SVT layers.
- Class III: Decays where either of the two pions have at least one SVT hit, but do not satisfy the requirements of Class I or II.

- Class IV: Decays where neither pion has SVT hits.

Fig 5.14 shows $\sigma_{\Delta t}$ versus the shortest flight distance in the x-y plane for the three K^0_S mesons in the event. We see that if the K^0_S decayed after the third SVT layer the error becomes larger as expected. The fourth and fifth layer of the SVT have worse resolution than the first three layers of the SVT. In this analysis and in all *BABAR* time-dependent analysis only events with $\sigma_{\Delta t} < 2.5\,\mathrm{ps}$ and $|\Delta t| < 20\,\mathrm{ps}$ are used.

Fig. 5.15 shows the Δt error distribution for B_{flav} MC events and comparison of nominally vertexed events in data and MC. Fig 5.16 shows the corresponding error distribution for SP5 and SP6 $B^0 \to K^0_S\,K^0_S\,K^0_S$ MC and data divided into different classes of events. We see that when at least one K^0_S is in Class I the Δt error distribution is similar to regularly vertexed events. Events with no Class I but at least one Class II K^0_S can be used for the fit since their Δt resolution is similar to that of decays with prompt particles. In all 99.9$\%$ of events have at least one Class I or Class II K^0_S. For the $B^0 \to K^0_S\,\pi^0$ decay only about 63% of events can be used for the time-dependent fit. Given the smaller branching for $B^0 \to K^0_S\,K^0_S\,K^0_S$ (6.9×10^{-6} versus 11.4×10^{-6}) the new channel provides a measurement with competitive precision because of the much higher vertex reconstruction efficiency.

Events in Class III or Class IV cannot be used since the error for these class of events is too large.

Table 5.3: Tag04 performance from MC events in the 6 tagging categories and the total. The tagging parameters are defined in section 5.1.1

Category	$\epsilon(\%)$	$\Delta\epsilon(\%)$	$\omega(\%)$	$\Delta\omega(\%)$	$Q(\%)$	$\Delta Q(\%)$
Leptons	9.1 ± 0.1	0.1 ± 0.2	2.8 ± 0.1	0.0 ± 0.3	8.2 ± 0.1	0.1 ± 0.2
Kaon I	11.4 ± 0.1	-0.2 ± 0.2	6.2 ± 0.2	0.3 ± 0.4	8.8 ± 0.1	-0.3 ± 0.2
Kaon II	17.4 ± 0.1	0.3 ± 0.2	15.7 ± 0.2	-0.2 ± 0.5	8.2 ± 0.1	0.2 ± 0.2
Kaons and Pions	13.9 ± 0.1	0.3 ± 0.2	25.6 ± 0.3	-1.8 ± 0.6	3.3 ± 0.1	0.6 ± 0.2
Pions	14.3 ± 0.1	-0.5 ± 0.2	34.8 ± 0.3	7.2 ± 0.7	1.4 ± 0.1	-1.3 ± 0.1
Others	9.4 ± 0.1	0.0 ± 0.2	41.8 ± 0.4	5.0 ± 0.8	0.3 ± 0.0	-0.3 ± 0.1
Total	75.5 ± 0.2	0.0 ± 0.5			30.1 ± 0.2	-1.0 ± 0.4

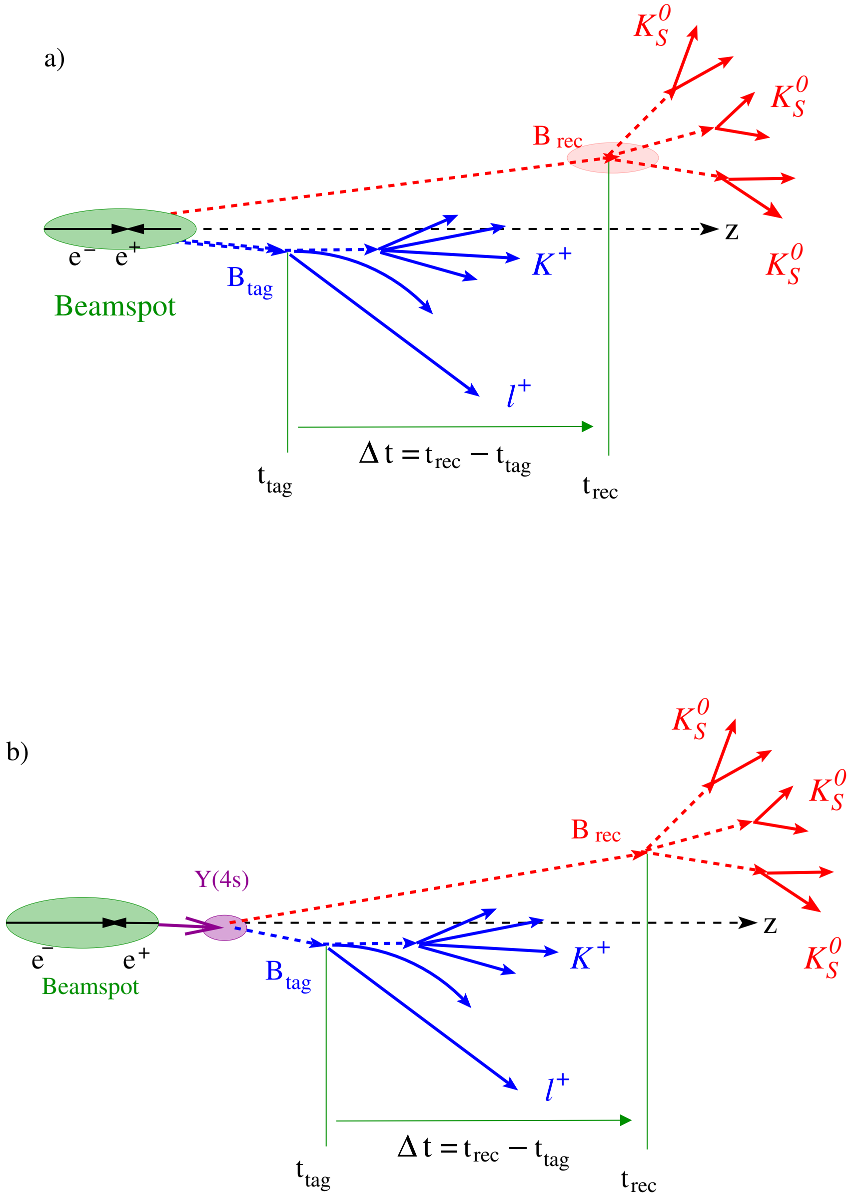

Figure 5.9: The two types of vertexing methods used to reconstruct $B_{\rm rec}$. a) B decay vertex (red ellipse) constrained to the beamspot (green ellipse) and the b) B production point (purple ellipse) constrained to the beamspot (green ellipse).

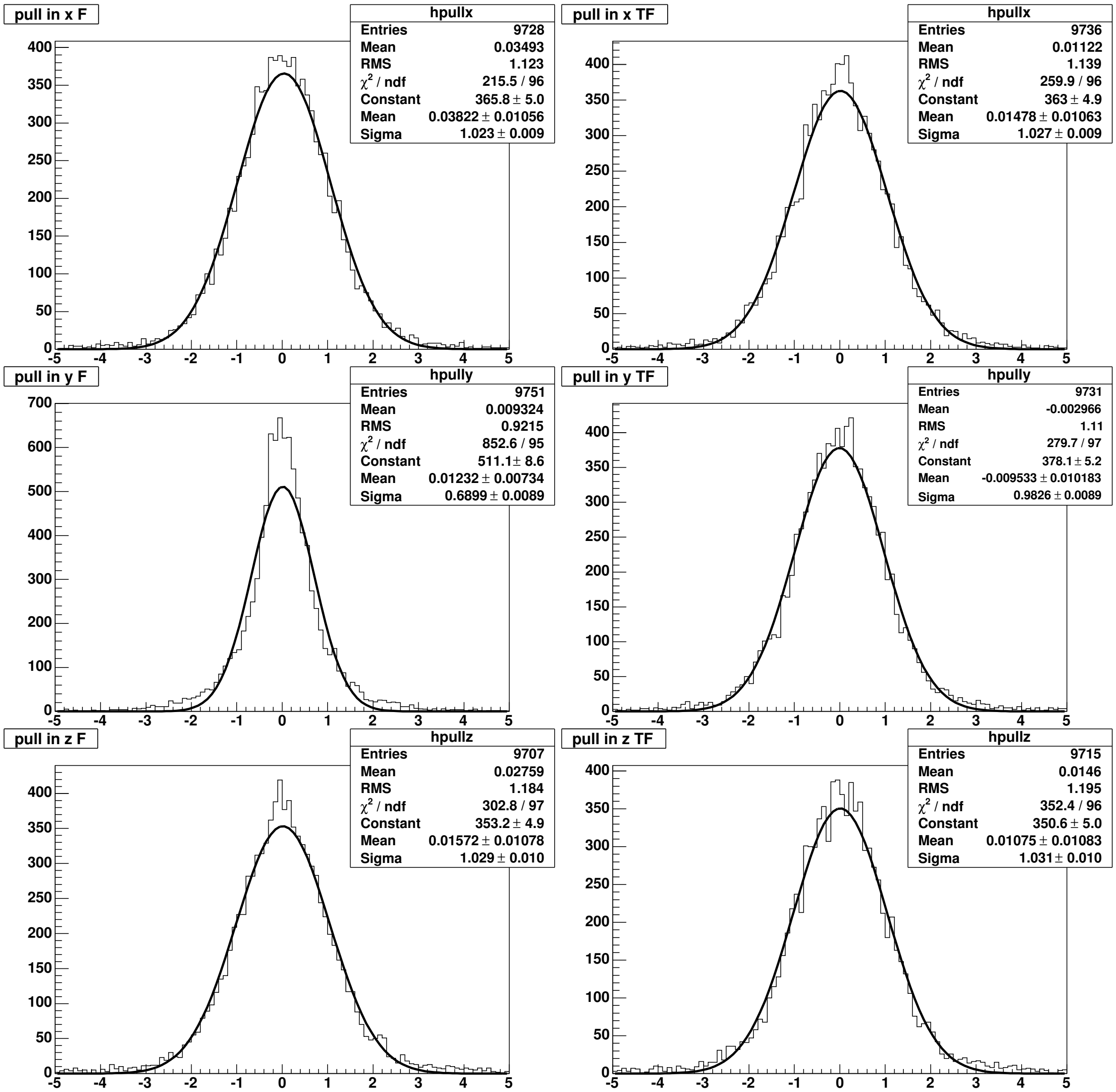

Figure 5.10: Pull distributions in x, y, and z of the decay vertex position of the $B^0 \to K^0_S K^0_S K^0_S$ decay using BC vertexing (F) (left) and TreeFitter (TF) (right).

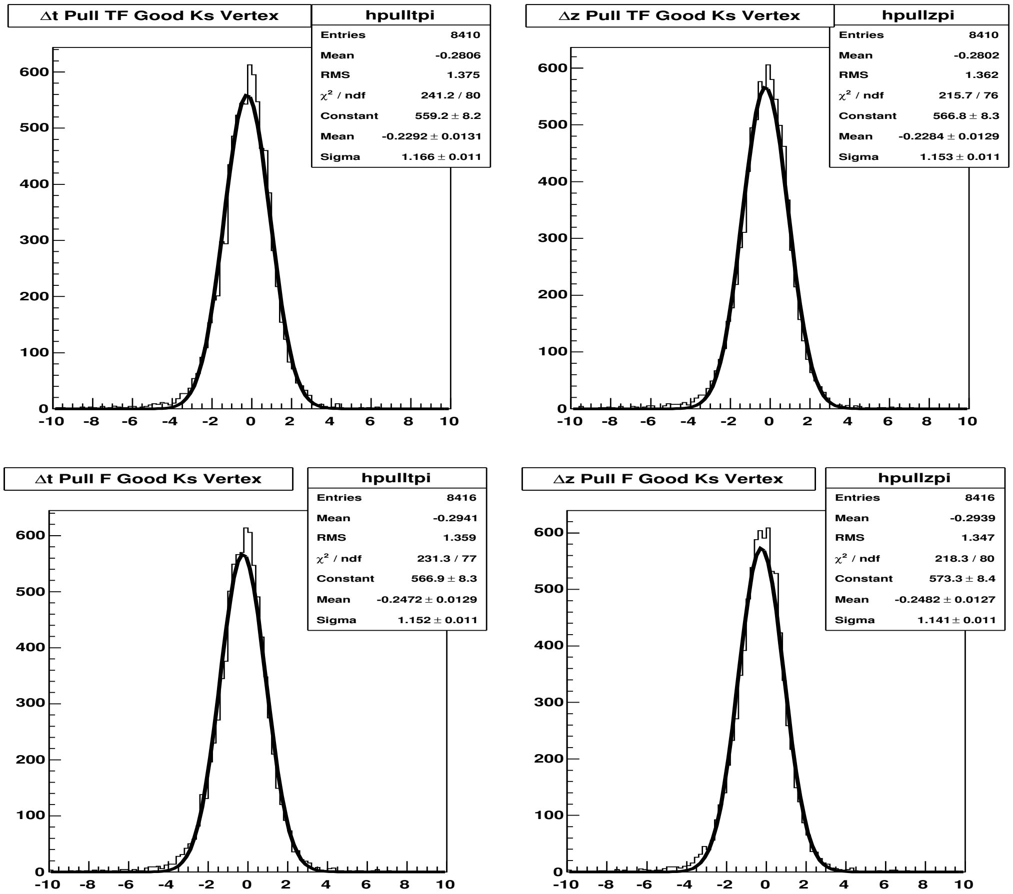

Figure 5.11: The Δz and Δt pull distributions for TreeFitter (TF) and BC vertexing (F).

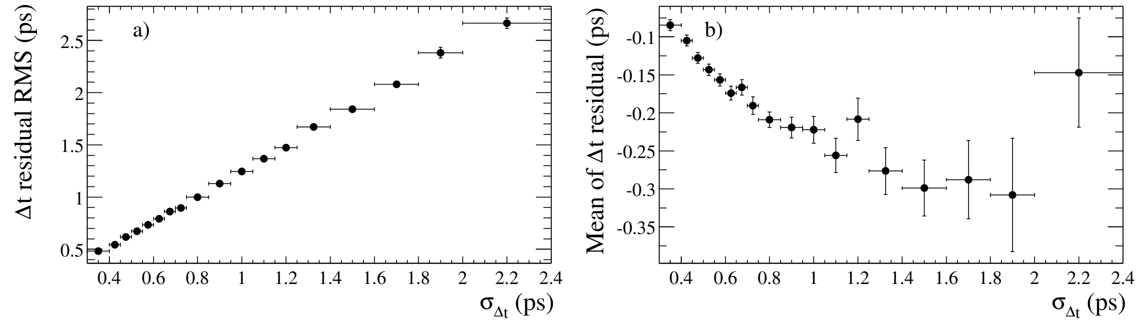

Figure 5.12: Correlation between $\sigma_{\Delta t}$ and a) the RMS spread and b) the mean of the residual $\delta_t = \Delta t_{\text{meas}} - \Delta t_{\text{true}}$ in simulated events with a decay vertex on the B_{rec} side.

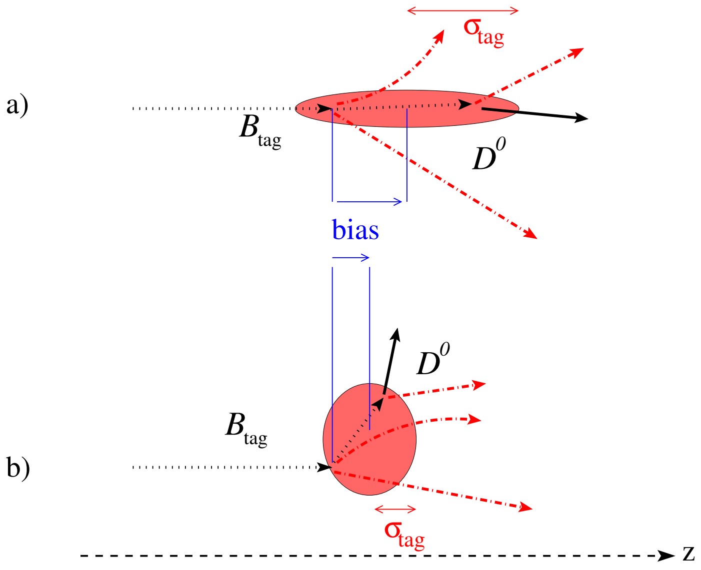

Figure 5.13: Correlation between the bias of the B_{tag} vertex and its uncertainty σ_{tag} when a) the D^0 flies in the boost direction of B_{tag}, or b) the D^0 is perpendicular to the boost direction of B_{tag}.

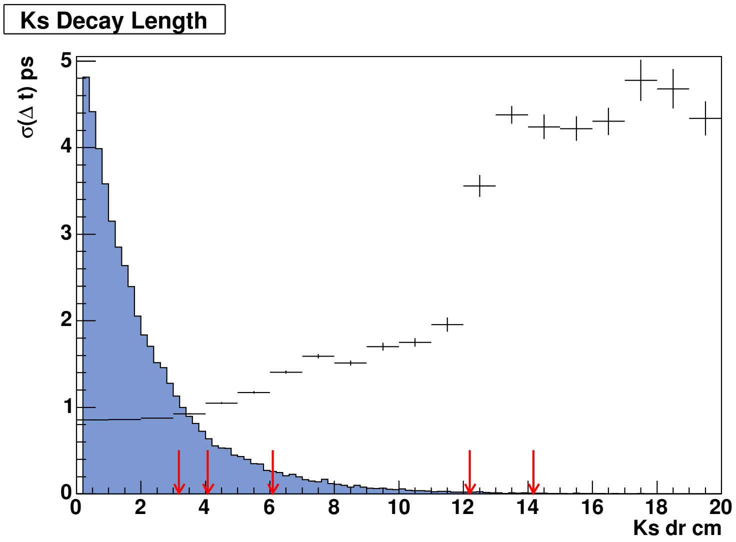

Figure 5.14: Projection plot of $\sigma_{\Delta t}$ versus the flight distance of the K_S^0 in the event with the smallest flight length. Distribution of the K_S^0 flight length in $x - y$ is shown by the filled histogram. The red arrows mark the location of SVT layers.

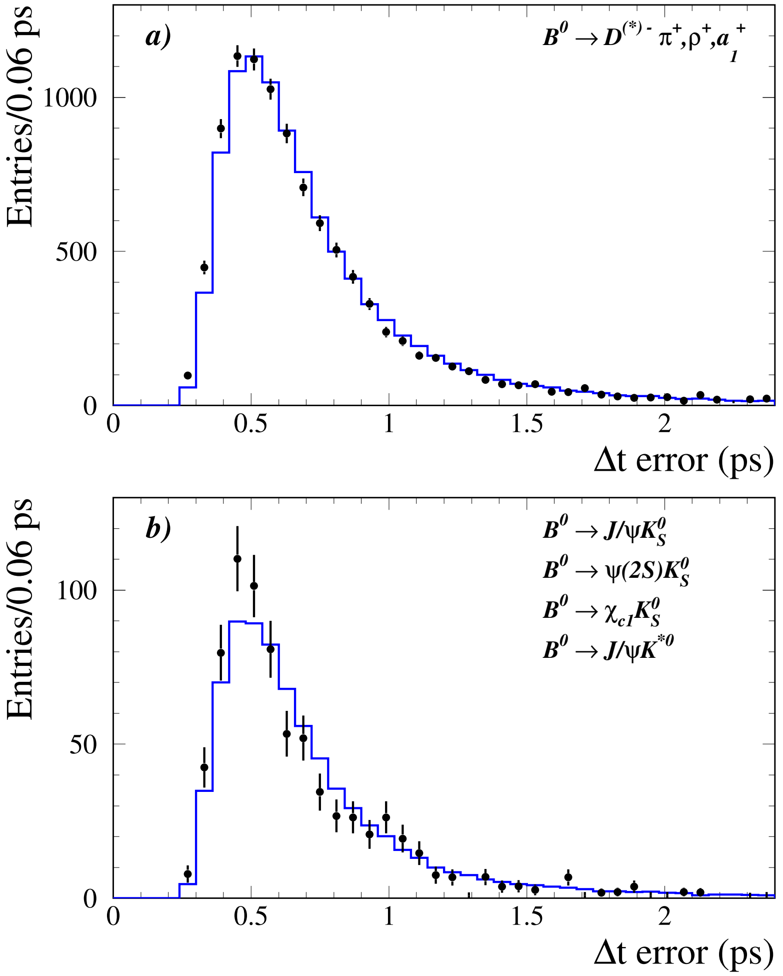

Figure 5.15: Distribution of $\sigma_{\Delta t}$ for a) the B_{flav} sample excluding the $J/\psi\, K^{*0}(K^+\pi^-)$ mode and b)B_{CP} the sample together with the $J/\psi\, K^{*0}$ mode. Points are from data and the open histogram is the expected distribution from Monte Carlo simulation.

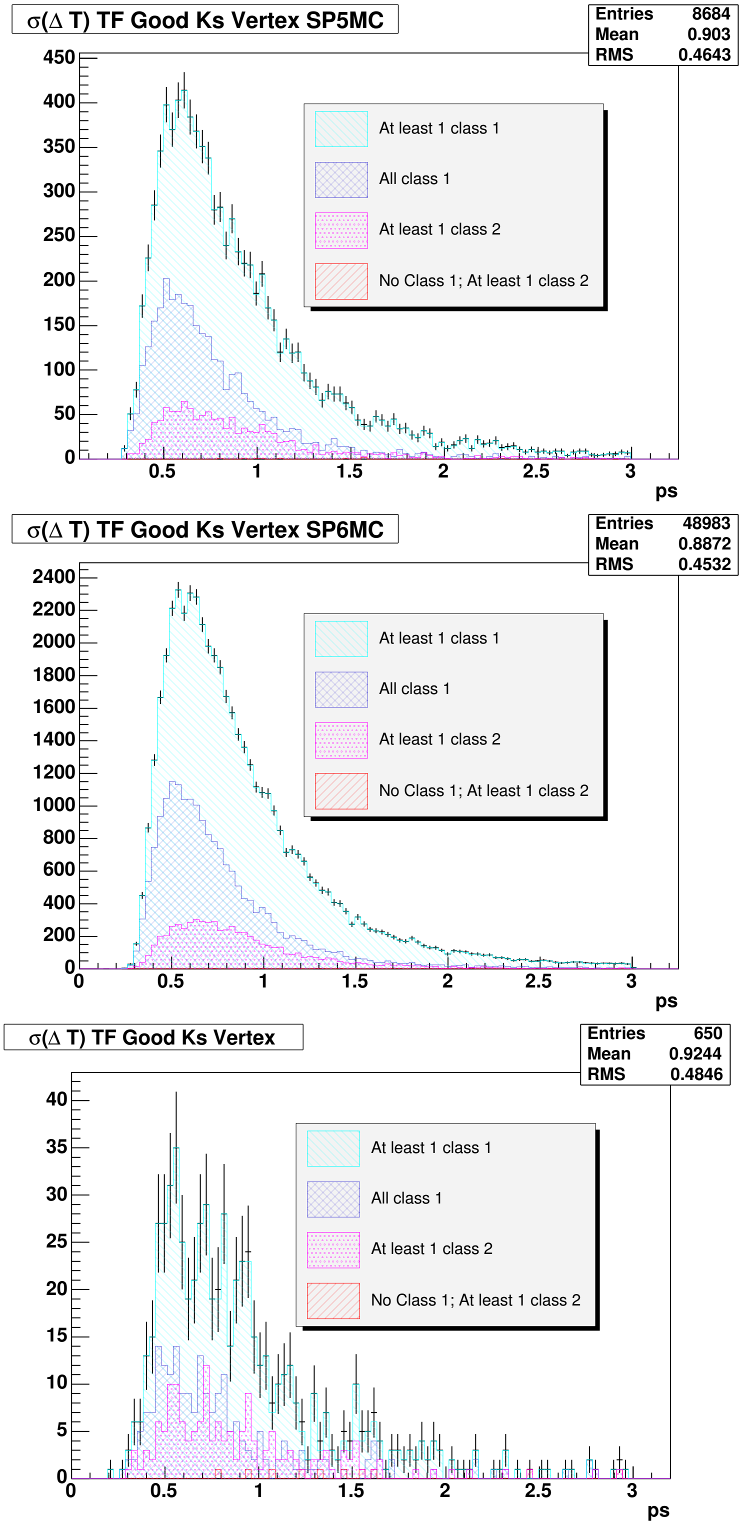

Figure 5.16: Distribution of $\sigma_{\Delta t}$ for SP5 signal MC (top), SP6 signal MC (middle), and data (bottom). Points represent all events and colored open histograms represent the different K_S^0 classifications shown in the key.

Chapter 6

Analysis

Now that we have described all the necessary pieces for doing a time-dependent CP analysis we can go into the details of the $B^0 \to K^0_S\ K^0_S\ K^0_S$ decay. In this chapter we will discuss and validate the Δt resolution function and show that it is indeed similar to the decays with a nominal decay vertex. We will also show that the tagging parameters can be used from the $B_{\rm flav}$ data sample. After these validations, we will parametrize the PDFs for the maximum likelihood fit and explore the impact of any possible correlations between the variables. An extensive set of Toy MC tests are also performed to demonstrate that the fit produces unbiased results. After validating the fit with MC, a blind fit is performed so that we can check that the errors on the asymmetries and the likelihood values are as expected from Toy MC events. We will then present the results and the systematic uncertainties for the measurement. Finally, additional validations are performed to make sure there are no inconsistencies in the data sample.

6.1 Time Structure of the Decay

In sections 5.3.1 and 5.3.2 we discussed how the time structure of the decay of $B^0 \to K^0_S\ K^0_S\ K^0_S$ could be different than nominally vertexed decays. We will have to validate that indeed the resolution function is similar to nominally vertexed events so that we may use the much more precise determination of parameters from the B flavor data sample. If we see that the values from the signal MC are very different from the B flavor MC values we would need to find a different method for extracting the asymmetries. Using TreeFitter to determine the decay vertex could also have some effects on tagging since we are not using the usual constraint from the reconstructed side to determine the $\Upsilon(4S)$ decay point. We must also check that the tagging parameters for $B^0 \to$

K^0_S K^0_S K^0_S signal MC do not differ very much from the B_{flav} MC sample. If the comparisons of the resolution function and the tagging parameters show only small deviations from the B_{flav} MC sample, we are justified in applying the the usual method of fitting for the asymmetries. In this analysis the tagging and resolution function parameters for the data B_{flav} sample are determined from a separate fit.

6.1.1 Resolution Function Validation

The typical resolution function model employed by *BABAR* time-dependent analysis scales the event-by-event errors on Δt, under the assumption that, in the absence of the charm bias, the measured error on Δt due to track parameter errors is a good measure of the resolution in Δt. Figure 6.1 displays the mean and width of the Δt pull defined as $(\Delta t - \Delta t_{\text{true}})/\sigma_{\Delta t}$ for $B^0 \to K^0_S K^0_S K^0_S$ signal MC, and Fig. 6.2 displays the Δt bias. The $B^0 \to K^0_S$ π^0 analysis sees a slight dilution of the charm bias for the BC vertexed events since the resolution is worse. We see that our sensitivity to the charm bias is similar to vertexed events like $B^0 \to J/\psi$ K^0_S.

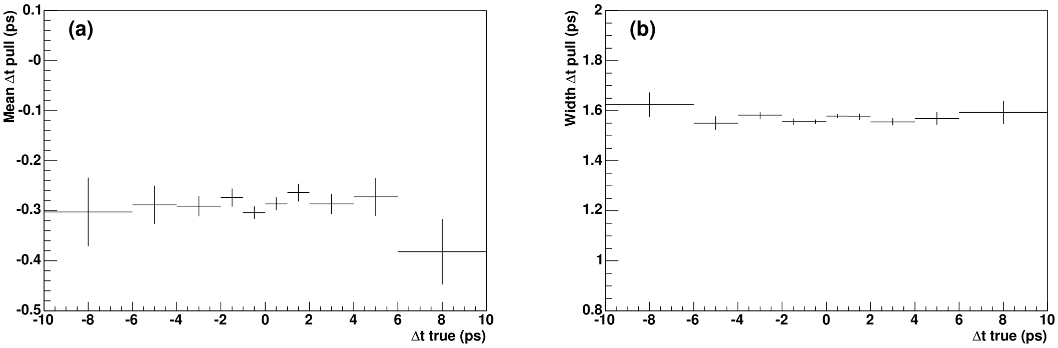

Figure 6.1: a)Mean and b)Width of Δt pull vs. (Δt) true.

As already noted, we observe a correlation between the charm bias in Δt and the estimated uncertainty in Δt, a consequence of inclusively reconstructing the tag side vertex. Therefore all *BABAR* time-dependent analysis adjust Δt on an event-by-event basis with an offset linear in $\sigma_{\Delta t}$ in the resolution function. Figure 6.3 displays the Δt bias versus the estimated uncertainty in Δt for all tagged events. The expected correlation of the mean and width is clearly visible for all samples: the resolution scales with the measured error $\sigma_{\Delta t}$, and the bias roughly scales with the $\sigma_{\Delta t}$ for small values of $\sigma_{\Delta t}$ and flattens out for larger values. Fig. 6.4 shows the Δt bias versus the estimated uncertainty in Δt for the $B^0 \to K^0_S$ π^0 and the $B^0 \to J/\psi$ K^0_S decays overlayed. We do not observe significantly different behavior of the $B^0 \to K^0_S K^0_S K^0_S$ candidates versus other time dependent

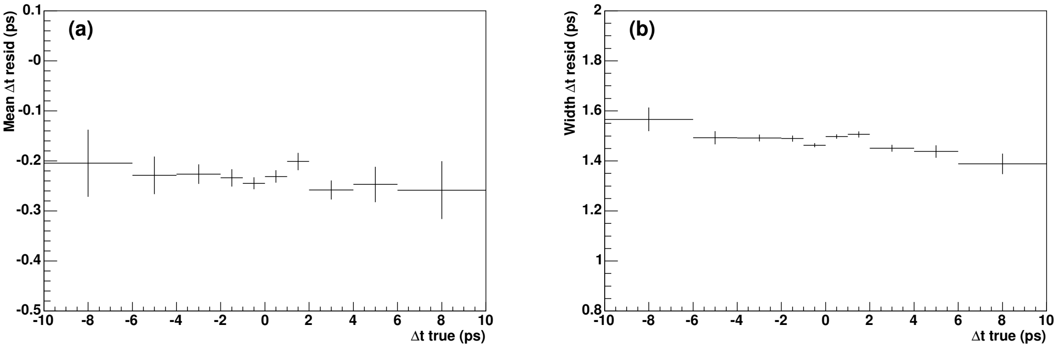

Figure 6.2: a)Mean and b)Width of Δt resid vs. (Δt) true.

analysis like $B^0 \rightarrow J/\psi\ K^0_S$ and $B^0 \rightarrow K^0_S\ \pi^0$ as shown the plots. Therefore we use the standard functional form for the Δt resolution function for $B^0 \rightarrow K^0_S\ K^0_S\ K^0_S$.

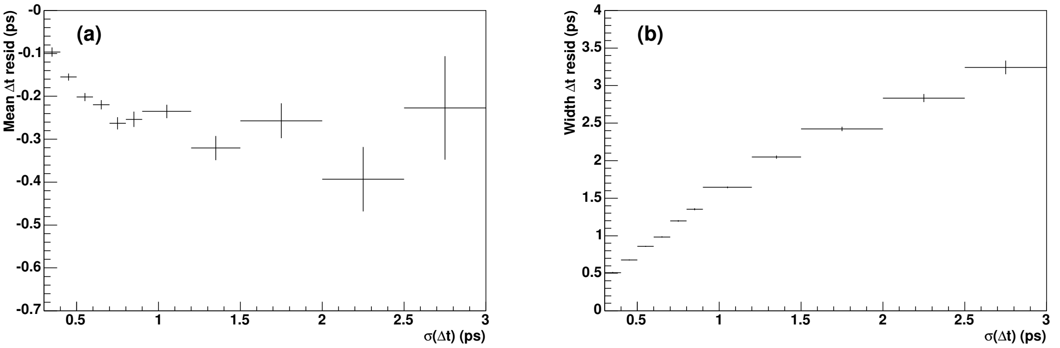

Figure 6.3: a)Mean and b)Width of Δt resid vs. $sigma_{\Delta t}$.

Table 6.1 shows the resolution function parameters, including the tagging efficiencies, for signal MC and for the B_{flav} data sample. We see that the values for signal MC are similar to those in data. We further test the sensitivity of S and C to the resolution function by fitting the asymmetries in MC using the two different sets of resolution function parameters, one from signal MC and one from the B_{flav} data sample. In the former case the asymmetries are fit by floating the resolution function parameters and in the latter case they are fixed to the values from the B_{flav} data sample.

Table 6.2 shows the full floating fit, where the generated value of $S = 0.7$ and $C = 0.0$, and table 6.1.1 shows the results when the resolution function parameters are fixed from the B_{flav} MC sample. We see that S and C are well within the generated values in both cases; therefore, we choose to use the values from the B_{flav} sample for our fit to data. This exercise shows that we do not bias our measured value of S and C by using resolution function parameters from the B_{flav} sample, therefore we are not sensitive to the small deviations of the signal MC values to the B_{flav}

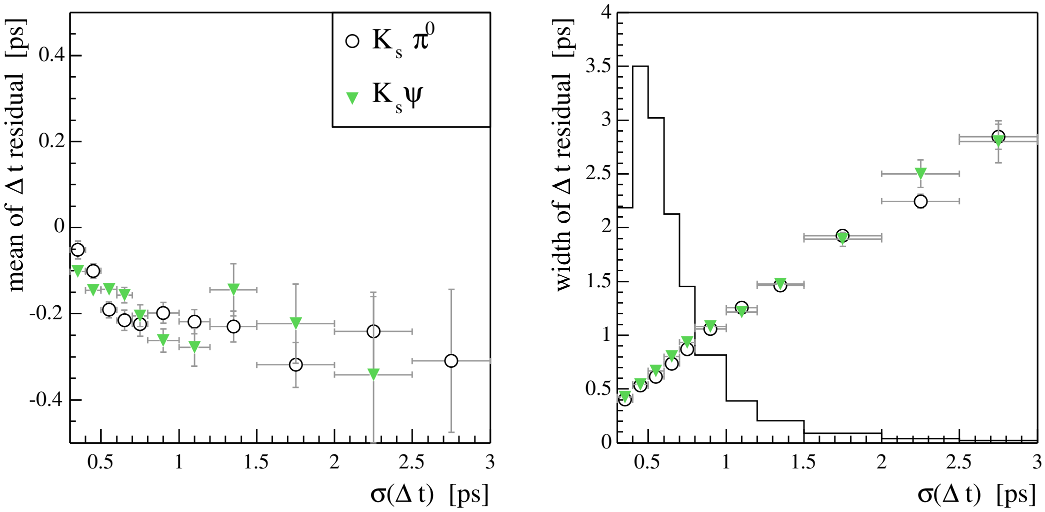

Figure 6.4: Mean and width of the Δt bias, $\Delta t - \Delta t_{\text{true}}$, versus $\sigma_{\Delta t}$ for $B^0 \to K^0_S\, \pi^0$ and nominally vertex $B^0 \to J/\psi\ K^0_S$ candidates. The histogram displays the distribution of $\sigma_{\Delta t}$.

MC values. This validates the use of resolution function parameters from the B_{flav} data sample to fit the asymmetries in our decay.

6.1.2 Comparison of Tagging Parameters

Table 6.1.2 shows the fitted tagging parameters from $B^0 \to K^0_S K^0_S K^0_S$ MC, B_{flav} data, and B_{flav} MC samples. In section 5.1.3 we discussed the fact that tagging parameters from data and MC may differ due to differences in reconstruction efficiency or branching fractions uncertainties. Therefore, when fitting the data we use parameters from the B_{flav} data sample and when fitting the MC we use parameters from the B_{flav} MC sample.

In addition since the $B^0 \to K^0_S K^0_S K^0_S$ is vertexed in a special way we want to make sure that the parameters do not differ significantly between the signal MC and the B_{flav} MC sample. Examining table 6.1.2, we see that the values are indeed consistent. We therefore conclude that we may use the tagging parameters from the B_{flav} data sample to fit the $B^0 \to K^0_S K^0_S K^0_S$ data to extract the asymmetries.

Table 6.1: Fit results for resolution function parameters for signal Monte Carlo and for the B_{flav} data; for signal Monte Carlo, S and C fixed to 0 as expected for this sample.

Parameter	$B^0 \to K^0_S K^0_S K^0_S$ Signal	B_{flav} Data
ϵ_{Cat1}	0.0885 ± 0.0031	0.08746 ± 0.00115
ϵ_{Cat2}	0.1142 ± 0.0034	0.10886 ± 0.00139
ϵ_{Cat3}	0.1658 ± 0.004	0.17138 ± 0.00168
ϵ_{Cat4}	0.1338 ± 0.0037	0.13581 ± 0.00156
ϵ_{Cat5}	0.1489 ± 0.0038	0.146895 ± 0.000695
ϵ_{Cat6}	0.0897 ± 0.0031	0.0992 ± 0.00123
b^{Cat1}_{core}	-0.06 ± 0.11	-0.0481 ± 0.044
b^{Cat2}_{core}	-0.211 ± 0.094	-0.103 ± 0.0428
b^{Cat3}_{core}	-0.206 ± 0.074	-0.1974 ± 0.0336
b^{Cat4}_{core}	-0.157 ± 0.08	-0.2154 ± 0.0355
b^{Cat5}_{core}	-0.146 ± 0.074	-0.2016 ± 0.0343
b^{Cat6}_{core}	-0.226 ± 0.096	-0.1514 ± 0.0413
b^{NoTag}_{core}	-0.187 ± 0.056	-0.2057 ± 0.0269
s_{core}	1.124 ± 0.058	1.0569 ± 0.0279
f_{out}	0.0057 ± 0.0023	0.004342 ± 0.00087
f_{tail}	0.052 ± 0.026	0.0937 ± 0.0119
b_{tail}	-1.05 ± 0.73	-1.242 ± 0.206

Table 6.2: Fit results for S and C obtained from signal Monte Carlo, with floating resolution function parameters.

Parameter	$B^0 \to K^0_S K^0_S K^0_S$ Signal
$S_{3K^0_S}$	0.671 ± 0.049
$C_{3K^0_S}$	0.061 ± 0.035
ϵ_{Cat1}	0.0923 ± 0.0042
ϵ_{Cat2}	0.1141 ± 0.0046
ϵ_{Cat3}	0.1641 ± 0.0054
ϵ_{Cat4}	0.1322 ± 0.0049
ϵ_{Cat5}	0.1445 ± 0.0051
ϵ_{Cat6}	0.0868 ± 0.0041
b^{Cat1}_{core}	-0.11 ± 0.14
b^{Cat2}_{core}	-0.26 ± 0.12
b^{Cat3}_{core}	-0.198 ± 0.097
b^{Cat4}_{core}	-0.22 ± 0.1
b^{Cat5}_{core}	-0.102 ± 0.098
b^{Cat6}_{core}	-0.37 ± 0.12
b^{NoTag}_{core}	-0.246 ± 0.07
s_{core}	1.073 ± 0.066
f_{out}	0.0051 ± 0.0028
f_{tail}	0.057 ± 0.028
b_{tail}	-0.72 ± 0.68

Table 6.3: Fit results for S and C from signal MC. The resolution function parameters and tagging parameters have been fixed to the B_{flav} MC values.

Parameter	$S = 0.0\ C = 0.0$	$S = 0.8\ C = 0.2$
$S_{3K^0_S}$	0.015 ± 0.011	0.823 ± 0.020
$C_{3K^0_S}$	0.014 ± 0.017	0.214 ± 0.015

Table 6.4: Dilutions D, dilution asymmetry ΔD, tagging efficiency asymmetry μ, and tagging efficiency ϵ for each category for $B^0 \to K^0_S K^0_S K^0_S$ MC, B_{flav} MC, B_{flav} data

Parameter	$B^0 \to K^0_S K^0_S K^0_S$ MC	B_{flav} MC	B_{flav} Data
ΔD_{Cat1}	0.0081 ± 0.0101	-0.0086 ± 0.0182	0.0057 ± 0.0180
ΔD_{Cat2}	-0.0045 ± 0.0131	-0.0073 ± 0.0203	0.041 ± 0.0190
ΔD_{Cat3}	0.0516 ± 0.0170	0.0231 ± 0.0205	0.0285 ± 0.0190
ΔD_{Cat4}	0.0312 ± 0.0220	0.0240 ± 0.0237	0.0018 ± 0.0227
ΔD_{Cat5}	-0.1540 ± 0.0233	0.1115 ± 0.0234	-0.1246 ± 0.0225
ΔD_{Cat6}	-0.1064 ± 0.0297	0.0562 ± 0.0285	-0.0843 ± 0.0272
D_{Cat1}	0.9453 ± 0.0050	0.9658 ± 0.0093	0.9364 ± 0.0094
D_{Cat2}	0.8795 ± 0.0066	0.8743 ± 0.0109	0.9001 ± 0.0101
D_{Cat3}	0.6636 ± 0.0085	0.6622 ± 0.0121	0.6916 ± 0.0111
D_{Cat4}	0.4952 ± 0.0110	0.4842 ± 0.0148	0.5426 ± 0.0140
D_{Cat5}	0.2887 ± 0.0116	0.3021 ± 0.0151	0.3377 ± 0.0146
D_{Cat6}	0.1541 ± 0.0148	0.1856 ± 0.0187	0.1821 ± 0.0183
$\Delta\epsilon_{Cat1}$	0.0133 ± 0.0154	-0.0097 ± 0.0185	0.0034 ± 0.0164
$\Delta\epsilon_{Cat2}$	-0.0154 ± 0.0138	0.0181 ± 0.0170	-0.0287 ± 0.0156
$\Delta\epsilon_{Cat3}$	0.0050 ± 0.0114	0.0218 ± 0.0155	-0.0025 ± 0.0139
$\Delta\epsilon_{Cat4}$	-0.0003 ± 0.0127	0.0586 ± 0.0172	-0.0089 ± 0.0161
$\Delta\epsilon_{Cat5}$	-0.0336 ± 0.0122	-0.0108 ± 0.0170	-0.0201 ± 0.016
$\Delta\epsilon_{Cat6}$	0.0136 ± 0.0150	-0.0039 ± 0.0201	0.0089 ± 0.0191
ϵ_{Cat1}	0.0875 ± 0.0013	0.0850 ± 0.0013	0.0875 ± 0.0012
ϵ_{Cat2}	0.1094 ± 0.0014	0.1132 ± 0.0015	0.1089 ± 0.0014
ϵ_{Cat3}	0.1606 ± 0.0017	0.1681 ± 0.0016	0.1714 ± 0.0017
ϵ_{Cat4}	0.1292 ± 0.0015	0.1402 ± 0.0016	0.1358 ± 0.0016
ϵ_{Cat5}	0.1400 ± 0.0016	0.1489 ± 0.0016	0.1469 ± 0.0007
ϵ_{Cat6}	0.0919 ± 0.0013	0.1018 ± 0.0014	0.0992 ± 0.0012

6.2 Correlations Between Variables

The maximum likelihood fit uses the variables $m_{\rm ES}$, ΔE, $\mathcal{F}$, and Δt and is discussed in detail in section 6.3. This fit model assumes no correlations among the input variables and the existence of correlations will lead to biases in the fit. Correlations in the signal could lead to a larger signal yield and correlations in the background will lead to lower signal yields.

Figures 6.5 and 6.6 show the various correlation plots between $\mathcal{F}$, $m_{\rm ES}$, and ΔE for signal MC events and background data events respectively. As expected there is a correlation between $m_{\rm ES}$ and ΔE in the signal due to the common uncertainty on the beam energy and material correction for the K_S^0 which are not accurate and therefore introduce a momentum-mass correlation which translates into a $m_{\rm ES}$-ΔE correlation. The correlation coefficient of $m_{\rm ES}$ and ΔE is 22.4%.

Figures 6.7 and 6.9 show the correlations of Δt and $\sigma(\Delta t)$ versus $\mathcal{F}$, $m_{\rm ES}$, and ΔE respectively. The corresponding background plots are shown in Figs. 6.8 and 6.10. With exception to the correlations in $m_{\rm ES}$ and ΔE, we see no significant correlations between the other variables.

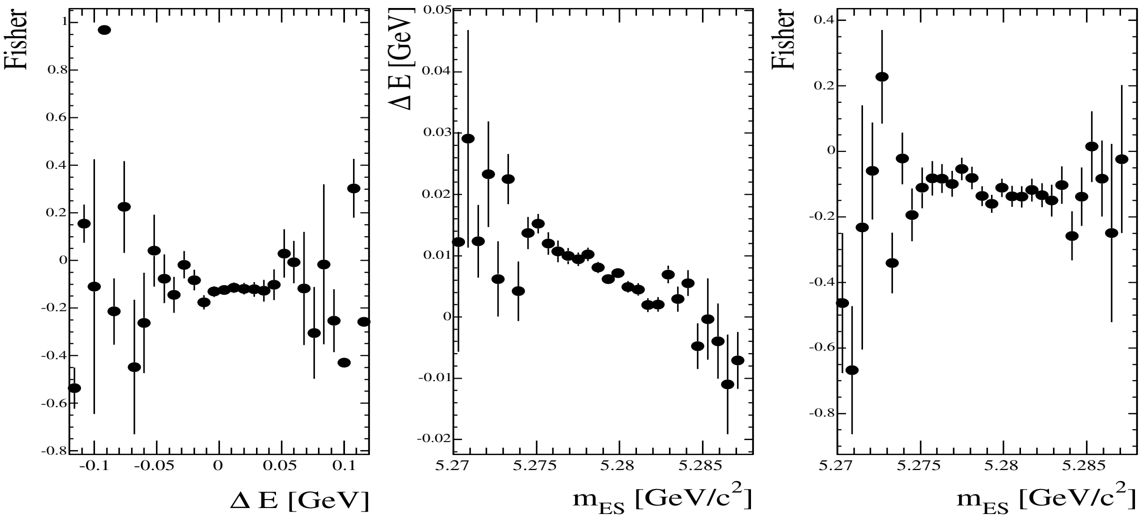

Figure 6.5: Correlation profile plots of $\mathcal{F}$ versus ΔE (left), ΔE vs $m_{\rm ES}$ (middle), and $\mathcal{F}$ versus $m_{\rm ES}$ (right) for truth matched signal MC.

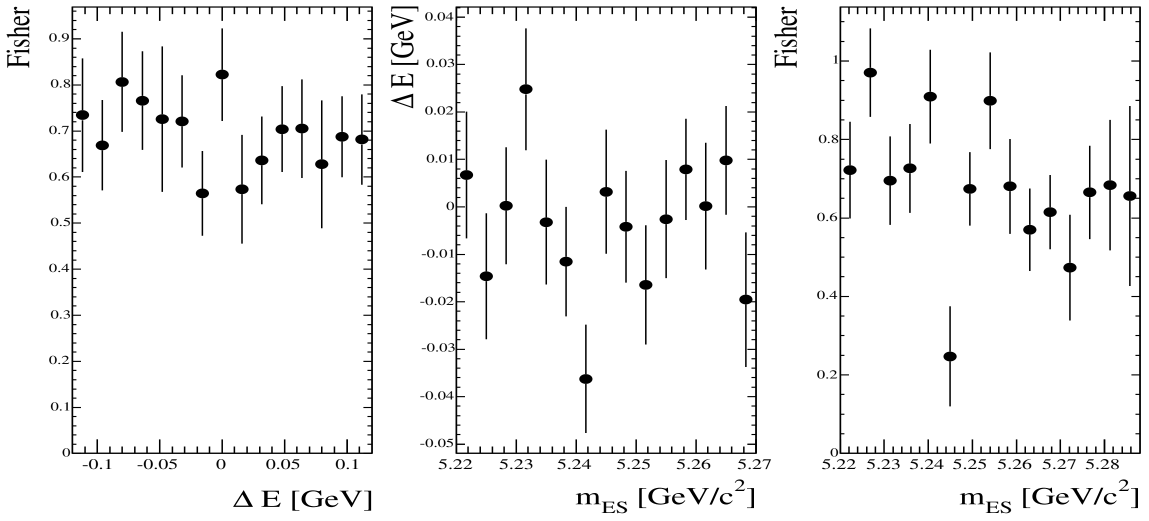

Figure 6.6: Correlation profile plots of $\mathcal{F}$ versus ΔE (left), ΔE vs $m_{\rm ES}$ (middle), and $\mathcal{F}$ versus $m_{\rm ES}$ (right) for background data sidebands. Plot of $\mathcal{F}$ versus $m_{\rm ES}$ uses data events with $|\Delta E| < 0.04\,\text{GeV}$ and the two other plots use data events with $m_{\rm ES} < 5.27\,\text{GeV}$

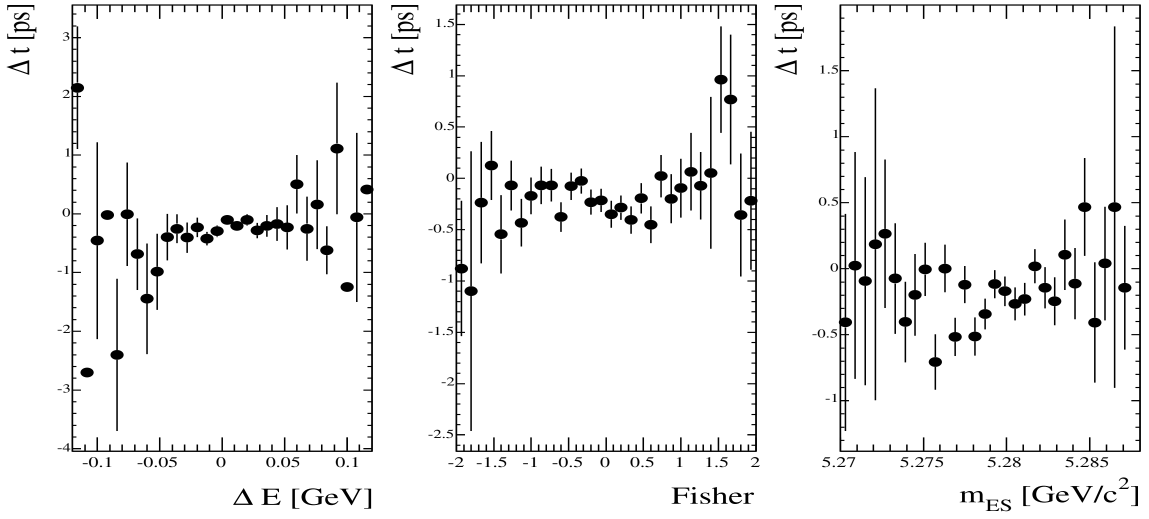

Figure 6.7: Correlation profile plots of Δt versus $\mathcal{F}$ (left), ΔE (middle), and $m_{\rm ES}$ (right) for truth matched signal MC events.

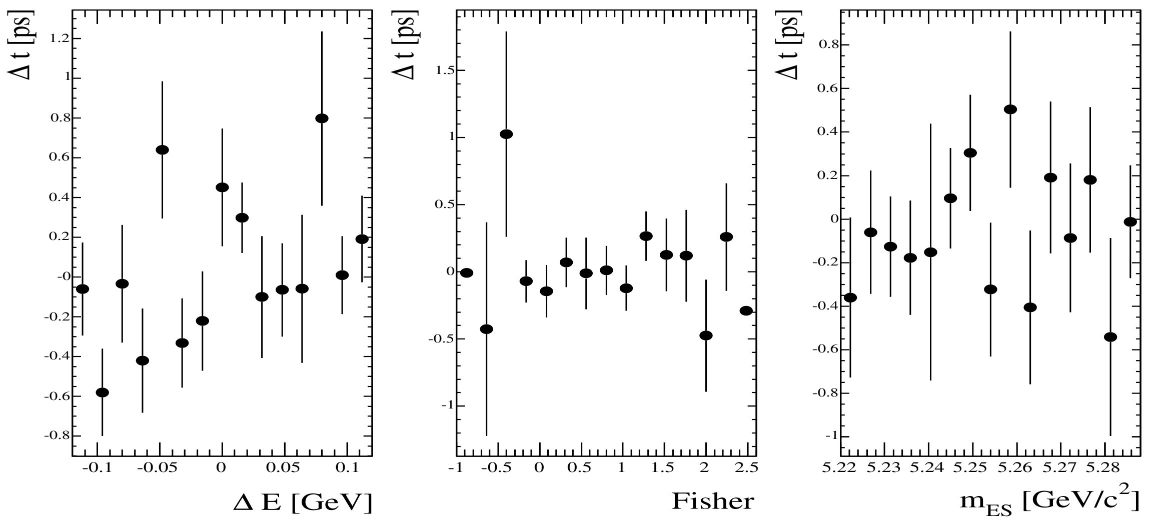

Figure 6.8: Correlation profile plots of Δt versus $\mathcal{F}$ (left), ΔE (middle), and m_{ES} (right) for background data events. The plot of Δt versus m_{ES} uses data events with $|\Delta E| < 0.04\,\mathrm{GeV}$ and the two other plots use data events with $m_{\mathrm{ES}} < 5.27\,\mathrm{GeV}$

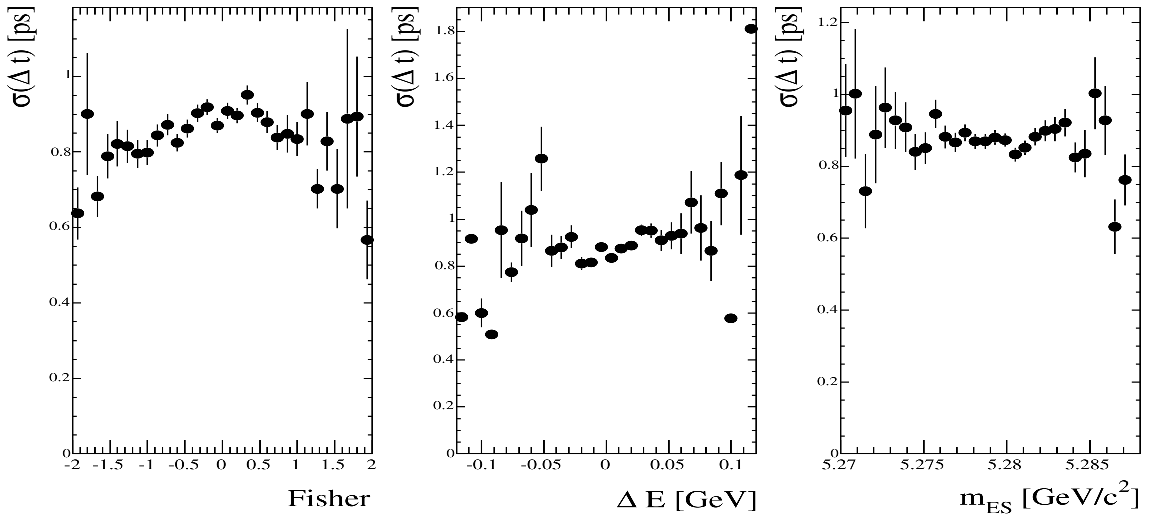

Figure 6.9: Correlation profile plots of $\sigma(\Delta t)$ versus $\mathcal{F}$ (left), ΔE (middle), and m_{ES} (right) for truth matched signal MC events.

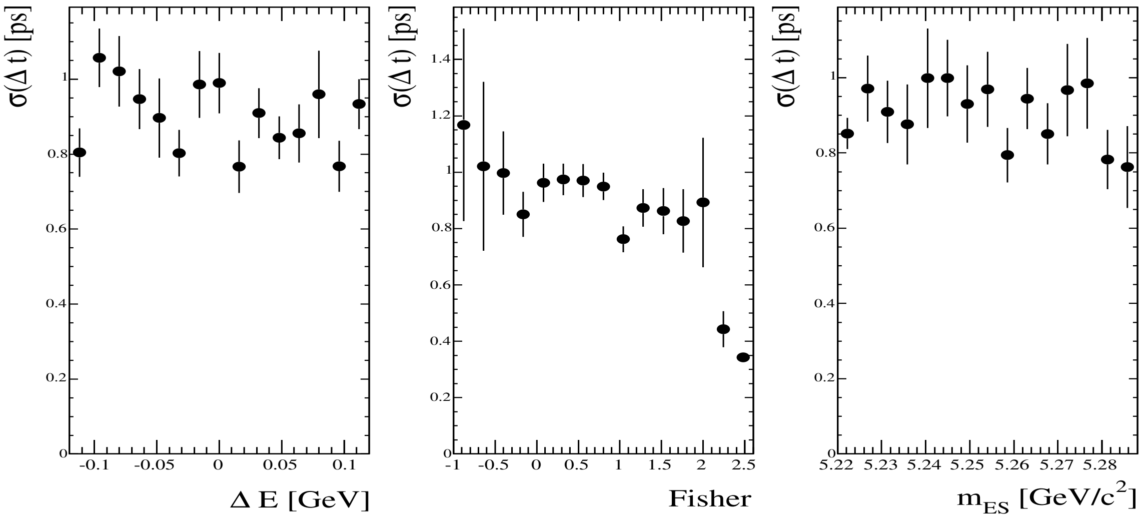

Figure 6.10: Correlation profile plots of $\sigma(\Delta t)$ versus $\mathcal{F}$(left), ΔE (middle), and m_{ES} (right) for background data events. The plot of $\sigma(\Delta t)$ versus m_{ES} uses data events with $|\Delta E| < 0.04\,\mathrm{GeV}$ and the two other plots use data events with $m_{\mathrm{ES}} < 5.27\,\mathrm{GeV}$

6.3 The Maximum Likelihood Fit

As explained in section 4.4, the time-dependent fit to $B^0 \to K_S^0 K_S^0 K_S^0$ events uses $m_{\rm ES}$, ΔE, $\mathcal{F}$, and Δt to extract $S_{3K_S^0}$ and $C_{3K_S^0}$ along with the signal and continuum background yields and various background parameters from the input dataset. In addition we use the tag04 flavor tag (T), and the tag04 tagging categories (c) to take into account the tagging imperfections and to split different physics parameters according to the tagging categories. We also saw that the Δt PDF is convolved with a resolution function which is a function of $\sigma_{\Delta t}$, therefore this variable is utilized to parametrize the data correctly.

Since we make no Δt or $\sigma_{\Delta t}$ cuts in the selection of the fit sample, we must use events which have a good measured Δt before fitting. We use events which satisfy the requirements

- have a Δt measurement,
- $|\Delta t| < 20$ ps,
- $\sigma_{\Delta t} < 2.5$ ps,
- satisfy the requirement of class I or II (Note: Only a few events are removed by this requirement.).

Then the likelihood function used in the fit may be expressed as:

$$\begin{aligned} L = \frac{e^{-(N_S+N_B)}}{(N_S+N_B)!}\prod_i^N\{N_S\epsilon_{c_i}^S &\cdot P_S(m_{\rm ES}{}_i)P_S(\Delta E_i)P_S(\mathcal{F}_i)P_S^c(\Delta t_i, T|\sigma_{\Delta t_i}) + \\ N_B\epsilon_{c_i}^B &\cdot P_B(m_{\rm ES}{}_i)P_B(\Delta E_i))P_B(\mathcal{F}_i)P_B^c(\Delta t_i, T|\sigma_{\Delta t_i})\} \end{aligned} \tag{6.1}$$

where

- N is the total number of events,
- $N_{S,B}$ are the signal and background yields, and
- $\epsilon_c^{S,B}$ are the signal and background tagging efficiencies.

The floating parameters in the fit are listed in table 6.3. The values for dilutions, Δ dilutions, tagging category efficiencies, tagging category efficiency asymmetries, and Δt resolution function parameters for the signal are taken from a separate fit to the $B_{\rm flav}$ data sample. In the next section we will show the parameterizations used to perform the fits.

6.3.1 PDF Parameterizations for ML Fit

The parametrization of the data in the ML fit is divided into three variable types: kinematic and event shape variables (m_{ES}, ΔE, $\mathcal{F}$), Δt, and $\sigma_{\Delta t}$. We saw in table 6.3 that the signal parameters are all fixed, except for the asymmetries and the yields, and the background parameters are what is being actually fit. In general we use the signal MC sample to parametrize the signal and the data sidebands to parametrize the background. We will use the fitted values from parameterizing each variable separately as the starting value given to the fit for the background. We will then show the functional form of Δt for the signal and background including all tagging and resolution effects. The parametrization of $\sigma_{\Delta t}$ is only used for the Toy MC events. This will be discussed further later in this section.

m_{ES}, ΔE, and $\mathcal{F}$

We parameterize m_{ES}, ΔE, and $\mathcal{F}$ distributions of $B^0 \to K^0_S K^0_S K^0_S$ from the signal Monte Carlo sample.

Figure 6.11 displays the m_{ES} distributions of the two components considered in the full fit. We parameterize the signal by fitting a Crystal Ball function to the signal MC [28]. The function is defined as

$$\begin{aligned} C(x) = & \quad \frac{1}{N} e^{-\frac{(x-\mu)^2}{2\sigma^2}}, & \quad \frac{x-\mu}{\sigma} < \alpha \\ C(x) = & \quad \frac{1}{N} \frac{(\frac{n}{\alpha})^n e^{\frac{-\alpha^2}{2}}}{(-\frac{x-\mu}{\sigma}+\frac{n}{\alpha}-\alpha)^n}, & \quad \frac{x-\mu}{\sigma} \geq \alpha. \end{aligned} \tag{6.2}$$

where N is a normalization factor.

The parameters are

- $\mu m_{\mathrm{ES}} = 5.2794 \pm 2.8519 \times 10^{-5}$ GeV/c,
- $\sigma m_{\mathrm{ES}} = 0.0025742 \pm 2.1326 \times 10^{-5}$ GeV/c,
- $\alpha m_{\mathrm{ES}} = 2.6896 \pm 0.073899$,
- $N m_{\mathrm{ES}} = 0.74587 \pm 0.092578$.

The background m_{ES} sample is taken from data with $|\Delta E| > 40\,\mathrm{MeV}$. Most *BABAR* analyses parameterize the background m_{ES} with an ARGUS function [29] with ξ_c parameters which depend on tagging category. The functional form of the ARGUS function is

$$\frac{dN}{dm_{\mathrm{ES}}} = N \cdot m_{\mathrm{ES}} \cdot \sqrt{1-x^2} \cdot \exp\left(-\xi \cdot (1-x^2)\right). \tag{6.3}$$

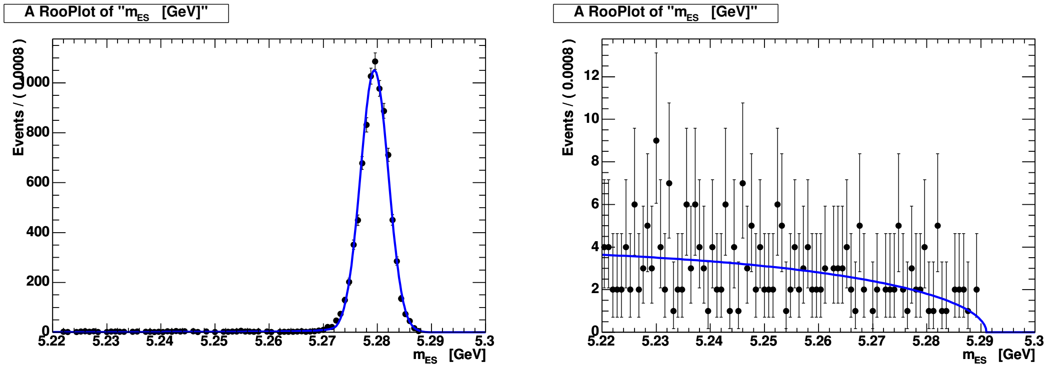

Figure 6.11: The m_{ES} distributions of signal $B^0 \rightarrow K^0_S K^0_S K^0_S$ Monte Carlo and data $|\Delta E| > 40\,\mathrm{MeV}$ sidebands, fitted to a Crystal Ball and ARGUS function, respectively.

When fitting each category separately we saw that only three out of seven categories have a fit which converges due to limited statistics. We chose not to split the background m_{ES} shape by tagging category to avoid having to fix the shape in the categories which have low statistics. We also see that the fits that do converge have large errors and therefore it not possible to demonstrate one way or the other whether there is variation with tagging category. The ARGUS shape parameter ξ is determined in the maximum likelihood fit. The values of ξ for the 3 converged categories and the total fit are

- $\xi_{\mathrm{Cat3}} = -27.7 \pm 26.1$,
- $\xi_{\mathrm{Cat5}} = -43.7 \pm 22.4$,
- $\xi_{\mathrm{NoTag}} = -10.3 \pm 15.0$,
- $\xi_{\mathrm{All}} = -9.8 \pm 9.1$.

Figure 6.12 displays the ΔE distribution of signal and background. We fit the signal distribution with the Cruijff function [30], which is defined as

$$f(x)_{\mathrm{cruijff}} = e^{\left(\frac{(x-\mu)^2}{2\sigma_\pm^2+\alpha_\pm(x-\mu)^2}\right)}. \tag{6.4}$$

The signal parameters are

- $\mu_{\Delta E} = 0.0075 \pm 0.0005\,\mathrm{GeV}/c$,
- $\sigma^L_{\Delta E} = 0.0139 \pm 0.0004\,\mathrm{GeV}/c$,
- $\sigma^R_{\Delta E} = 0.0133 \pm 0.0004\,\mathrm{GeV}/c$,

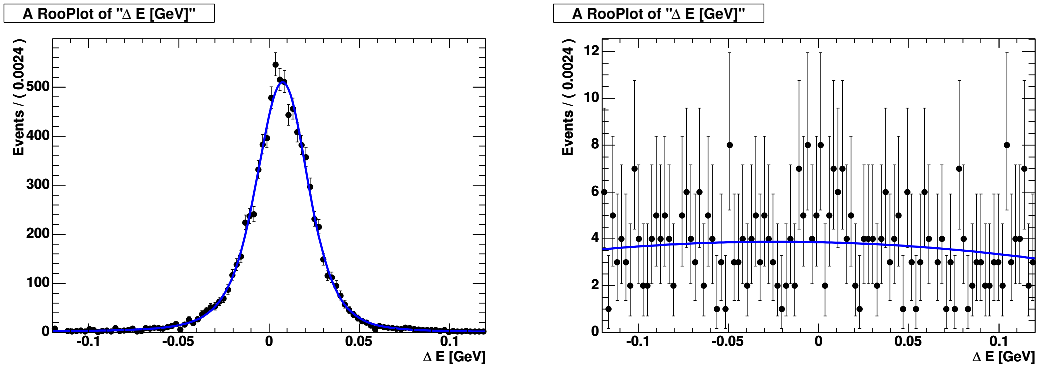

Figure 6.12: The ΔE distributions of signal $B^0 \rightarrow K^0_S K^0_S K^0_S$ Monte Carlo and data, $m_{\rm ES} < 5.27\,{\rm GeV}/c^2$, sidebands. The fits are to a Cruijff function and a 2nd order polynomial respectively

- $\alpha^L_{\Delta E} = 0.1660 \pm 0.0050\,{\rm GeV}/c$,
- $\alpha^R_{\Delta E} = 0.1523 \pm 0.0055\,{\rm GeV}/c$.

We parameterize the background ΔE distribution with a quadratic function whose parameters are determined in the maximum likelihood fit.

We parameterize the signal Fisher distribution with a bifurcated Gaussian function. A bifurcated Gaussian is a guassian with a different width on the left and right side. The signal parameters are (see fig. 6.13)

- $\mu_{\mathcal{F}} = -0.0405 \pm 0.0166$
- $\sigma^L_{\mathcal{F}} = 0.6748 \pm 0.0110$,
- $\sigma^R_{\mathcal{F}} = 0.5533 \pm 0.0105$.

We parameterize the background Fisher with a bifurcated Gaussian function with parameters determined from the maximum likelihood fit.

Table 6.3.1 summarizes the PDFs used for the signal and background variables and the sample used for determining the parameterization.

Time Difference Δt Distributions

As discussed in section 6.1.1, we use the Δt resolution function parameters obtained from the $B_{\rm flav}$ data sample to model the signal. We also assume that the parameters describing the tagging

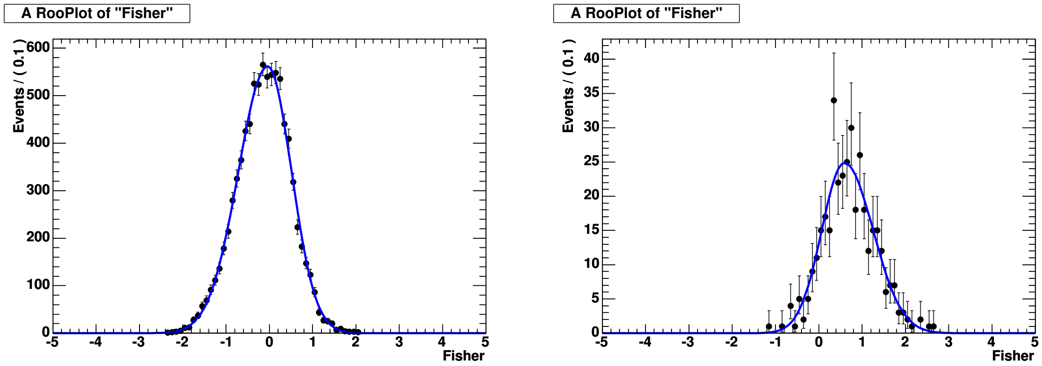

Figure 6.13: The $\mathcal{F}$ distributions of signal $B^0 \to K^0_S K^0_S K^0_S$ Monte Carlo and $5.2 < m_{\rm ES} < 5.27\,{\rm GeV}/c^2$ sidebands , both fitted with bifurcated Gaussian functions.

performance are the same in events with a $B^0 \to K^0_S K^0_S K^0_S$ decay as other B^0 decays. These parameters are the dilutions D_c, dilution asymmetries ΔD_c, tagging efficiency asymmetries $\Delta\epsilon_c$, and the average tagging efficiency ϵ_c. The tagging and resolution function parameter values used to fit the signal are shown in table 6.3.1.

We model the background Δt resolution function with the same form as the signal, but with separate parameters. The underlying Δt distribution is a delta function centered at $\Delta t = 0$. We fix $\sigma_{\rm out} = 8\,{\rm ps}$, $\sigma_{\rm tail} = 3\,{\rm ps}$, $\epsilon_{\rm Cat1} = 0.0027$, and $\Delta\epsilon_{\rm Cat1} = 0$. The lepton category (Cat 1) for the background is fixed due to the limited number of continuum-produced background events in the lepton sample.

Figure 6.14 show the Δt fit to $m_{\rm ES} < 5.27\,{\rm GeV}/c^2$ data sideband region. We also show the fit on a logarithmic scale to better show the events in the tail Gaussian. The result of the fit is shown in table 6.3.1. These are taken as the starting values in the final asymmetry fit to the full data sample.

Uncertainty of Δt, $\sigma_{\Delta t}$

As in other time-dependent analysis in *BABAR*, the signal and background Δt PDFs are normalized so that

$$\sum_{T=-1,+1} \int_{-\infty}^{\infty} P^c_{S,B}(\Delta t, T|\sigma_{\Delta t})\, d(\Delta t) = 1$$

for any value of $\sigma_{\Delta t}$. This normalization allows us to eliminate a PDF for $\sigma_{\Delta t}$ in the likelihood function. Figures 6.15 and 6.16 show the $\sigma_{\Delta t}$ distributions for signal MC and background data, events with $m_{\rm ES} < 5.27\,{\rm GeV}/c^2$, for different tagging categories. We use these two samples to parametrize $\sigma_{\Delta t}$ for Toy MC studies only. The distributions are parametrized by Landau functions.

The lepton category (Cat 1) for the background has only one event. Therefore we used the parameters from the full sample, not divided by tagging category. The results of these fits are shown in tables 6.3.1 and 6.3.1.

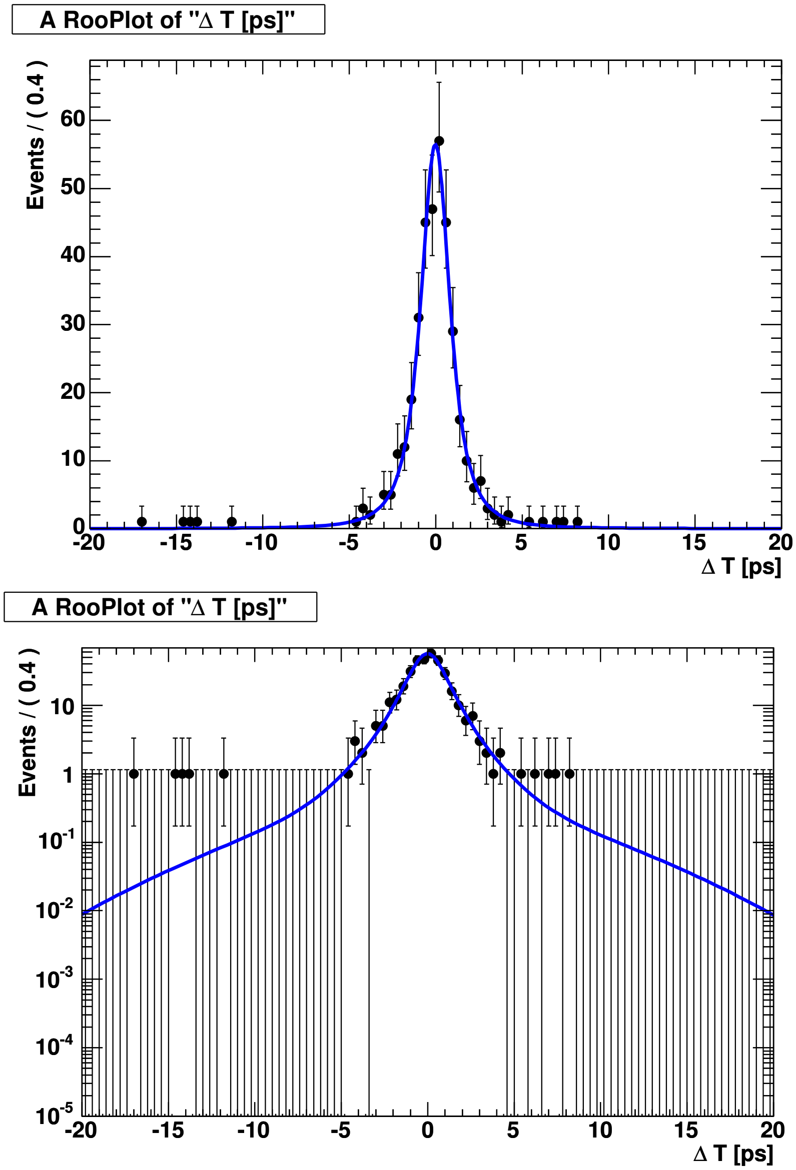

Figure 6.14: Background Δt fit; $m_{\mathrm{ES}} < 5.27\,\mathrm{GeV}/c^2$. Bottom plot is shown on a Log scale.

Table 6.5: List of parameters allowed to float in the final maximum likelihood fit for the CP asymmetry.

Parameter	Description
$C_{3K_S^0}$	
$S_{3K_S^0}$	
N_S	Number of signal $B^0 \to K_S^0 K_S^0 K_S^0$ candidates
N_B	Number of background $B^0 \to K_S^0 K_S^0 K_S^0$ candidates
ξ	Background $m_{\rm ES}$ Argus function parameter
P_1	Background $\Delta\ E$ parameter 1 of polynomial
P_2	Background $\Delta\ E$ parameter 2 of polynomial
$\mu_{\mathcal{F}}^{B}$	Background Fisher Bifurcated Gaussian mean
$\sigma_{\mathcal{F}}^{BL}$	Background Fisher Bifurcated Gaussian left sigma
$\sigma_{\mathcal{F}}^{BR}$	Background Fisher Bifurcated Gaussian right sigma
b_{core}	Background Δt core bias scale factor
b_{tail}	Background Δt tail bias scale factor
s_{core}	Background Δt core sigma scale factor
f_{tail}	Background Δt tail fraction ; σ fixed to 3ps
f_{out}	Background Δt outlier fraction; σ fixed to 8ps
$\Delta\epsilon_{Cat2}$	Background Category 2 tagging efficiency asymmetry
$\Delta\epsilon_{Cat3}$	Background Category 3 tagging efficiency asymmetry
$\Delta\epsilon_{Cat4}$	Background Category 4 tagging efficiency asymmetry
$\Delta\epsilon_{Cat5}$	Background Category 5 tagging efficiency asymmetry
$\Delta\epsilon_{Cat6}$	Background Category 6 tagging efficiency asymmetry
ϵ_{Cat2}	Background Category 2 tagging efficiency
ϵ_{Cat3}	Background Category 3 tagging efficiency
ϵ_{Cat4}	Background Category 4 tagging efficiency
ϵ_{Cat5}	Background Category 5 tagging efficiency
ϵ_{Cat6}	Background Category 6 tagging efficiency

Table 6.6: Description of m_{ES}, ΔE, and $\mathcal{F}$ parameters used in ML fit.

Parameter	PDF	Sample Used for Parameterization
Signal m_{ES}	Crystal Ball	Signal MC
Background m_{ES}	Argus	Data $\lvert\Delta E\rvert > 40\,\mathrm{MeV}$
Signal ΔE	Cruijff	Signal MC
Background ΔE	Polynomial 2	Data $m_{\mathrm{ES}} < 5.27\,\mathrm{GeV}/c$
Signal $\mathcal{F}$	Bifurcated Gaussian	Signal MC
Background $\mathcal{F}$	Bifurcated Gaussian	Data $m_{\mathrm{ES}} < 5.27\,\mathrm{GeV}/c$

Table 6.7: The tagging parameters and resolution function parameters used to fit the signal asymmetries. These values are determined from the B_{flav} data sample.

Category	ΔD	D	$\Delta\epsilon$	ϵ	b_{core}
Cat 1	0.0057 ± 0.0180	0.9364 ± 0.0094	0.0034 ± 0.0164	0.0875 ± 0.0012	-0.0481 ± 0.044
Cat 2	0.041 ± 0.0190	0.9001 ± 0.0101	-0.0287 ± 0.0156	0.1089 ± 0.0014	-0.103 ± 0.0428
Cat 3	0.0285 ± 0.0190	0.6916 ± 0.0111	-0.0025 ± 0.0139	0.1714 ± 0.0017	-0.1974 ± 0.0336
Cat 4	0.0018 ± 0.0227	0.5426 ± 0.0140	-0.0089 ± 0.0161	0.1358 ± 0.0016	-0.2154 ± 0.0355
Cat 5	-0.1246 ± 0.0225	0.3377 ± 0.0146	-0.0201 ± 0.016	0.1469 ± 0.0007	-0.2016 ± 0.0343
Cat 6	-0.0843 ± 0.0272	0.1821 ± 0.0183	0.0089 ± 0.0191	0.0992 ± 0.0012	-0.1514 ± 0.0413
No Tag					-0.2057 ± 0.0269

Table 6.8: Fit to background events with $m_{\mathrm{ES}} < 5.27\,\mathrm{GeV}/c^2$ for Δt parameters, efficiencies, and efficiency asymmetries.

Parameter	Value
b_{core}	-0.031 ± 0.089
s_{core}	1.244 ± 0.088
s_{tail}	3.000 FIXED
s_{out}	8.000 FIXED
f_{tail}	0.151 ± 0.053
f_{out}	0.025 ± 0.012
$\Delta\epsilon_{Cat1}$	0.00 FIXED
$\Delta\epsilon_{Cat2}$	0.00 ± 0.17
$\Delta\epsilon_{Cat3}$	-0.21 ± 0.13
$\Delta\epsilon_{Cat4}$	-0.02 ± 0.15
$\Delta\epsilon_{Cat5}$	-0.32 ± 0.14
$\Delta\epsilon_{Cat6}$	-0.25 ± 0.14
$\Delta\epsilon_{NoTag}$	-0.191 ± 0.084
b_{tail}	-0.15 ± 0.55
ϵ_{Cat1}	0.0027 ± 0.0027
ϵ_{Cat2}	0.098 ± 0.015
ϵ_{Cat3}	0.157 ± 0.019
ϵ_{Cat4}	0.117 ± 0.017
ϵ_{Cat5}	0.127 ± 0.017
ϵ_{Cat6}	0.130 ± 0.018

Table 6.9: Result of a fit of a Landau function to the $\sigma_{\Delta t}$ distribution of signal events.

Tagging Category	Mean	Sigma
Cat 1	0.520154±0.00888008	0.0996335±0.00428945
Cat 2	0.510544 ± 0.0064556	0.088499 ± 0.0031635
Cat 3	0.58153±0.00609403	0.103966±0.00314638
Cat 4	0.63924±0.00852728	0.130228±0.00440427
Cat 5	0.640253±0.00826417	0.132603±0.00439915
Cat 6	0.637382±0.0102729	0.124885±0.00545023
No Tag	0.705011±0.00729587	0.151718±0.00385095
All	0.61899±0.00314687	0.129692±0.00158326

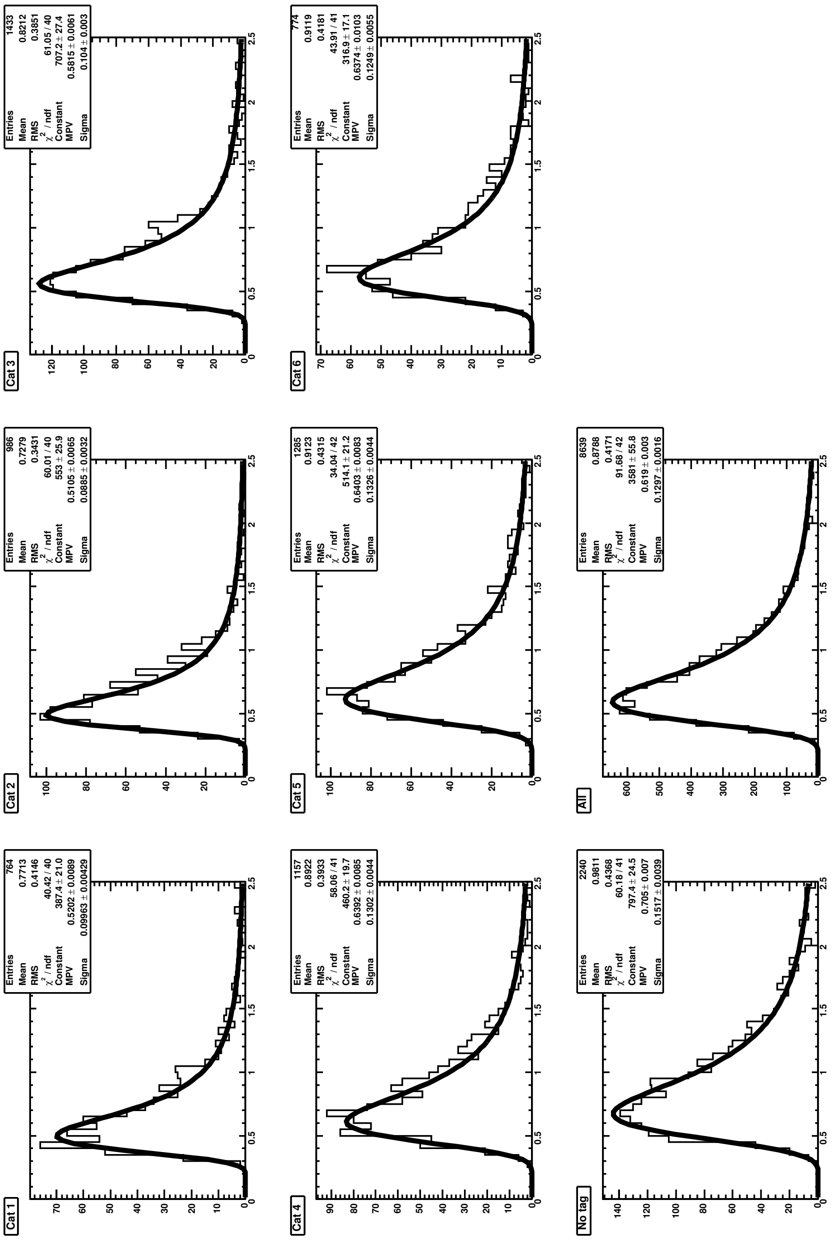

Figure 6.15: Signal MC $\sigma_{\Delta t}$ fit to Landau function.

Table 6.10: Result of a fit of a Landau function to the $\sigma_{\Delta t}$ distribution of background events ($m_{\mathrm{ES}} < 5.27\,\mathrm{GeV}/c^2$).

Tagging Category	Mean	Sigma
Cat 1 (fixed to ”All”)	0.621755±0.0151976	0.133652±0.00880798
Cat 2	0.493422±0.0409271	0.103145±0.0205992
Cat 3	0.628501±0.0555583	0.133057±0.0509737
Cat 4	0.649403±0.0480262	0.13302±0.0355151
Cat 5	0.6891±0.0981701	0.216665±0.0588089
Cat 6	0.649548±0.0501611	0.146863±0.0302051
No Tag	0.670903±0.0262448	0.137158±0.0144399
All	0.621755±0.0151976	0.133652±0.00880798

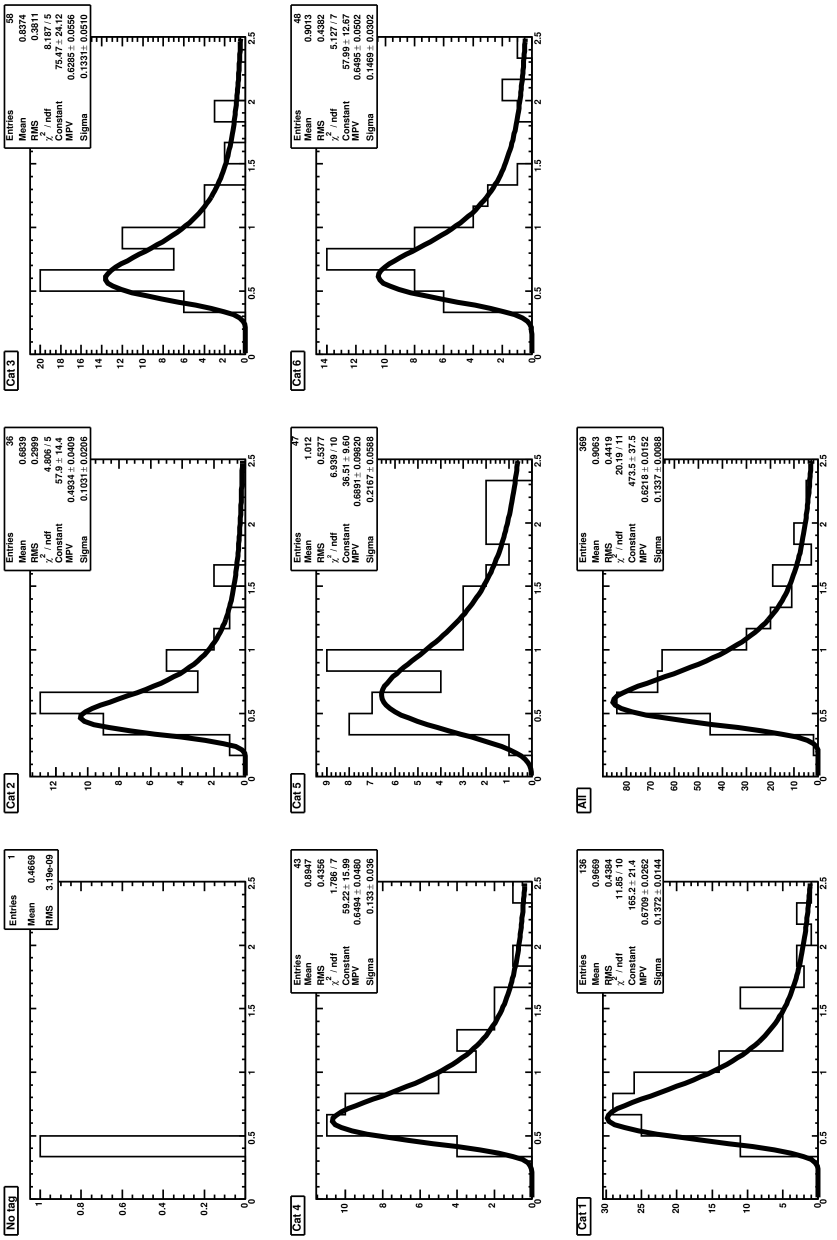

Figure 6.16: Background $\sigma_{\Delta t}$ fit to Landau function; $m_{\mathrm{ES}} < 5.27\,\mathrm{GeV}/c^2$ in data.

6.4 Toy MC Validations

Monte Carlo experiments are generated with parameters fitted from signal MC and the background data sample, $m_{\mathrm{ES}} < 5.27\,\mathrm{GeV}/c^2$. To test the sensitivity to the asymmetries we generate $S_{3K^0_S}$ and $C_{3K^0_S}$, randomly, in the physical region $S^2 + C^2 < 1$ and do some diagnostic checks. Signal and background yields are generated using Poisson distributions with signal and background parameters centered at the values we found in the Run1-4 fit ($N_{sig} = 89$ and $N_{bkg} = 439$). The $\sigma_{\Delta t}$ distributions used are shown in section 6.3.1. Figure 6.17 shows the fitted values of the asymmetries and the mean of the pull distributions as a function of the corresponding generated values. These results provide a quantitative measure of the linearity of the fit procedure. A linear fit to the correlation between generated and measured values for S and C have slopes within 2σ of unity. We use the observed correlation to correct the measured values of S and C.

The mean values for pull distributions all lie within 2σ of zero, while a fit with a straight line exhibits a slope consistent with zero. The standard deviations of the pull distribution shown in fig. 6.18 are typically slightly larger than one. We suspect this is due to some fraction of the fits giving unphysical results. This happens when the random values of S and C are close to unity. About 18% of fits lie in the unphysical region $S^2 + C^2 \geqq 1$ and 0.6% are unphysical and lie 3σ away from one, or are highly unphysical. The widths of the S and C pull distributions shown in fig. 6.19 for an ensemble of experiments generated with random physical values for S and C are larger than one as expected.

With a cut of $|S| < 1.15$ and $|C| < 1.15$ for the S pull and $|S| < 1.2$ and $|C| < 1.2$ for the C pull, the distributions have a mean which is one σ away from zero (see figure 6.20). Therefore our theory about the unphysical fits making the pulls larger is valid.

6.4.1 Validation of Fit on Embedded Toy Monte Carlo Experiments

We also do embedded Toy MC studies where a random subset of signal MC events is mixed with background events generated with the Toy MC technique. These studies are intended to show whether the correlations in the variables in the maximum likelihood fit bias our results. As we saw in section 6.2 m_{ES} and ΔE are the two variable with largest correlation.

Fits are performed to an ensemble of embedded Toy MC experiments with the correct proportion of background events observed in data. Table 6.4.1 shows the mean values and standard deviations from the ensembles generated with four different combinations of values for S and C.

We also do fits with the number of signal and background events set to the value obtained from a fit to the data. Likewise, fits are performed with the background fixed to zero. We compare the set of fits for the same random combination of signal MC events to determine whether the *CP* information is diluted by adding background. We see no evidence of any dilutions. The residuals of these fits are shown in Figs. 6.21 and 6.22.

Since we have a small sample of MC events, we run the risk of oversampling and amplifying slight biases after scaling to larger samples. If there is a small bias in the MC sample we will artificially make the bias larger if we reuse events selected randomly for these tests. We can overcome this by first fitting a large sample of MC events as shown earlier in table 6.4.1 to check that no bias is introduced from correlations in the signal events. Then by comparing samples with and without background events as was shown in figures 6.21 and 6.22 we can determine if the *CP* information is diluted by the addition of the background events.

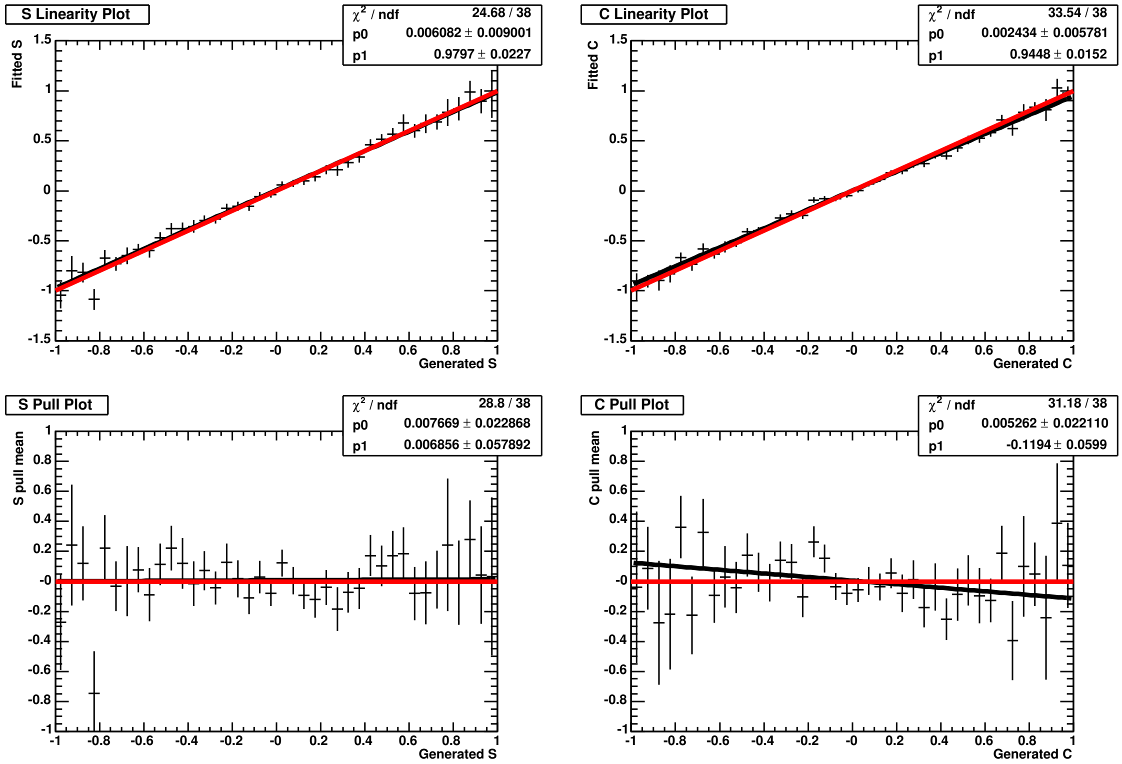

Figure 6.17: Fitted S and C versus their generated values in Toy Monte Carlo studies (first row). Mean of the pull distribution versus generated value in Toy Monte Carlo studies (second row). Pull is defined as $(x_{\text{fitted}} - x_{\text{generated}})/x_{\text{error}}$ where is x is the variable in question and x_{error} is the error on x determined from the fit. The red line is the expectation if the measured result from the fit agrees on average with the generated value and the black line is the result of a fit to a linear function of generated values.

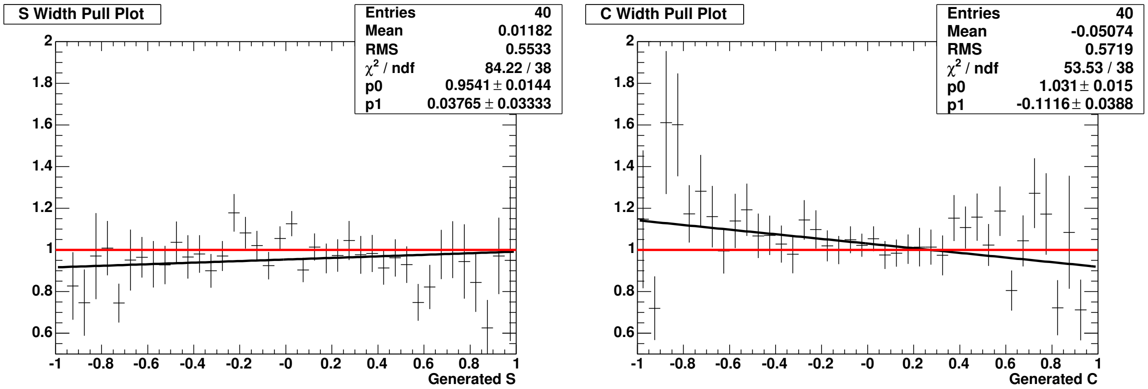

Figure 6.18: Standard deviation of the pull distribution for S and C from Toy Monte Carlo studies with a cut of $|S| < 1.1$ and $|C| < 1.1$. Pull is defined as $(x_{\text{fitted}} - x_{\text{generated}})/x_{\text{error}}$ where is x is the variable in question. The red line is the expectation if the errors from the fit are correct and the black line is the result of a fit to a linear function of generated value.

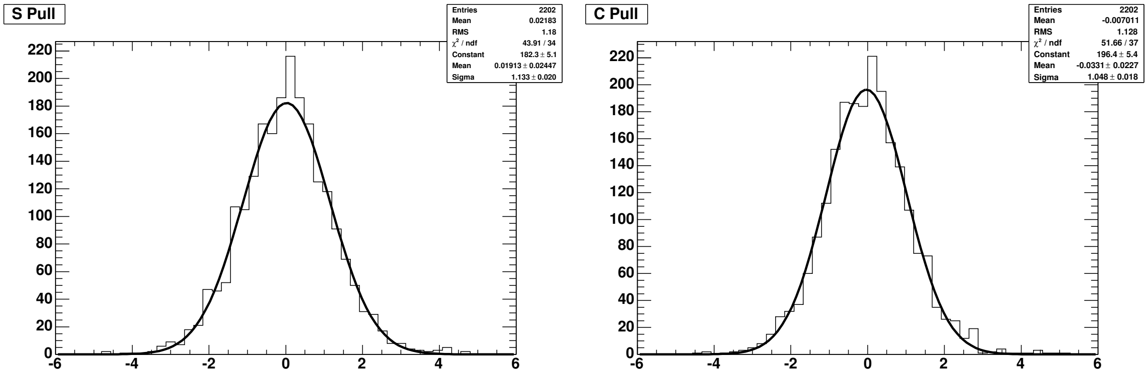

Figure 6.19: $S_{3K_S^0}$ and $C_{3K_S^0}$ pull distributions from Toy MC studies with random generated values for S and C.

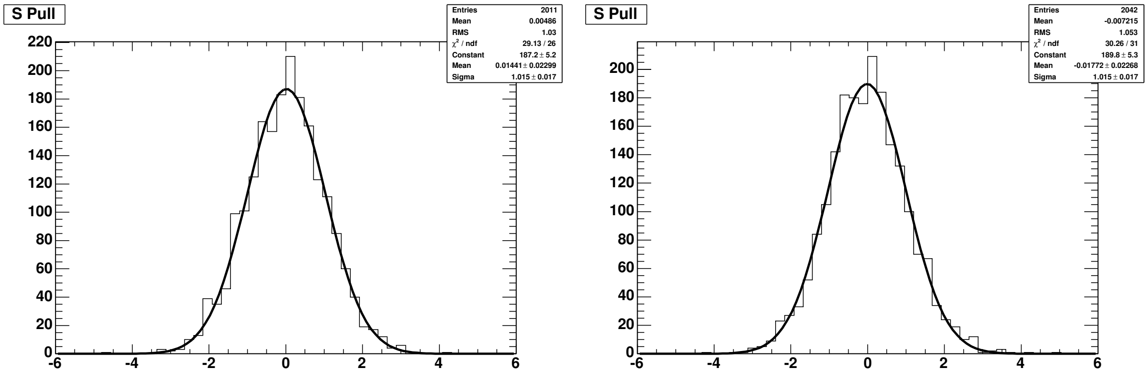

Figure 6.20: $S_{3K_S^0}$ and $C_{3K_S^0}$ pull distributions from Toy MC studies with a cut of $|S| < 1.15$ and $|C| < 1.15$ for the S pull and a cut of $|S| < 1.2$ and $|C| < 1.2$ for the C pull.

Table 6.11: Fits to ensembles of Toy MC generated background events embedded with full MC signal events for different values of S and C.

Parameter	$S = C = 0.0$	$S = 0.7 C = 0.0$	$S = 0.8 C = 0.2$	$S = 0.5 C = 0.5$
$C_{3K_S^0}$	0.0018 ± 0.0160	0.0025 ± 0.0203	0.1990 ± 0.0207	0.5169 ± 0.0190
$S_{3K_S^0}$	0.0366 ± 0.0237	0.7334 ± 0.0278	0.8012 ± 0.0279	0.5146 ± 0.0286

Table 6.12: Summary of mean residuals of $S_{3K_S^0}$ and $C_{3K_S^0}$; Difference between embedded Toy MC fits with and without background

Parameter	S=C=0.0	S=0.7 C=0.0	S=0.8 C=0.2	S=0.5 C=0.5
$\delta C_{3K_S^0}$	0.0004	0.0012	0.0041	-0.0007
$\delta S_{3K_S^0}$	-0.0066	-0.0038	-0.0161	-0.0097

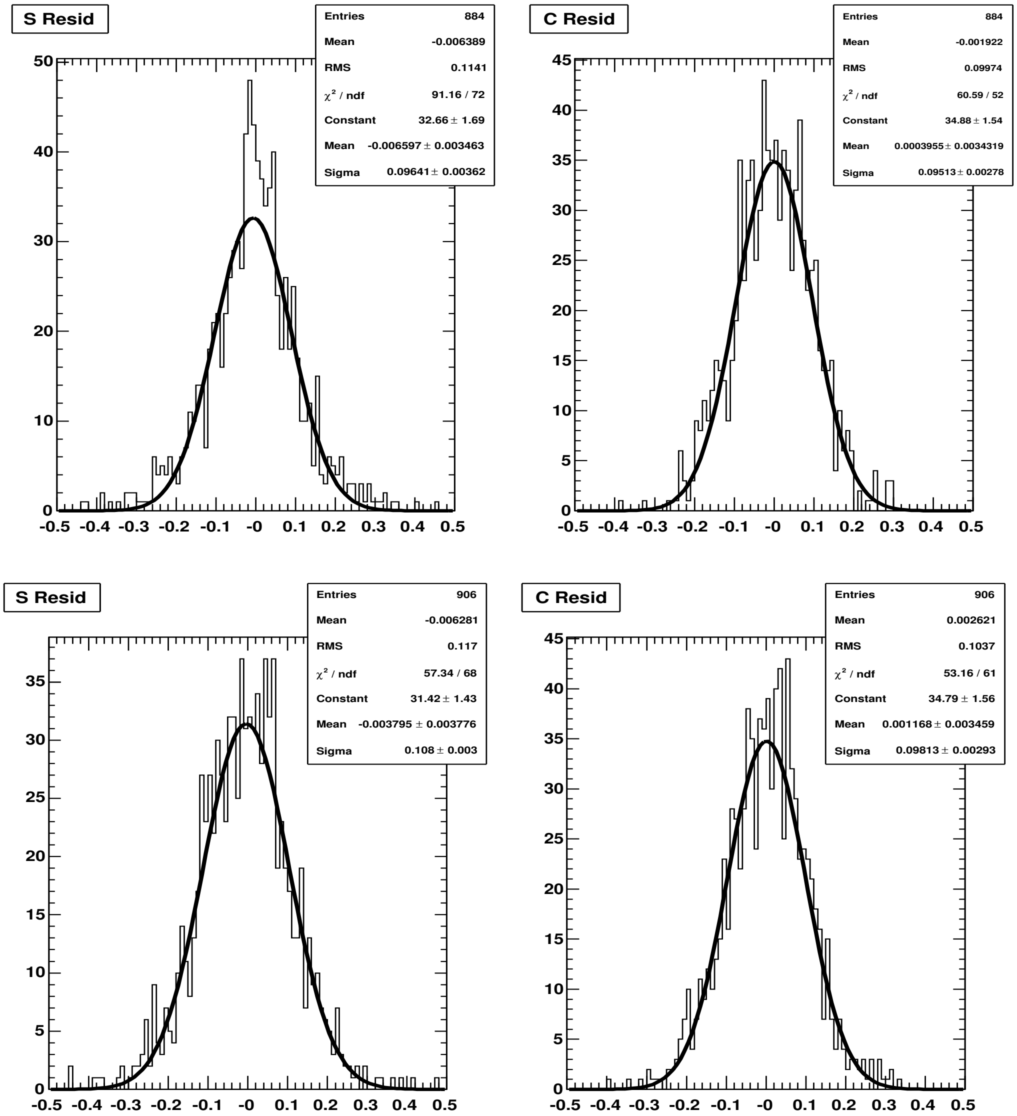

Figure 6.21: Residual distributions of $S_{3K_S^0}$ and $C_{3K_S^0}$; Difference between embedded Toy MC fits with and without background events. Generated value of S=0.7 and C=0.0 for first row and S=0.0 and C=0.0 for second row.

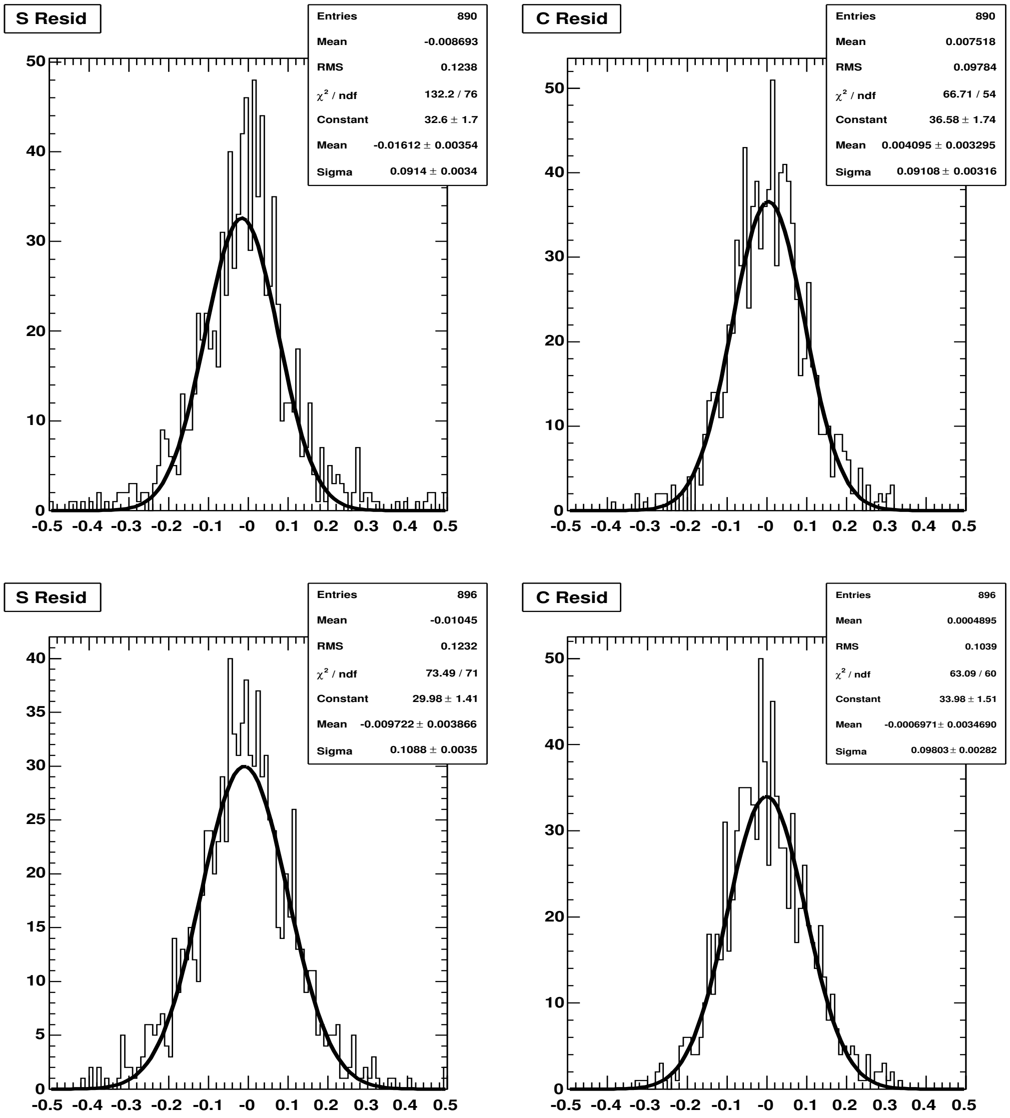

Figure 6.22: Residual distributions of $S_{3K_S^0}$ and $C_{3K_S^0}$; Difference between embedded Toy MC fits with and without background. Generated value of S=0.8 and C=0.2 for first row and S=0.5 and C=0.5 for second row.

6.4.2 Errors and Likelihoods from Toy Studies

Figure 6.23 shows the expected error on S and C from the MC toy studies. The mean value of the error distribution is 0.39 for $S_{3K_S^0}$ and 0.26 for $C_{3K_S^0}$. The arrows on the plots represent the error from the fit to our blinded data sample. We see that the value of the error is in good agreement with predictions from the Toy MC studies.

The distribution of the likelihood value itself is shown in Fig. 6.24. Again the arrow on the likelihood plot shows the value from the blind fit to data and it is again in good agreement with the Toy MC predictions. The agreement with Toy MC predictions serves as a loose goodness of fit test. It's argued that there is no good measure of the goodness of fit from likelihood fits, but these checks are done to determine if the deviation between the data and Toy MC fits are large. This would warn us if the fit is problematic.

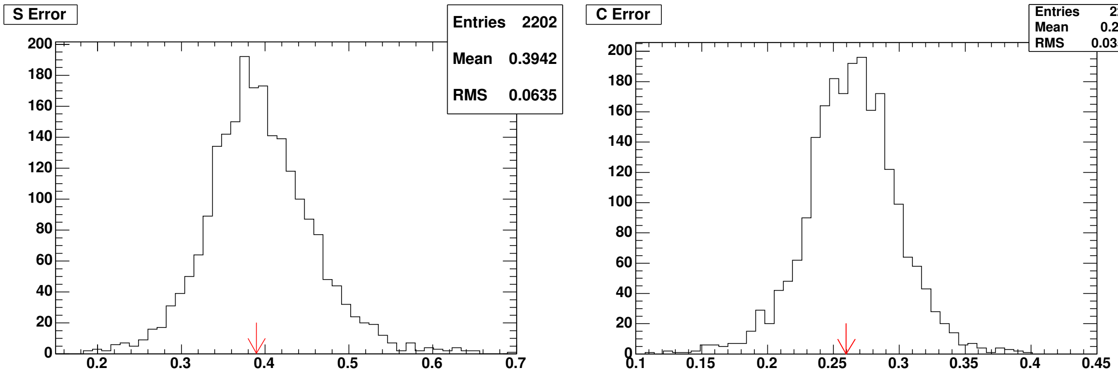

Figure 6.23: $S_{3K_S^0}$ and $C_{3K_S^0}$ error distributions from Toy MC studies. Arrows point to the error estimates obtained from the fit to the blinded data.

6.5 Results

Table 6.5 shows the full result of the likelihood fit to the data. Fig 6.25 shows distributions of Δt for B^0 tagged and $\overline{B}^0$ tagged events and the asymmetry $\mathcal{A}(\Delta t) = (N_{B^0} - N_{\overline{B}^0})/(N_{B^0} + N_{\overline{B}^0})$ obtained by making a likelihood ratio cut to remove the background component. This cut removes 96% of the background while retaining 95% of the signal. The curve is the fit result scaled to the number of signal and background events remaining after the likelihood ratio cut. The values of S,

C, and N_{sig} determined from the fit with asymmetric errors are

$$\begin{aligned} S &= -0.71^{+0.38}_{-0.32} \\ C &= -0.34^{+0.28}_{-0.25} \\ N_{\text{sig}} &= 86.7^{+10.5}_{-9.8}. \end{aligned}$$

Fixing $C = 0$, which is the Standard Model expectation, we obtain $\sin 2\beta_{\text{eff}} = -S = 0.79^{+0.29}_{-0.36}$.

Figure 6.26 shows the maximum likelihood value as a function of S and C. This shows that our results are indeed the minimum of the likelihood function as expected.

The distribution of per event weights and event weights versus Δt are shown in fig. 6.27. The event weight is the log likelihood contribution for the individual event. We see that the events with a large -log likelihood are ones with large Δt in data. This trend is also observed in Toy MC events, as shown in 6.28. The Toy MC results are obtained by generating a sample 20 times larger than data, but with the observed ratio of background to signal. An overlay of the data and Toy MC events also shows good agreement. This is shown in fig. 6.29 and gives us confidence in our modeling of data events.

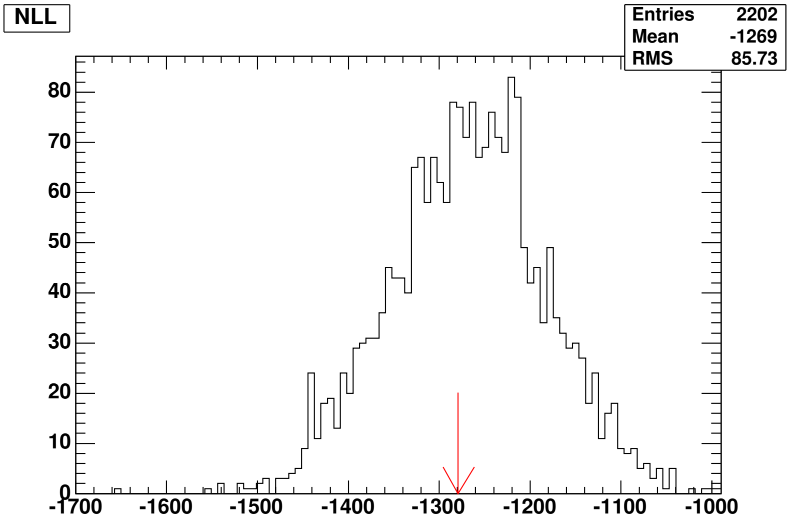

Figure 6.24: Log(likelihood) distribution from Toy MC studies. Arrow points to result from blind fit.

6.5.1 $_sPlots$

Figures 6.30- 6.33 show $_sPlots$ of m_{ES}, ΔE, $\mathcal{F}$, and Δt [31]. These figures are made by first omitting the projection variable, the variable being plotted, and fitting the remaining variables, to estimate signal and background yields. For each event, a weight to be signal or background is derived according to these fit results and the probability distributions in the restricted set of variables. Using these weights, the data is then plotted in the projection variable. The curves show the results of the fit to the restricted set of variables for comparison. Note that the final results are based on a fit to all

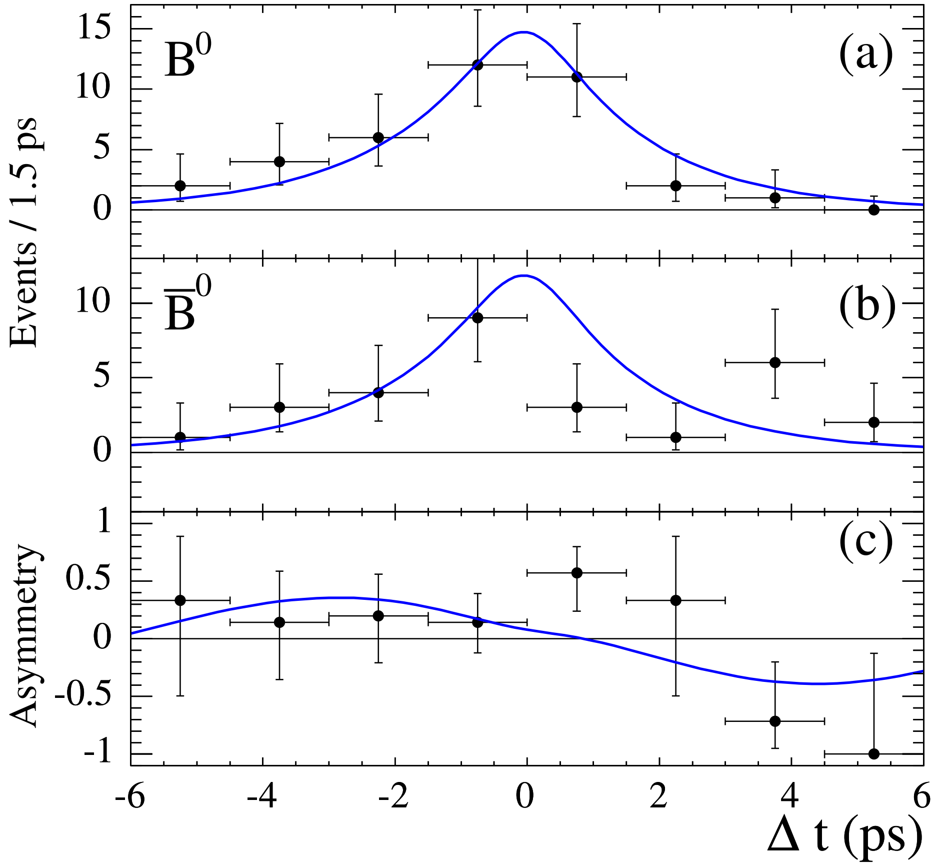

Figure 6.25: Distributions of Δt for background subtracted events for B_{tag} tagged as (a) B^0 or (b) $\overline{B}^0$, and (c) the asymmetry $\mathcal{A}(\Delta t)$. We use a likelihood ratio cut that removes 96% of the background while retaining 95% of the signal. The curve is the scaled fit result.

6.6 Systematic Uncertainties and Cross Checks

The errors on this measurement are expected to be dominated by the statistical error, but the systematic error must be determined and cross checks on the data must be performed to insure consistency in the data sample. Section 6.6.1 explains and shows estimates of the sources of systematic uncertainties on S and C. Section 6.6.2 shows the list of cross checks performed on the data sample.

6.6.1 Systematic Uncertainties

This section details the systematic uncertainties on the asymmetries S and C which are listed in table 6.14. The main source of uncertainty arises from the PDF uncertainty. The uncertainty on the PDF parameters arises from the error from the fit to the data sample. In general to determine the uncertainty on S and C data is refit changing a parameter in the fit. Other ways to estimate an uncertainty is to use MC control samples as is done for the SVT alignment and tag side interference

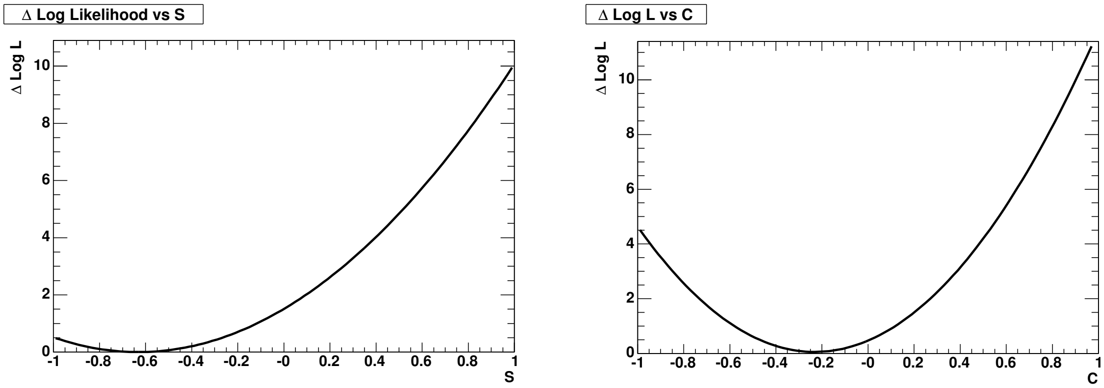

Figure 6.26: Δ Likelihood functions for S and C from fit to data.

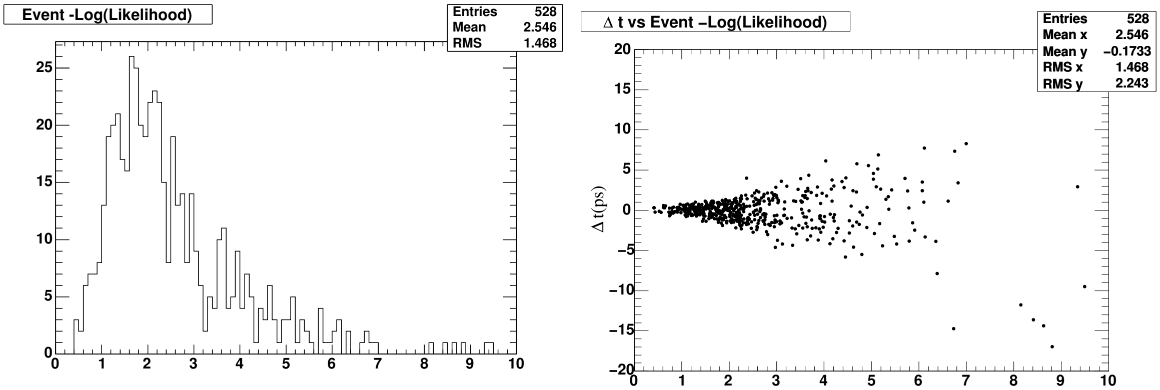

Figure 6.27: Distribution of -log(likelihood) and correlation between -log(likelihood) and Δt for data events.

systematic uncertainties. Also any fit bias determined from the Toy MC events is added as a systematic uncertainty. Other systematic uncertainties are determined by a comparison of signal and MC events as for the vertexing method and the Δt resolution function uncertainties. There is no well defined procedure for determining sources of systematic uncertainties, therefore potential sources of uncertainties have to be considered and tested.

Systematic Uncertainties from PDF parametrization

Tables A- A in Appendix A provide a detailed account of the estimated systematic uncertainties from varying the signal PDF parameters in the fit by their error. These errors are mostly statistical in nature. The exceptions are Δm and τ_{B^0} whose values are varied by their error in the PDG [13]. The PDF systematics are summarized in table 6.14 lines 1-7 of the PDF section, the top portion separated

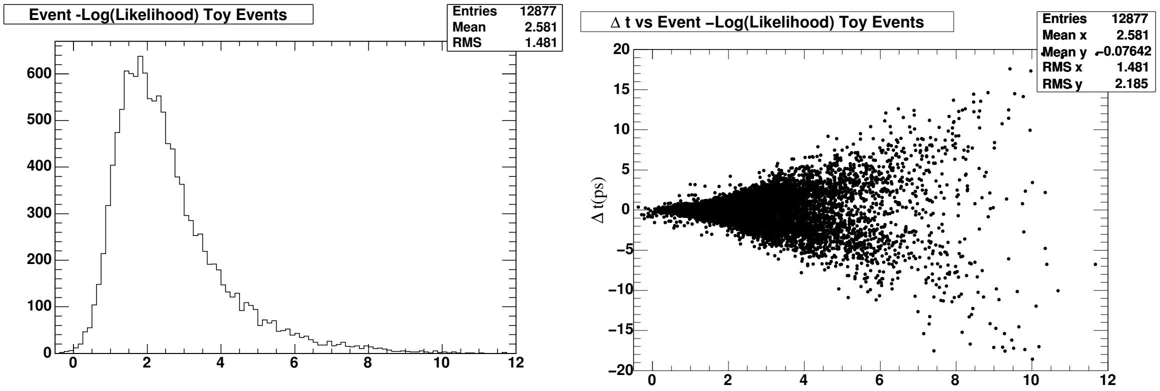

Figure 6.28: Distribution of -log(likelihood) and correlation between -log(likelihood) and Δt for a Toy MC sample of events.

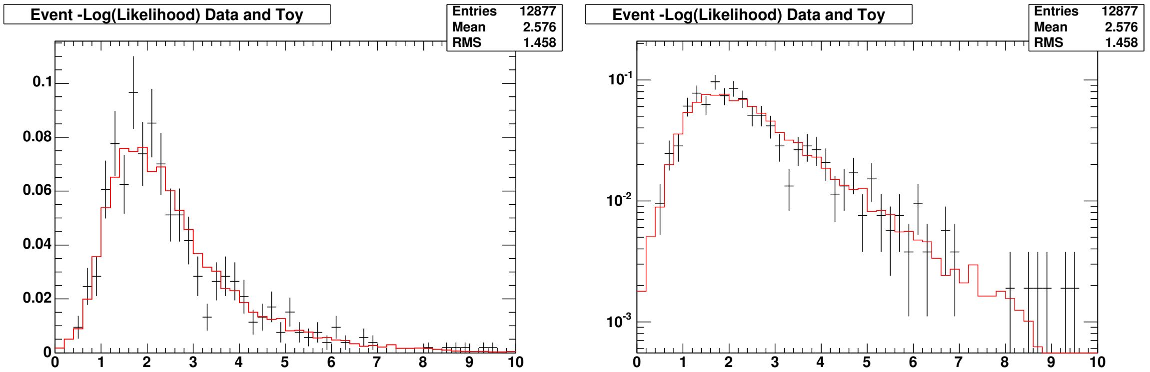

Figure 6.29: Distribution of -log(likelihood) for data events (points with error bars) and Toy MC (overlaid histogram) on a linear (left) and log scale (right).

by horizontal line. The systematic uncertainty, ΔS or ΔC, is estimated from the difference between the nominal fit and the fit where the PDF parameter in question is varied up and down by the error. The sign of ΔS or ΔC is shown in the table. If both values are positive (negative), the greater (lesser) of the two is taken for the +(-) category and the -(+) category is set to zero. The other systematics in the PDF category are obtained from floating $\mu^S_{m_{\rm ES}}$ and $\mu^S_{\Delta E}$ to make sure the MC values are similar to data values and therefore do not bias our results on S and C. The total sum for the PDF systematics are 0.0254 for S and 0.0263 for C.

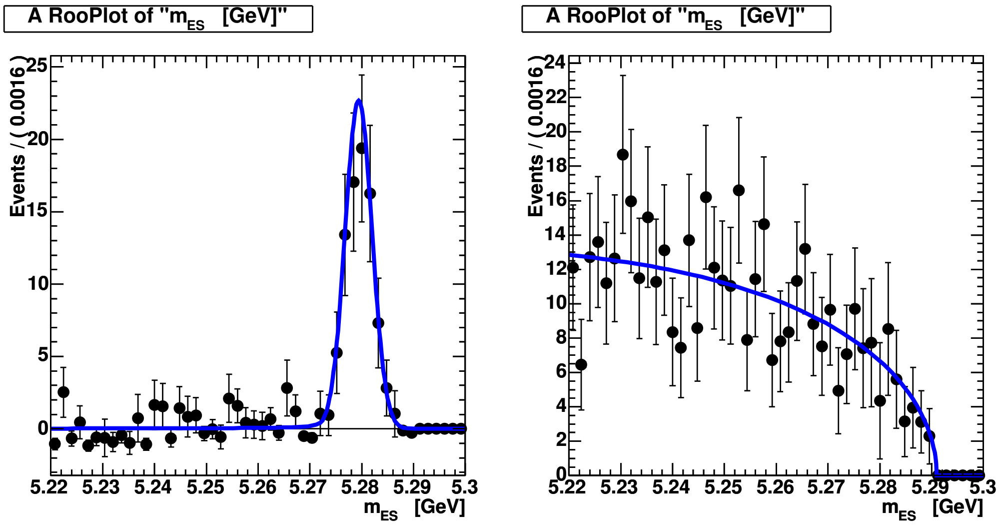

Figure 6.30: ${}_s$Plot of signal (left) and background (right) $m_{\rm ES}$.

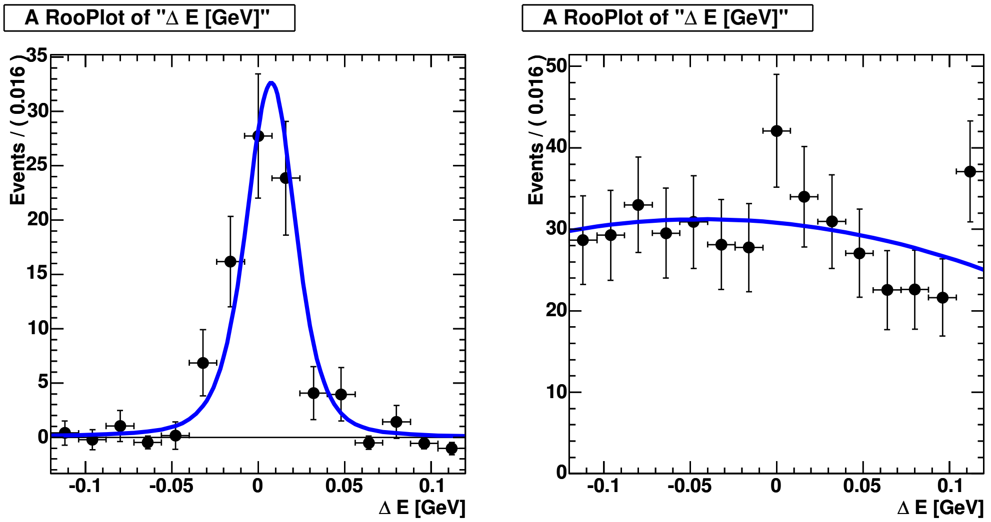

Figure 6.31: ${}_s$Plot of signal (left) and background (right) ΔE.

SVT Alignment and Boost Uncertainties

We rely on the precision of the SVT for reconstructing decay vertices and for tracking charged particles in the detector. The precision of determining the position of a charged particle in the SVT however is only as good as our knowledge of the relative position of the silicon wafers. Determining the position of the wafers and strips relative to their nominal position is known as the *local SVT alignment*.

The internal alignment of SVT wafers is determined by comparing measured versus projected

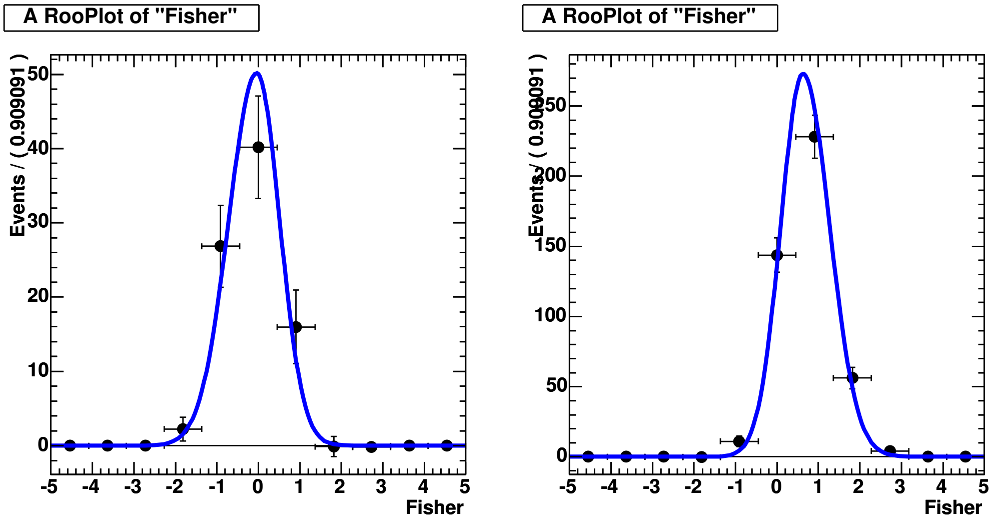

Figure 6.32: $_s$Plot of signal (left) and background (right) $\mathcal{F}$.

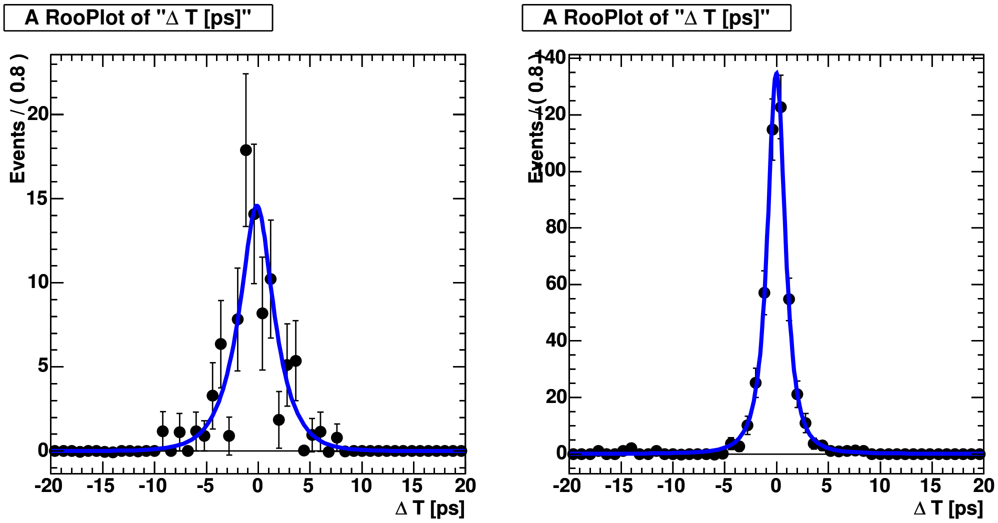

Figure 6.33: $_s$Plot of signal (left) and background (right) Δt.

positions of tracks obtained from the process $e^+e^- \to \mu^+\mu^-$ for studying the parameters d_0, z_0, and ϕ_0 defined in section 3.4.1. The position of the wafers is expressed in terms of a rotation and translation with respect to the nominal alignment.

Systematic uncertainties from residual uncertainties in the SVT local alignment are determined from simulated MC events. Several *misalignment scenarios* are introduced in the reconstruction of the MC, which is normally reconstructed with the nominal alignment, to determine systematic effects.

We also take into account the uncertainty of the radius-dependent z shift of entire layers which is equivalent to having an uncertainty in the boost, $\beta\gamma$. This uncertainty is computed from MC events in the same fashion as the SVT misalignments.

We fit a Monte Carlo sample reconstructed in *refit mode* with four different misalignment scenarios and one boost uncertainty file [32]. Refit mode means the tracks are refit, or reconstructed again, instead of being taken from a stored nominal reconstruction in the database called *cache mode*. We also reconstruct events without misalignment in the refit mode to make sure any differences are not coming from the reconstruction method.

For each misalignment scenario we compare the sample without misalignment ('nominal') with the sample with misalignment. To reduce the impact of statistical fluctuations due to events entering or leaving the selection, we select only events that are common in the nominal and the misaligned sample. The errors are added in quadrature for the total systematic uncertainty. The variation if S and C for each misalignment file and the total systematic uncertainty are shown in table 6.6.1.

Vertexing and Resolution Function

To determine if there is a difference in our vertexing method versus the nominal vertexing method used by most other time dependent analyses at *BABAR*, we fit our MC sample with the resolution function parameters taken from $B^0 \to K^0_S K^0_S K^0_S$ MC and D_c, ΔD_c, μ_c, and ϵ_c taken from the MC B_{flav} sample. The difference between this fit and the nominal fit, with all parameters taken from the $B^0 \to K^0_S K^0_S K^0_S$, is assigned as the systematic error. This is done on a MC sample with $S = 0.8$ and $C = 0.2$. We find a variation of 0.020 for S and 0.022 for C.

To determine a systematic error on the resolution function, we first compare the resolution functions of $B^0 \to K^0_S K^0_S K^0_S$ MC to the B_{flav} MC values and determine scale and offsets differences. We then scale or shift the B_{flav} data resolution function values according to the differences seen between the two MC samples. The bias values are shifted and the other parameters, σ_{core}, f_{out}, and f_{tail} are scaled. The difference in S and C from the nominal fit in data is taken as a systematic error. These values are 0.017 for both S and C.

Background Tagging Asymmetry

We set the background tagging asymmetry parameters to zero since in the fit we see that most tagging categories have values which are consistent with zero. It is likely that their deviation from zero is just a statistical fluctuation. There is also no mechanism where an asymmetry in the background could be produced so we expect those values to be zero. This gives an uncertainty in S of 0.007 and in C of 0.022.

Embedded Toy MC Bias/Correlations in Fit Parameter

Correlations in the fit parameters would effect signal and background yields and therefore vary the values of S and C. We assign a systematic error for the correlation between the fit parameters by taking the largest residual from Table 6.4.1. This table shows the mean of the residuals of S and C when fitting signal MC events only and when adding generated background events. These residuals are a measure of uncertainty of S and C from correlations. For C the largest residual is 0.004 and for S it's 0.016.

Tag Side Interference

Interference between CKM-favored $b \to c\overline{u}d$ and doubly-CKM suppressed $\overline{b} \to \overline{u}c\overline{d}$ amplitudes in final states used for B flavor tagging gives deviations from the standard time evolution assumed in *CP* violation measurements [33]. For example a tag B meson may be observed in the $D^+\pi^-$ mode and generate a K^- tag from the D^+. The dominant amplitude contribution is from the $\overline{B}^0$ decay ($b \to c\overline{u}d$), but a suppressed amplitude from the B^0 decay ($\overline{b} \to \overline{u}c\overline{d}$) cannot be ruled out. These two amplitudes will interfere with a relative weak phase of γ and a relative strong phase of δ' from final-state interactions. A rough estimate of the relative size of these amplitudes is $r' \sim |V_{ub}^* V_{cd}/V_{cb}V_{ud}^*| = 0.02$. Events which decay semileptonically are immune to this effect.

Using equation (31) and (32) in [33]:

$$\begin{aligned}\mathcal{C}_{\text{fit}} &= \mathcal{C}_0[1 + 2r' \cos\delta' \mathcal{G}\cos(2\beta+\gamma) - \mathcal{S}_0\sin(2\beta+\gamma)] - 2r' \sin\delta' \mathcal{S}_0\cos(2\beta+\gamma) \\ &\qquad + \mathcal{G}\sin(2\beta+\gamma) \qquad (6.5)\\ \mathcal{S}_{\text{fit}} &= \mathcal{S}_0[1 + 2r' \cos\delta' \mathcal{G}\cos(2\beta+\gamma)] + 2r' \sin\delta' \mathcal{C}_0\cos(2\beta+\gamma) \qquad (6.6)\end{aligned}$$

where $\mathcal{G} \equiv 2\text{Re}\lambda_C P/(|\lambda_C P|^2 + 1)$ which in the standard model would give $\mathcal{G} \equiv -\cos(2\beta)$ since $\lambda = -e^{2i\beta}$, we can determine the deviation of S and C from the nominal value. We generate values of $\gamma[39^\circ, 80^\circ]$, $\delta'[0, 2\pi]$, and $r'[0.00, 0.04]$, and $2\beta = 47.7^\circ$ and determine the one sigma deviation of the $\mathcal{C}_{\text{fit}}$ and $\mathcal{S}_{\text{fit}}$ distributions which we define as δC and δS respectively. We can then use the relation:

$$\delta S_{DCSD} = \sum_i \epsilon_{NSL,i} \frac{D_{NSL,i}}{\langle D_i \rangle} Q_i \delta S \tag{6.7}$$

$$\delta C_{DCSD} = \sum_i \epsilon_{NSL,i} \frac{D_{NSL,i}}{\langle D_i \rangle} Q_i \delta C \tag{6.8}$$

where $\epsilon_{NSL,i}$ and $D_{NSL,i}$ are the efficiency and dilutions respectively of events which decayed non-semileptonically at the MC truth level and $\langle D_i \rangle$ and Q_i are the average dilutions and quality factor respectively for all events for tagging category i. The value of $\sum_i \epsilon_{NSL,i} \frac{D_{NSL,i}}{\langle D_i \rangle} Q_i = 0.4965$. We then input the values of S and C that are determined from our fit and vary them by one sigma. The values which give the largest deviations are taken as the systematic uncertainty. The uncertainty on S is determined to be 0.008 and for C to be 0.015.

6.6.2 Cross Checks

To insure consistency of the data sample we perform the cross checks which are shown in this section.

Floating B^0 Lifetime

In the nominal fit the B^0 lifetime is fixed to 1.537 ± 0.015 [13]. Redoing the nominal fit for extracting S and C and floating B^0 lifetime gives $\tau_{B^0} = 1.771 \pm 0.231$ which is consistent with the world average which is used in the nominal fit. The values of S and C change by +0.022 and -0.016 respectively from the nominal value, however these numbers are just quoted to access the impact on the asymmetries and are not used as systematic errors.

Splitting Runs 1-3 and Run4

In order to check the consistency of subsamples of the full data set, we compare fits to run 1-3 versus run4. Given the limited background statistics in the subsamples, we are unable to determine background parameters independently. Instead we fix all fit variables to the values taken from the full sample with the exception of yields and the C and S time-dependent coefficients. Table 6.6.2 shows the blind results, since these checks were done before unblinding our results, on the asymmetries, the yields, purity, $\mathrm{N_{sig}/N_{bkg}}$, and the deviations of S and C in the subsamples from the full run 1-4 fit. The purity is calculated by Purity=$N_{\text{sig}}/\sigma(N_{\text{sig}})^2$. We see that the asymmetries and yields are consistent across the samples.

BC Vertexing Method Versus TreeFitter

In order to determine if the TreeFitter method has the same performance as the BC vertexing method which was tested in great detail in the $B^0 \to K^0_S\, \pi^0$ analysis, we fit signal MC events using Δt and $\sigma_{\Delta t}$ from the BC vertex method. This test will validate that the two methods are similar and there are no unexpected biases between the two. Table 6.6.2 shows fits to two MC samples with and without an asymmetry. We see slight variations in the measured values of S and C which are within statistics of the sample. The same events are used in the fit with different vertexing methods to avoid any statistical fluctuations in the central value.

B Background

A study has been performed where an additional uncorrelated B background component is added to the background sample. From our study of $B\overline{B}$ MC events, we demonstrated that most of the B background is evenly distributed in $m_{\rm ES}$ and ΔE. Enlarging the B background component three-fold from the expected level of 4 events we find that when the additional events have zero lifetime, the change in S is negligible while C changes by 0.004. With a non-zero lifetime the change in S and C are negligible since it does not pick up any B background component from this fit. These events are absorbed in the continuum background component. We conclude that the effect of an additional background component is negligible.

Branching Fraction Check

Using our measured signal yield we estimate a branching fraction (BF) of (6.8 ± 0.8)x10^{-6} for $B^0 \to K^0_S K^0_S K^0_S$. Note that this yield is after Δt and $\sigma_{\Delta t}$ selection requirements described in section 6.3. We've quoted a BF just as a consistency check with the BF analysis. This result is consistent with the BF analysis measurement of $(6.9 \pm 0.8 \pm 0.8)$x10^{-6} [34]. The slight deviations come from possible data/MC differences in efficiency when making selection requirements on Δt and $\sigma_{\Delta t}$.

Table 6.13: Result of fit to full dataset showing values of all parameters floated in the fit.

Parameter	Value
N_B	441.3 ± 21.4
N_S	86.7 ± 10.1
P_1	-0.649 ± 0.657
P_2	-7.43 ± 9.91
b_{core}	-0.0305 ± 0.0778
s_{core}	1.1801 ± 0.0758
f_{out}	0.0205 ± 0.0104
f_{tail}	0.1578 ± 0.0461
μ_{Cat2}	0.03 ± 0.149
μ_{Cat3}	-0.171 ± 0.124
μ_{Cat4}	-0.015 ± 0.145
μ_{Cat5}	-0.259 ± 0.121
μ_{Cat6}	-0.242 ± 0.131
b_{tail}	0.007 ± 0.471
$\mu_{\mathcal{F}}^{B}$	0.6253 ± 0.0678
$\sigma_{\mathcal{F}}^{BL}$	0.5327 ± 0.0441
$\sigma_{\mathcal{F}}^{BR}$	0.6446 ± 0.0445
ξ	-11.47 ± 6.99
ϵ_{Cat2}	0.1044 ± 0.0148
ϵ_{Cat3}	0.1482 ± 0.0172
ϵ_{Cat4}	0.1106 ± 0.0152
ϵ_{Cat5}	0.1468 ± 0.017
ϵ_{Cat6}	0.1271 ± 0.016
$C_{3K_S^0}$	-0.338 ± 0.265
$S_{3K_S^0}$	-0.707± 0.362

Table 6.14: Breakdown of all contributions to the systematic uncertainty on S and C.

	ΔS		ΔC	
	$(+)$	$(-)$	$(+)$	$(-)$
m_{ES} PDf	0.0021	0.0038	0.0009	0.0010
ΔE PDF	0.0008	0.0034	0.0017	0.0019
$\mathcal{F}$ PDF	0.0032	0.0057	0.0017	0.0024
resolution function	0.0097	0.0128	0.0061	0.0060
D and ΔD	0.0105	0.0150	0.0080	0.0082
ϵ_{tag}	0.0003	0.0034	0.0002	0.0008
$\Delta\epsilon^{S}$	0.0042	0.0080	0.0090	0.0095
$\mu^{S}_{m_{\mathrm{ES}}}$ float	0.0001	0.0001	0.0000	0.0000
$\mu^{S}_{\Delta E}$ float	0.0087	0.0087	0.0020	0.0020
PDF total	0.0254		0.0263	
SVT Alignment	0.015		0.008	
data/MC RF	0.017		0.017	
vertexing method	0.020		0.022	
$\Delta\epsilon^{B} = 0$	0.007		0.022	
Embedded fit bias	0.016		0.004	
tag side interference	0.008		0.015	
Total	0.043		0.047	

Table 6.15: Effects of SVT misalignment scenarios on measurements of S and C for about 120k MC events. The total systematic error is determined by adding in quadrature the boost misalignment to the largest value from the time misalignments.

Misalignment	ΔS	ΔC
Time1	-0.0144	0.0004
Time2	-0.0096	0.0073
Time3	-0.0103	0.0012
Time4	-0.0133	0.0016
Boost	-0.0023	0.0016
Total sys	0.0146	0.0075

Table 6.16: Summary of yields and blind asymmetries in data subsamples versus the nominal fit.

Parameter	Run1-4	Run 1-3	Run 4
$S_3K_S^0$	-1.158 ± 0.362	-1.107 ± 0.428	-1.561 ± 0.874
$\delta S_{3K_S^0}$		$+0.051$	-0.403
$C_3K_S^0$	-0.790 ± 0.265	-0.648 ± 0.367	-0.953 ± 0.345
$\delta C_{3K_S^0}$		$+0.142$	-0.163
$\mathrm{N_{sig}}$	86.7 ± 10.1	52.0 ± 7.7	34.6 ± 6.4
$\mathrm{N_{bkg}}$	441.3 ± 21.4	259.0 ± 16.3	182.4 ± 13.7
Purity	85.0%	87.7%	84.5%
$\mathrm{N_{sig}}/\mathrm{N_{bkg}}$	19.6%	20.1%	19.0%

Table 6.17: Comparison of fit results with signal MC events using the BC and TreeFitter vertexing methods

Vertexing Method	$S = C = 0.5$		$S = C = 0.0$	
	S	C	S	C
TreeFitter	0.515 ± 0.021	0.499 ± 0.014	0.014 ± 0.017	0.015 ± 0.011
BC	0.525 ± 0.021	0.497 ± 0.014	0.014 ± 0.017	0.014 ± 0.011

Chapter 7

Conclusions

With a data sample of 205 fb^{-1} amounting to 227 million $\Upsilon(4S) \to B\,\overline{B}$ decays we measure CP-violating asymmetries in $B^0 \to K_S^0\,K_S^0\,K_S^0$ decays

$$\begin{aligned} S_{3K_S^0} &= -0.71^{+0.38}_{-0.32} \pm 0.04 \\ C_{3K_S^0} &= -0.34^{+0.28}_{-0.25} \pm 0.05 \end{aligned}$$

with 87 ± 10 signal events where the decays of $K_S^0 \to \pi^+\,\pi^-$ are only considered. This result is published in Phys. Rev. Lett. [34]. Fixing $C = 0$, which is the Standard Model expectation, we obtain $\sin 2\beta_{3K_S^0} = -S = 0.79^{+0.29}_{-0.36} \pm 0.04$.

7.1 Significance of Result

In section 2.5 we showed that the $B^0 \to K_S^0\,K_S^0\,K_S^0$ decay is a penguin mode which has a theoretically reliable predicted *CP* asymmetry within the Standard Model, similar to $B^0 \to \phi K_S^0$. The penguin decays are an important experimental probe of new physics beyond the Standard Model. As shown before a deviation of the $\sin 2\beta_{3K_S^0}$ from $\sin 2\beta_{J/\psi\,K_S^0}$ would be an evidence of new physics; however, our result is quite consistent with SM prediction.

Around the same time the Belle collaboration has also made a measurement of these asymmetries: $S_{3K_S^0} = 1.26 \pm 0.68 \pm 0.20$ and $C_{3K_S^0} = -0.54 \pm 0.34 \pm 0.09$ [35]. The Belle Collaboration has much worse uncertainties since their vertexing efficiency and Δt resolution are much worse than *BABAR*'s. The Belle result also includes decays where one $K_S^0 \to \pi^0\,\pi^0$. In a sample of 275 million $\Upsilon(4S) \to B\,\overline{B}$ pairs they have 88 ± 13 signal events, therefore they also suffer from lower K_S^0 efficiency. This measurement is 2.9σ away from the SM prediction but their uncertainties are quite large [35]. The average of the two measurements gave a central value on S of -0.26 ± 0.34 [36] which is about 1.3σ away from $\sin 2\beta_{J/\psi\, K^0_S}$.

At the Lepton-Photon Conference which took place in summer of 2005, Belle updated their results with 386 million $\Upsilon(4S) \rightarrow B\ \overline{B}$ pairs to $S = -0.58 \pm 0.36 \pm 0.08$ and $C = -0.50 \pm 0.23 \pm 0.06$ with 105 ± 12 signal events [6] [37]. This preliminary measurement has a much better statistical error which we presume comes from the new silicon vertex tracker installed at Belle since the additional signal events cannot improve the statistical error about a factor of two. The central value of S has moved much closer to our result making the two measurements consistent with each other and also with SM predictions.

7.2 Comparison with other Penguin and Charmonium Decays

As seen from fig. 7.1 our result is consistent with both the average from charmonium decays and the penguin decays. The decay $B^0 \rightarrow K^0_S\, K^0_S\, K^0_S$ has advantage over decays where the *CP* content is not well understood. It is purely *CP* even whereas other measurements can have a mixture of *CP* even and *CP* odd making it more difficult to interpret results. We also saw in section 2.5 that the SM prediction for $S_{3K^0_S}$ differs from $S_{J/\psi\, K^0_S}$ by $\Delta S_{3K^0_S}$ = 0.02 when applying the QCD factorization model [19]. If the measurement of $S_{3K^0_S}$ is very different from $S_{J/\psi\, K^0_S}$ this could be evidence for a new physics phenomenon.

Fig. 7.2 [38] shows the theoretical expectations from QCD factorization for each penguin decay mode. We see with the exception of the $B^0 \rightarrow K^0_S\, K^0_S\, K^0_S$ decay the predictions make $\Delta \sin 2\beta = \sin 2\beta_{\text{eff}} - \sin 2\beta_{J/\psi\, K^0_S} > 0$ for all other modes. However from figs. 7.1 and 7.3 we see that most measurements yield $\Delta \sin 2\beta_{\text{meas}} = \sin 2\beta_{\text{meas}} - \sin 2\beta_{J/\psi\, K^0_S} < 0$ and the average from penguin modes, shown as a yellow band, in fig. 7.1 also shows this trend. The opposite sign of the measured versus expected deviation could be the first hint of new physics in the penguin decays.

Some argue a naive average of the penguin modes can lead to incorrect conclusions since each mode suffers from a different predicted theoretical uncertainty. Performing a χ^2 for each mode from the predicted theoretical value is a preferred method of comparison. Hence the Heavy Flavor Averaging Group (HFAG) has been discouraged from performing these naive averages of all the penguin modes as shown in the yellow band in fig. 7.1.

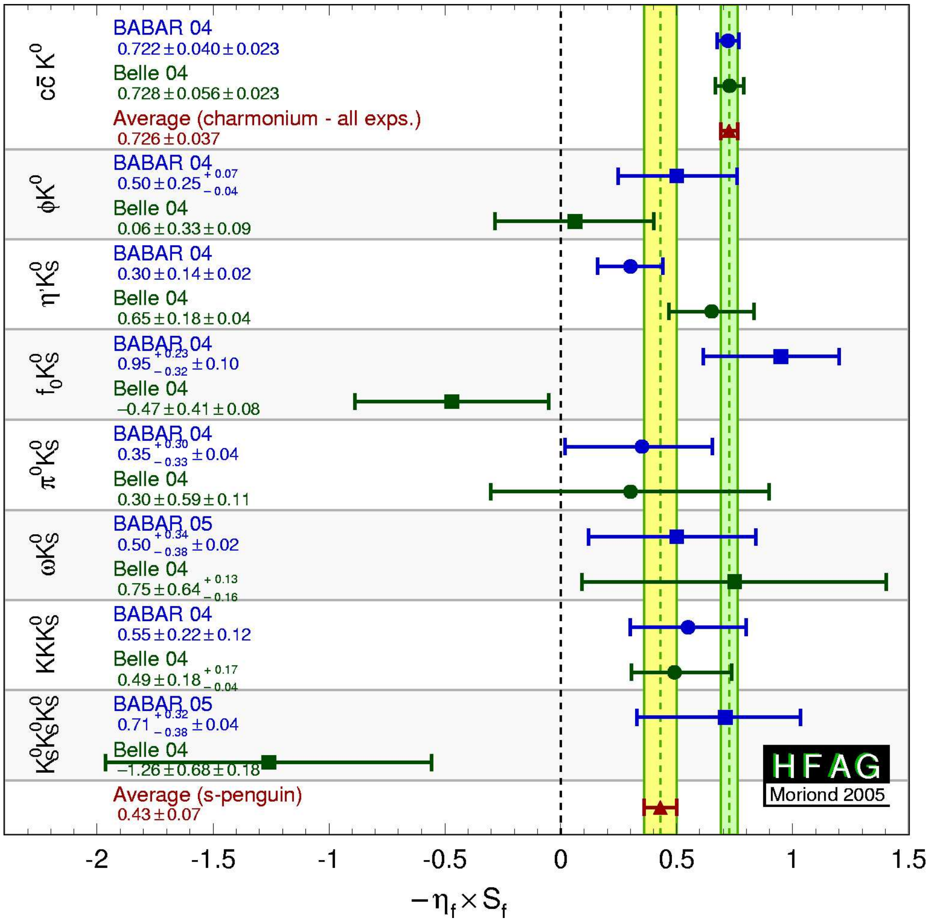

Figure 7.1: Compilation of results of time-dependent CP asymmetries by the Heavy Flavor Averaging Group (HFAG) from $b \rightarrow c\bar{c}s$ and $b \rightarrow s$ penguin decays.

7.3 Future Prospects

BABAR has recently made a preliminary measurement adding decays where one K^0_S is allowed to decay to $K^0_S \rightarrow \pi^0\,\pi^0$. Combining those decays with the ones shown in this dissertation the value of the asymmetries become [39]

$$\begin{aligned} S_{3K^0_S} &= -0.63^{+0.32}_{-0.28} \pm 0.04 \\ C_{3K^0_S} &= -0.10 \pm 0.25 \pm 0.05. \end{aligned}$$

This decay includes an additional $41.0^{+9.2}_{-8.3}$ signal events which improves the statistical uncertainty. The average of the new Belle measurement with this combined measurement gives a central value on S of -0.64 ± 0.23 which is consistent with the SM prediction. By summer of 2006 *BABAR*

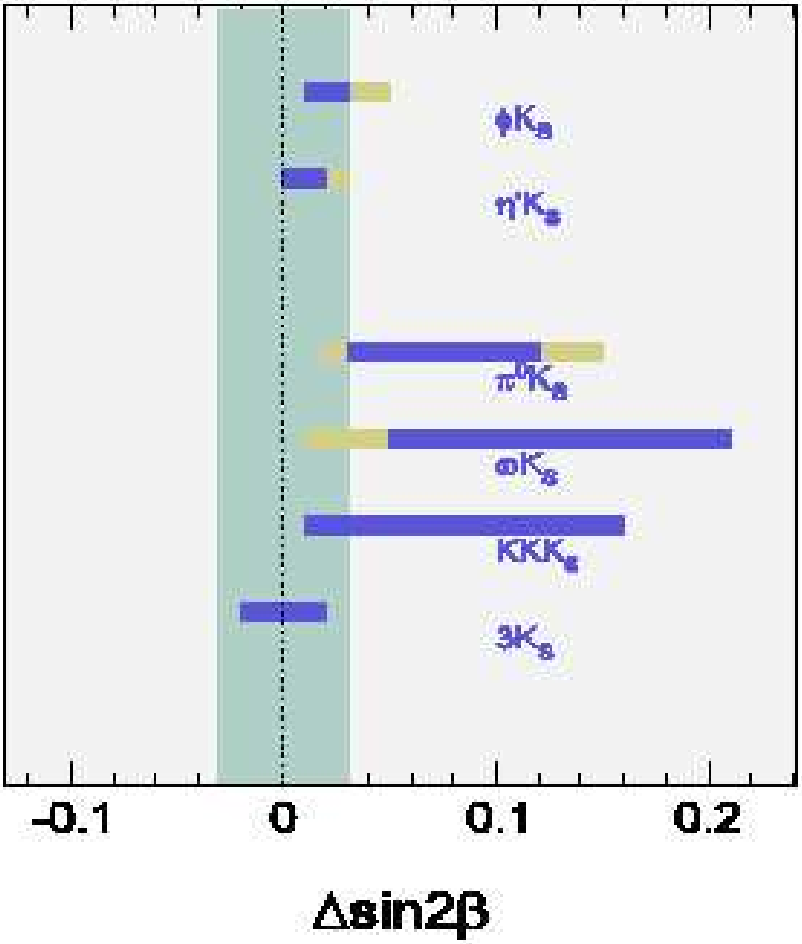

Figure 7.2: QCD factorization predictions for $\Delta \sin 2\beta$ for different penguin modes. The gray bar represents upper bounds determined from the range of values from toy studies and the blue represent upper bounds determined by adding errors in quadrature.

will double their dataset and by summer of 2008 the dataset will be more than five times that presented in this analysis (see fig. 7.4). Doubling the dataset will make the statistical uncertainty of the combined result about 0.21 for S and with five times more data the uncertainty will be reduced to 0.13.

Some updates of results presented this summer at the Lepton-Photon Conference shifted the values of the asymmetries significantly from the winter 2005 results. We saw that the Belle measurement of $B^0 \rightarrow K^0_S\, K^0_S\, K^0_S$ was greatly improved and the central value shifted to a value consistent with our result as well as with the SM. The value of $\sin 2\beta$ from charmonium modes changed from 0.726 ± 0.037 to 0.69 ± 0.03 and many other penguin decay measurements changed to move results closer to $\sin 2\beta_{\mathrm{J}/\psi\, \mathrm{K}^0_\mathrm{S}}$. With *BABAR* taking data at a steady and improving rate the statistical

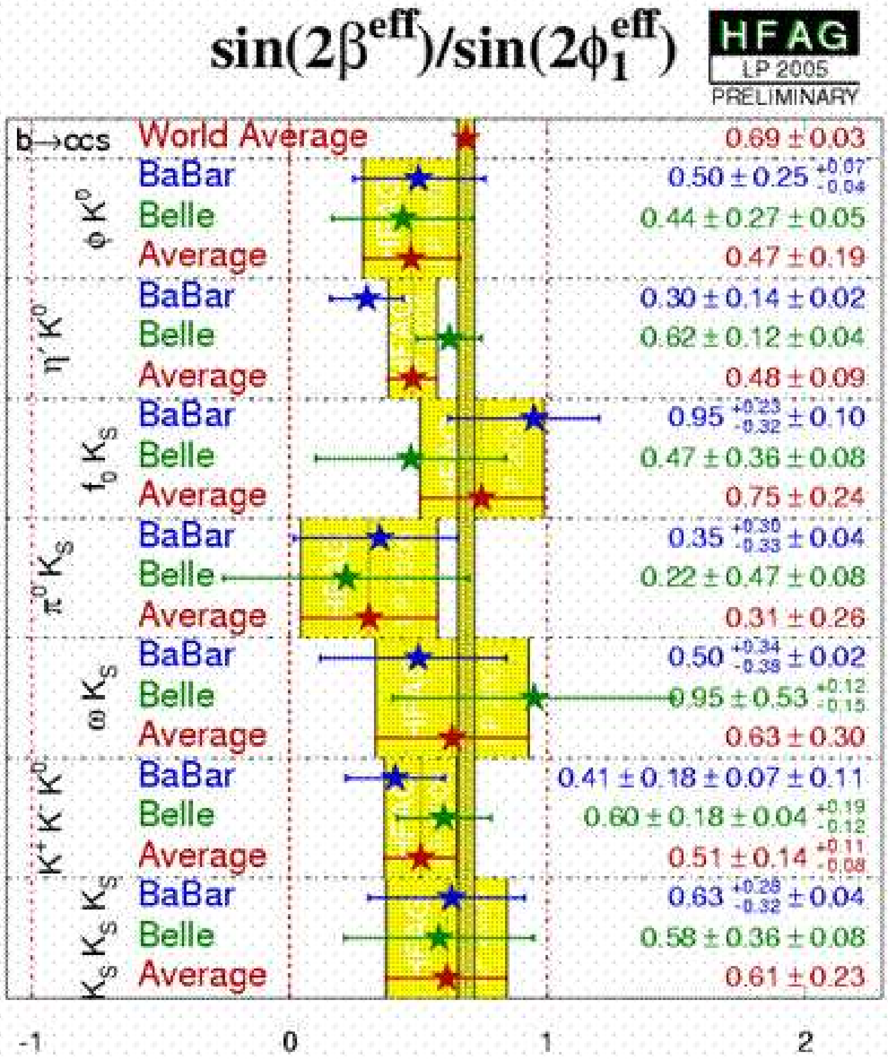

Figure 7.3: Compilation of results of time-dependent CP asymmetries by the Heavy Flavor Averaging Group (HFAG) from $b \to c\bar{c}s$ and $b \to s$ penguin decays.

errors on the measurements can be improved two fold by 2008. Only with more statistics can we tell if $\sin 2\beta$ from the penguin modes deviates from $\sin 2\beta_{\mathrm{J}/\psi\,\mathrm{K_S^0}}$ and therefore have contributions from new physics. As we saw from this summer, fluctuations in the central values can occur and the updates from every season provide interesting results which we look forward to.

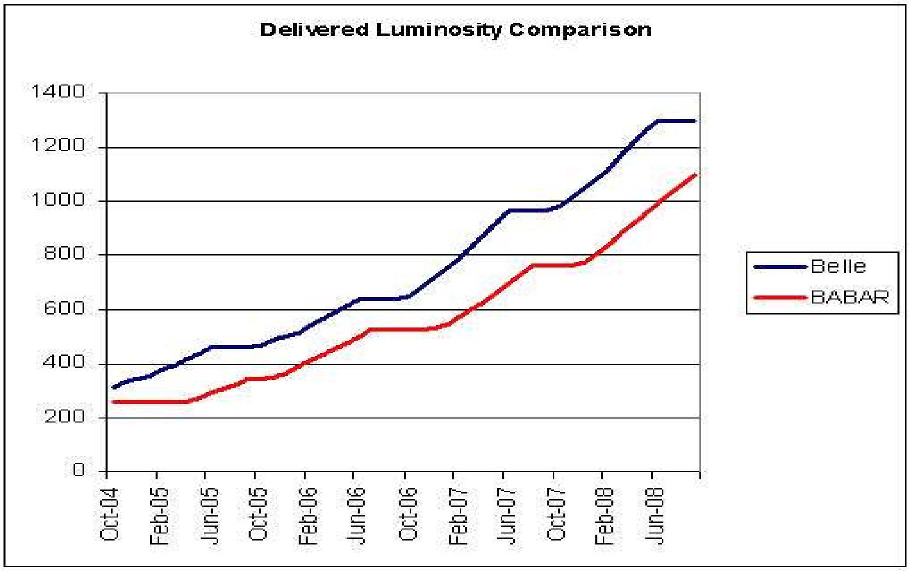

Figure 7.4: Seeman luminosity projection up to Summer of 2008 for both Belle and *BABAR*.

Appendix A

Systematic Uncertainties from PDF Variation

This appendix incluces tables for the PDF systematics in Tables A- A.

Table A.1: Change is S and C as a result of varying m_{ES} PDF parameters by statistical error from fit to signal MC.

Parameter	Values	$\Delta(S)$ +	$\Delta(S)$ -	$\Delta(C)$ +	$\Delta(C)$ -
$N_{m_{ES}}$	0.7459 ± 0.0926	0.0019	-0.0028	0.0008	-0.0007
$\alpha_{m_{ES}}$	2.6896 ± 0.0739	0.0010	-0.0022	0.0001	0.0000
$\mu_{m_{ES}}$	5.2794 ± 0.00003	0.0000	-0.0012	0.0000	-0.0002
$\sigma_{m_{ES}}$	0.0026 ± 0.00002	0.0000	-0.0009	0.0005	-0.0006
Total		0.0021	0.0038	0.0009	0.0010

Table A.2: Change is S and C as a result of varying ΔE PDF parameters by statistical error from fit to signal MC.

Parameter	Values	$\Delta(S)$ +	$\Delta(S)$ -	$\Delta(C)$ +	$\Delta(C)$ -
$\alpha^L_{\Delta E}$	0.1660 ± 0.0050	0.0000	-0.0007	0.0001	-0.0002
$\alpha^R_{\Delta E}$	0.1522 ± 0.0055	0.0004	-0.0014	0.0014	-0.0014
$\mu_{\Delta E}$	0.0075 ± 0.0005	0.0005	-0.0021	0.0000	-0.0003
$\sigma^L_{\Delta E}$	0.0139 ± 0.0004	0.0000	-0.0006	0.0006	-0.0007
$\sigma^R_{\Delta E}$	0.0134 ± 0.0004	0.0005	-0.0019	0.0007	-0.0009
Total		0.0008	0.0034	0.0017	0.0019

Table A.3: Change is S and C as a result of varying $\mathcal{F}$ PDF parameters by statistical error from fit to signal MC.

Parameter	Values	$\Delta(S)$ +	$\Delta(S)$ -	$\Delta(C)$ +	$\Delta(C)$ -
$\mu_{\mathcal{F}}$	-0.0405 ± 0.0166	0.0024	-0.0039	0.0004	-0.0010
$\sigma^L_{\mathcal{F}}$	0.6748 ± 0.0109	0.0000	-0.0012	0.0000	-0.0002
$\sigma^R_{\mathcal{F}}$	0.5533 ± 0.0105	0.0021	-0.0040	0.0017	-0.0022
Total		0.0032	0.0057	0.0017	0.0024

Table A.4: Change is S and C as a result of varying signal tagging asymmetry by statistical error from B_{flav} sample.

Parameter	Values	$\Delta(S)$ +	$\Delta(S)$ -	$\Delta(C)$ +	$\Delta(C)$ -
$\Delta\epsilon_{Cat1}$	0.0034 ± 0.0164	0.0003	-0.0015	0.0043	-0.0044
$\Delta\epsilon_{Cat2}$	-0.0287 ± 0.0156	0.0014	-0.0027	0.0041	-0.0042
$\Delta\epsilon_{Cat3}$	-0.0025 ± 0.0139	0.0014	-0.0042	0.0037	-0.0039
$\Delta\epsilon_{Cat4}$	-0.0089 ± 0.0161	0.0036	-0.0057	0.0044	-0.0047
$\Delta\epsilon_{Cat5}$	-0.0201 ± 0.0160	0.0003	-0.0014	0.0033	-0.0035
$\Delta\epsilon_{Cat6}$	0.0089 ± 0.0191	0.0000	-0.0016	0.0011	-0.0015
Total		0.0042	0.0080	0.0090	0.0095

Table A.5: Change is S and C as a result of varying signal efficiencies by statistical error from B_{flav} sample.

Parameter	Values	$\Delta(S)$ +	$\Delta(S)$ -	$\Delta(C)$ +	$\Delta(C)$ -
ϵ_{Cat1}	0.0875 ± 0.0011	0.0000	-0.0013	0.0000	-0.0003
ϵ_{Cat2}	0.1089 ± 0.0014	0.0000	-0.0011	0.0001	-0.0003
ϵ_{Cat3}	0.1714 ± 0.0017	0.0003	-0.0021	0.0001	-0.0005
ϵ_{Cat4}	0.1358 ± 0.0016	0.0002	-0.0012	0.0000	-0.0003
ϵ_{Cat5}	0.1469 ± 0.0007	0.0000	-0.0013	0.0000	-0.0003
ϵ_{Cat6}	0.0992 ± 0.0012	0.0000	-0.0011	0.0000	-0.0002
Total		0.0003	0.0034	0.0002	0.0008

Table A.6: Change is S and C as a result of varying dilutions and Δ dilutions by statistical error from B_{flav} sample.

Parameter	Values	$\Delta(S)$ +	$\Delta(S)$ -	$\Delta(C)$ +	$\Delta(C)$ -
D_{Cat1}	0.9364 ± 0.0094	0.0000	-0.0023	0.0029	-0.0025
D_{Cat2}	0.9001 ± 0.0101	0.0034	-0.0044	0.0017	-0.0024
D_{Cat3}	0.6916 ± 0.0111	0.0015	-0.0026	0.0007	-0.0012
D_{Cat4}	0.5426 ± 0.0140	0.0063	-0.0077	0.0017	-0.0016
D_{Cat5}	0.3377 ± 0.0146	0.0032	-0.0046	0.0001	-0.0013
D_{Cat6}	0.1821 ± 0.0183	0.0053	-0.0068	0.0027	-0.0035
ΔD_{Cat1}	0.0057 ± 0.0180	0.0000	-0.0028	0.0032	-0.0027
ΔD_{Cat2}	0.0410 ± 0.0190	0.0039	-0.0051	0.0028	-0.0031
ΔD_{Cat3}	0.0285 ± 0.0190	0.0014	-0.0040	0.0036	-0.0031
ΔD_{Cat4}	0.0018 ± 0.0227	0.0012	-0.0036	0.0031	-0.0028
ΔD_{Cat5}	-0.1246 ± 0.0225	0.0000	-0.0017	0.0007	-0.0011
ΔD_{Cat6}	-0.0843 ± 0.0272	0.0000	-0.0016	0.0007	-0.0009
Total		0.0105	0.0150	0.0080	0.0082

Table A.7: Change is S and C as a result of varying signal resolution function parameters by statistical error from B_{flav} sample.

Parameter	Values	$\Delta(S)$ +	$\Delta(S)$ -	$\Delta(C)$ +	$\Delta(C)$ -
b_{core}^{Cat1}	-0.0481 ± 0.0440	0.0036	-0.0046	0.0022	-0.0028
b_{core}^{Cat2}	-0.1030 ± 0.0428	0.0000	-0.0002	0.0025	-0.0026
b_{core}^{Cat3}	-0.1974 ± 0.0336	0.0000	-0.0015	0.0013	-0.0014
b_{core}^{Cat4}	-0.2154 ± 0.0355	0.0014	-0.0032	0.0005	0.0000
b_{core}^{Cat5}	-0.2016 ± 0.0343	0.0000	-0.0007	0.0003	-0.0005
b_{core}^{Cat6}	-0.1514 ± 0.0413	0.0000	-0.0004	0.0001	-0.0002
b_{core}^{NoTag}	-0.2057 ± 0.0269	0.0000	-0.0014	0.0000	-0.0003
s_{core}	1.0569 ± 0.0279	0.0062	-0.0074	0.0008	-0.0003
Δm	0.5020 ± 0.0070	0.0034	-0.0040	0.0038	-0.0035
f_{out}	0.0043 ± 0.0009	0.0000	-0.0018	0.0008	-0.0010
f_{tail}	0.0937 ± 0.0119	0.0050	-0.0063	0.0010	-0.0006
b_{tail}	-1.2420 ± 0.2060	0.0010	-0.0034	0.0026	-0.0021
τ_{B0}	1.5370 ± 0.0150	0.0017	-0.0031	0.0009	-0.0012
Total		0.0097	0.0128	0.0061	0.0060

References

[1] J.H. Christenson et al, Phys. Rev. Lett. **13**, 138 (1964).

[2] A.D. Sakharov, Pisma Zh. Eksp. Theor. Fiz. 5, 32 (1967); JETP Lett. 5, 24 (1956).

[3] I. Bigi and A. Sanda, *CP Violation*, Cambridge University Press (2000).

[4] M. Kobayashi and T. Maskawa, Prog. Th. Phys. **49**, 652 (1973).

[5] *The BABAR Physics Book*,edited by P. F. Harrison and H. R. Quinn,SLAC-R-504 (1998).

[6] Heavy Flavor Averaging Group, *Results on Time-Dependent CP Measurements: Summer 2005 (Lepton-Photon, Uppsala, Sweden and HEP 2005, Lisboa, Portugal)* , http://www.slac.stanford.edu/xorg/hfag/triangle/summer2005/, (2005).

[7] M. Gavela *et al.* Mod. Phys. Lett. **A9**, 895 (1994) and Nucl. Phys. **B340**, 382 (1994); P. Huet and E. Sather. Phys. Rev. D **D51**, 379 (1995).

[8] C.S. Wu, E. Ambler, R.Hayward, D. Hoppes, adn R. Hudson, Phys. Rev.**105**, 1413 (1957).

[9] M. Goldhaber, L. Grodzinns, and A. Sunyar, Phys. Rev.**109**, 1015 (1958).

[10] F. Halzen and A. Martin, *Quarks and Lepton: An Introductory Course in Modern Particle Physics*, (1984).

[11] M.E. Peskin and D.V. Shroeder, *An Introduction to Quantum Field Theory*, (1995).

[12] G. Branco, L. Lavoura, J. Silva, *CP Violation*, Oxford University Press (1999).

[13] Particle Data Group, S. Eidelman *et. al.*, Phys. Lett. B **592**, 1 (2004).

[14] L. Wolfenstein, Phys. Rev. Lett. **51**, 1945 (1983).

[15] Okubo, S. Phys. Lett., 1963, B5, 165. Zweig, G. CERN Report No.8419/TH412 (1964). Iizuka, I. Prog. Theor., Phys. Suppl. 37, 1966, 38, 21.

[16] Y. Grossman and M. P. Worah, Phys. Lett. B **395**, 241 (1997);

[17] M. Ciuchini, E. Franco, G. Martinelli, A. Masiero and L. Silvestrini, Phys. Rev. Lett. **79**, 978 (1997).

[18] T. Gershon and M. Hazumi, Phys. Lett. B **596**, 163 (2004).

[19] H. Cheng, C. Chua, and A. Soni, hep-ph/0506268 (2005).

[20] G. Englehard, Y. Nir, and G. Raz, he-ph/0505194 (2005).

[21] *BABAR* Collaboration, B. Aubert et al, Nucl. Instr. Methods A479, 1 (2002).

[22] *BABAR* Collaboration, B. Aubert et. al., hep-ex/0408065 (2004).

[23] W. Verkerke and D. Kirkby, *The RooFit Toolkit for Data Modelling*, http://roofit.sourceforge.net/ (2005); R. Brun and F. Rademakers, *Root: An Object-Oriented Data Analysis Framework*, http://root.cern.ch/ (2004).

[24] J. Smith, A. Soffer, and R. Waldi, *Recommendation for Exclusive B Reconstruction Analysis Variables*, *BABAR* Note 497 (1999).

[25] J. Ocariz, M. Pivk, L Roos, A. Hoecker, H. Lacker, F.R. Le Diberder, *Background Fighting in Charmless Two-Body Analyses*, *BABAR* Analysis Document 346 (2002).

[26] *BABAR* Collaboration, B. Aubert et al, Phys. Rev. Lett. **93**, 131805 (2004). (2004).

[27] D. Lange, G. Sciolla, M.C. Simani, Y. Zheng, *BtgTest and Tag04: Studies Towards an Improved Tagging Algorithm*, *BABAR* Analysis Document 730

[28] Crystal Ball Collaboration, D. Antreasyan et al, Crystal Ball Note 321 (1983).

[29] ARGUS Collaboration, H. Albrecht et al, Phys. Lett. B **185**, 218 (1987); **241**, 278 (1990).

[30] W. Hulsbergen, H. Jawahery, D. Kovalskyi, and M. Pierini , *Measurement of the branching ratio and the time-dependent CP asymmetries for $B^0 \rightarrow K^0_S\,\pi^0$ decays on run 1-4 data* ,

[31] M. Pivk and F. LeDiberder, physics/0402083 (2004). *BABAR* Analysis Document 904 (2004).

[32] *BABAR* Collaboration, *SVT misalignment files for 14-series data*, http://www.slac.stanford.edu/BFROOT/www/Detector/SVT/LocalAlignment/systematics-14/ (2004).

[33] O. Long, M. Baak, R.N. Cahn, and D. Kirkby, Phys. Rev. D **68**, 034010 (2003).

[34] *BABAR* Collaboration, B. Aubert et al, Phys. Rev. Lett. **95**, 011801 (2005).

[35] Belle Collaboration, K. Sumisawa et al, Phys. Rev. Lett. **95**, 061801 (2005)

[36] Heavy Flavor Averaging Group, *Results on Time-Dependent CP Measurements: Winter (Moriond) 2005.*, http://www.slac.stanford.edu/xorg/hfag/triangle/moriond2005/index.shtml, (2005).

[37] K. Trabelsi, $\sin 2\phi_1$ *Charmless and Radiative Decays*, http://www.lip.pt/events/2005/hep2005/talks/hep2005_talk_KarimTrabelsi.pdf, (2005).

[38] M. Beneke, Phys. Lett. B **620** 143 (2005).

[39] *BABAR* Collaboration, B. Aubert et. al., hep-ex/0507052 (2005).